Nonlinear dynamics of jointed structures: a multiscale approach to predict fretting wear and its effects on the dynamic response

Jason Armand

Department of Mechanical Engineering
Imperial College London

A thesis submitted in fulfilment of the requirements for the degree of
Doctor of Philosophy and the Diploma of Imperial College

December 2017

I dedicate this thesis to my father who passed on his curiosity and passion for science to me.

"*Being a graduate student is like becoming all of the Seven Dwarves. In the beginning you're Dopey and Bashful. In the middle, you're usually sick (Sneezy), tired (Sleepy), and irritable (Grumpy). But at the end, they call you Doc, and then you're Happy*"

Dr. Ronald Azuma

Declaration

I hereby declare that this dissertation is the result of my own work carried out in the Dynamics Group of the Department of Mechanical Engineering at Imperial College London. This work, supervised by Dr. Christoph Schwingshackl and Dr. Loïc Salles, is part of a collaborative R&T project 'SILOET II Project 10' which is co-funded by Innovate UK and Rolls-Royce plc and carried out by Rolls-Royce plc and the Vibration UTC at Imperial College London. No part of the research herein has been previously submitted in whole or in part for consideration for any other degree or qualification in this, or any other university. The work is original, and due attention has been drawn to the work of others. Some of the work described herein has contributed to the following publications:

Armand, J., Salles, L., and Schwingshackl, C. W. (2017). On the effects of roughness on the nonlinear dynamics of a bolted joint: a multiscale analysis. European Journal of Mechanics - A/Solids. (Under review)

Pesaresi, L., Armand, J., Salles, L., Schwingshackl, C. W. and Wong, C. (2017). An advanced underplatform damper modelling approach based on a microslip contact model. ISROMAC 2017 - International Symposium on Transport Phenomena and Dynamics of Rotating Machinery. (Accepted for publication)

Armand, J., Pesaresi, L., Salles, L., and Schwingshackl, C. W. (2016). A Multiscale Approach for Nonlinear Dynamic Response Predictions With Fretting Wear. Journal of Engineering for Gas Turbines and Power, 139(2), 022505. doi:10.1115/1.4034344.

Armand, J., Salles, L., and Schwingshackl, C. W. (2015). Numerical Simulation of Partial Slip Contact Using a Semi-Analytical Method. ASME. International Design Engineering Technical Conferences and Computers and Information in Engineering Conference, Volume 8: 27th Conference on Mechanical Vibration and Noise. doi:10.1115/DETC2015-46464.

Jason Armand
December 2017

Acknowledgements

First of all, I would like to thank Dr. Christoph Schwingshackl for giving me the opportunity to carry out this PhD research, and for his constant enthusiasm and useful guidance throughout these years.

I wish to express my gratitude to Dr. Loïc Salles for sharing his broad expertise with me and his essential assistance with the code FORSE and many other technical aspects of my work. Without his precious help, these years would have surely been even more challenging.

I am also thankful to Prof. Daniele Dini for the very interesting and useful discussions we had about contact modelling and my implementation of 'SAM'.

Thanks to Innovate UK and Rolls-Royce plc. for funding this research and to Dr. Chian Wong for his interest in my project, his useful comments and his industrial perspective on my research.

I am grateful to Dr.-Ing. Lars Panning-von Scheidt and Prof. Michael Lowe who kindly accepted to review this thesis and to be my examiners in my viva. Thanks to them for their thoughtful comments on my work and the stimulating discussions we had during my viva.

I thank my past and present fellow labmates for the heated debates and the good 'craic' we had in the office and during our 'brazilian breaks'. Special thanks go to Dr. Luca Pesaresi for our very fruitful collaboration and the now famous 'TurboExpo paper' written together. I also wish him the best of luck to take over my research and the future developments of 'SAM'.

I would like to express my special appreciation to Peter Higgs who took great care of all my logistical and administrative needs and who kindly accepted to proofread this thesis.

Last but not least, I would like to thank my family for always believing in me and for their support during these challenging years.

Abstract

Accurate prediction of the vibration response of friction joints is of great importance when estimating both the performance and the life of built-up structures. The relative motion at the frictional interfaces can lead to a highly nonlinear dynamic response and cause fretting wear at the contact. The latter, by changing the contact surface geometry, affects the contact conditions of the interface and consequently impacts the nonlinear dynamic response of the entire assembly, which today is ignored in the analysis.

To address the above issue, a novel multiscale approach that incorporates wear into the nonlinear dynamic analysis is presented. A contact solver, based on boundary integral equations, is implemented to compute local contact stresses and stiffness which, in combination with an energy wear approach, allow to compute fretting wear at the contact interface. The nonlinear dynamic response of the whole system is computed using a multi-harmonic balance approach and a continued iteration between the contact and nonlinear dynamic solvers allows the prediction of the nonlinear dynamic response over time.

After describing its implementation in detail, the contact solver results are fully verified against a range of test cases for which an analytical solution is available. A comparison against finite element simulations demonstrates the accuracy and computational benefits of the implemented solver. The limitations of the solver due to its underlying half-space assumption are also discussed.

The proposed multiscale approach is applied to an underplatform damper-blade system. A significant impact of fretting wear on the nonlinear dynamic behaviour of the blade-damper system is observed, highlighting the sensitivity of the nonlinear dynamic response to changes at the contact interface due to wear. A strong effect of rough interfaces on the wear rate and the resulting interface parameters was also discovered, making them a crucial component for nonlinear dynamic response predictions over time.

Table of contents

List of figures

List of tables

Chapter 1

Introduction

1.1 Context and motivations

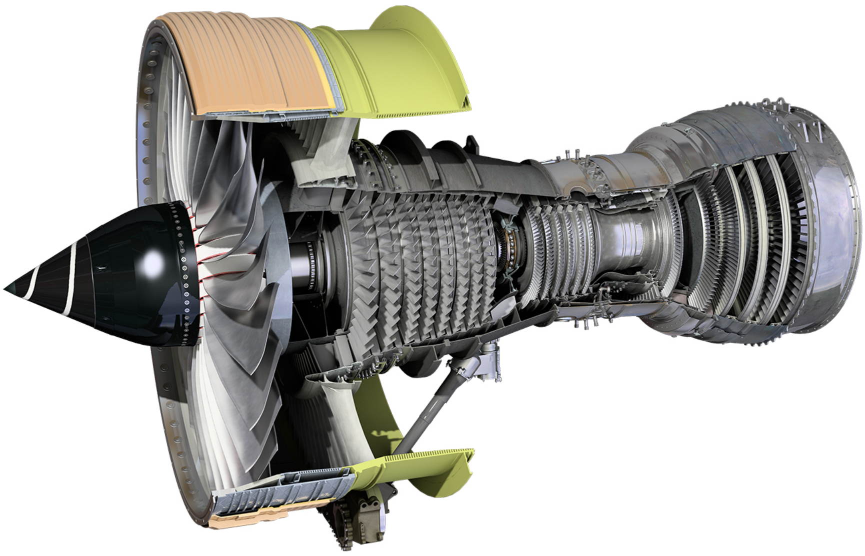

Fig. 1.1 Rolls-Royce Trent 700 engine [Source: Rolls-Royce plc.]

Aero-engines, such as the Rolls-Royce Trent 700 depicted in Fig. 1.1, are among the most critical components of an aircraft. Their design results from trade-offs between performance, safety, environmental footprint, cost of implementation and operating costs. In order to improve performance and efficiency, key components of the engines, such as the bladed-discs, are subjected to increasing mechanical and thermal loads. During the design process, the engine manufacturers need to predict the behaviour of the engine and its components accurately in order to ensure performance and operational safety. One particular issue thereby is the vibration response of the structure, since high amplitude vibration can lead to performance reduction, wear at interfaces, and most importantly can significantly impact the remaining life of a component.

Among other components, bladed-discs and their friction interfaces are critical from a safety perspective. Wear occurring at the contact interfaces can cause cracks that may lead to the early failure of a blade or the disc, which may eventually cause a catastrophic failure of the engine. Apart from bladed-discs, a large number of friction joints can be found in an aero-engine: there are bolted joints between the casings, spline couplings which ensure power transmission between different shafts, rotor flanges or underplatform dampers. When the engine is running, all these joints are sources of friction and energy dissipation. For some of these joints, the friction forces can be detrimental for the engine behaviour. For instance, the resulting rotating damping in rotor flanges can lead to instability of the rotor and dangerously high vibratory stresses. Conversely, for some joints, the friction forces are beneficial for the engine since they reduce the vibration amplitudes. This is the case for underplatform dampers that are specifically designed and introduced to mitigate turbine blades vibrations. Whether their behaviour is beneficial or detrimental, understanding the complex phenomena taking place in the friction joints of the engine is essential for accurate predictions of its behaviour.

Vibrations in aircraft engines

There exist many sources of vibrations in an aircraft engine which can be of structural or aeroelastic nature [47]. Structural sources include the vibrations due to torsional and lateral dynamics of the rotor shafts, rubbing phenomena in rotor to stator contact and extreme events such as blade releases due to ingestion of foreign objects such as birds or ice. The two main aeroelastic sources are forced synchronous responses and flutter instabilities. In the case of forced response, the vibrations are caused by a non-uniform pressure acting on the blades. From the perspective of the rotating bladed-disc, this pressure field takes the form of a wave traveling with rotor speed which results in dynamic loading with frequencies being integer-multiples of the rotational frequency, hence the terms 'synchronous excitation' and 'engine order excitation'. When an excitation frequency coincides with a natural frequency of the structure, the amplitude of the forced response can reach particularly high levels. A Campbell diagram, such as the one shown in Fig. 1.2, is typically used to identify these resonance coincidences, also called 'critical speeds'.

In contrast, flutter is a self-excited and self-sustained aeroelastic instability which is caused by the fluid-structure interaction between a blade vibration and the resulting unsteady pressure distribution on the blade and its neighbours. Depending on the phase angle of the unsteady aerodynamic pressure distribution, it can either reduce

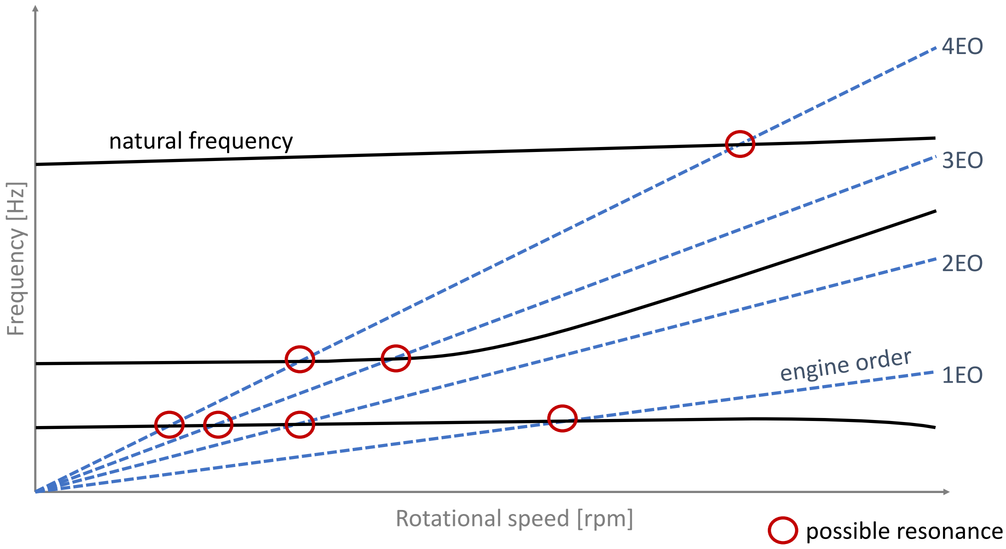

Fig. 1.2 Schematic Campbell diagram

or increase the amplitude of the vibration. In the latter case, self-excited vibrations (natural oscillations) appear and the blade becomes aerodynamically unstable. In contrast to forced response, the natural oscillation frequency is generally not an integer-multiple of the rotational speed.

Underplatform damper-blade friction interface

Considering a high-pressure turbine underplatform damper-blade system, which will be studied in the fourth chapter of this thesis, the friction joint basically consists of two contact interfaces between the damper and two adjacent blades. Due to the rotational speed of the turbine, the blades and the damper experience centrifugal forces CF which generate high-intensity and low-frequency loadings at the friction contact interfaces. These loadings are relative micro-displacements δ, normal (N) and tangential (T) forces as depicted in Fig. 1.3. These low-cycle excitations are often simplified to a unique loading during take-off and a unique unloading during landing. As a result, one flight represents one low-frequency cycle. The blade-damper system is also subjected to low-amplitude and high-frequency excitations which are due to the aerodynamic loads and structural vibrations introduced in the previous section.

Fretting wear, fretting fatigue and fretting corrosion

These cyclic loadings of the contact interfaces induce damage which is called fretting. More precisely, fretting activates two damage mechanisms: fretting fatigue of materials and fretting wear of the contacting surfaces. Fretting fatigue leads to crack nucleation and propagation which is a typical cause of failure of blades. Fretting wear corresponds

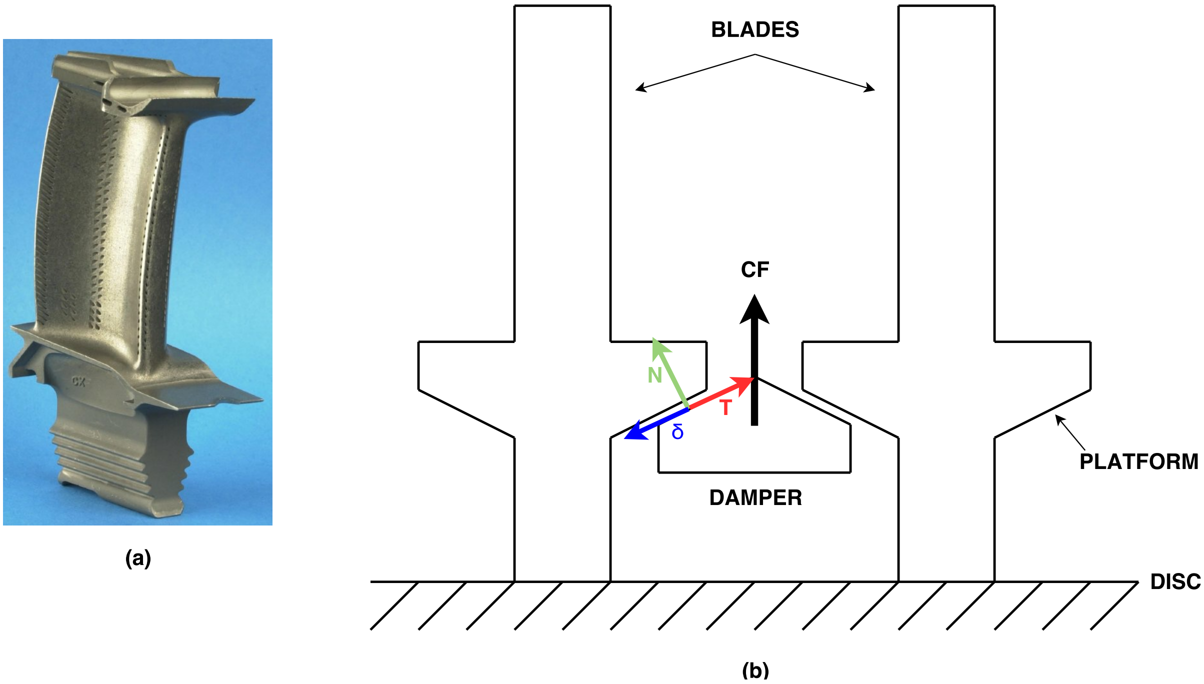

Fig. 1.3 (a) Rolls-Royce HPT blade and (b) scheme of the blade-damper contact loadings

to the material removal from the surface of the bodies in contact. Due to the presence of oxygen in the contact area, the material removal results in the production of oxide debris, hence the term fretting corrosion. These debris may be trapped and stay in the contact area and form an interfacial layer called third body. This third body affects the mechanical and chemical properties of the contact interface. Fretting wear is a complex process involving several sub-wear participants, including adhesive wear, surface fatigue wear, delamination wear, corrosive wear and abrasive wear, as described in [7-10], and is not as well understood as fretting fatigue.

Fretting wear and fretting fatigue are both extensively studied in order to constantly improve flight safety. These studies have led to different solutions that are used today by the engine manufacturers to improve resistance to fretting. The material commonly used for blades and discs is the titanium alloy Ti-6Al-4V which is light, strong and corrosion resistant. Blades and discs are forged and machined, and their contact interfaces are reinforced using a shot peening process. By adding compressive residual stresses on the surface, this process reduces crack nucleation and propagation. Solid coatings are also applied to contact surfaces [36]. Over time, part of the coating is removed due to wear, and new layers of coating have to be applied during shop visits.

Regardless of these solutions, fretting fatigue and fretting wear continue to be challenging issues for the engine manufacturers. A better understanding of fretting phenomena and improved modelling capabilities in terms of fretting could potentially lead to more efficient and sustainable solutions.

Fretting wear and nonlinear dynamics

By changing the contact geometry and the composition of the mating surfaces, fretting wear is having an impact on the stiffness of the friction joint and the energy dissipation mechanisms taking place at its contact interfaces. These two parameters drive the dynamic behaviour of the joint and therefore influence that of the assembled structure. As a result, fretting wear will inevitably have an impact on the nonlinear dynamic response over time of the assembled structure, which makes its prediction of great importance to the engine manufacturers. Due to its complex nature, only very few attempts [157, 158] have been made to start addressing this problem.

1.2 Research objectives

The main goal of this PhD project is to evaluate and understand the effects of a change of the contact geometry due to fretting wear on the nonlinear dynamic response of a jointed structure with dry friction interfaces. To achieve this goal, several objectives have been identified that will be addressed in this work:

1. Develop a flexible and computationally efficient numerical tool to solve contact interface problems and extract local contact conditions which are key to evaluate fretting wear.

2. Combine the contact solver with a reliable wear prediction approach to compute time dependent input parameters for the nonlinear dynamic analysis.

3. Couple the wear prediction approach to the existing nonlinear dynamic solver FORSE.

4. Obtain an in-depth understanding of the effects of wear on the dynamic response of the system with a particular focus on frequency variations and energy dissipation over time.

Due to the challenges to meet these objectives, a purely numerical approach will be taken.

1.3 Thesis overview

This thesis is divided into seven chapters, the first one being the present introduction.

In Chapter 2 an overview is given of the existing work that is most relevant to the present research. First of all, the most popular wear modelling techniques will be presented and discussed. After that, the few works considering the coupling between nonlinear dynamics and wear will be introduced. Finally, the state-of-the-art methods to predict the nonlinear dynamics of jointed structures will be described.

Chapter 3 presents the development of a contact solver based on boundary integral equations. The first part of the chapter is dedicated to the theoretical aspects of the elastic contact. In the second part, the numerical solutions of the contact problems and their implementation are described in detail. The verifications of the code against analytical solutions are the subject of the third part of this chapter. Finally, the effects of the underlying half-space assumption on the solver results are discussed.

In Chapter 4, a novel multiscale approach, combining the developed contact solver, an energy wear approach and an existing nonlinear dynamic solver, is proposed in order to model and account for fretting wear in a nonlinear dynamic analysis. A detailed description of the approach is provided before demonstrating its potential on an underplatform damper system test case. The results and their implications from a turbomachinery design perspective will also be discussed.

The multiscale approach is extended in Chapter 5 to the analysis of rough contact to allow the study of its impact on the nonlinear dynamic response. After introducing a few key roughness concepts and showing how to numerically generate rough surfaces, an upgrade of the previously presented multiscale approach is introduced. The effects of surface roughness on contact conditions and on the nonlinear dynamic response will be illustrated on a single bolted joint system.

In chapter 6, the finalised multiscale approach is applied to that single bolted joint system to highlight the effects of surface roughness on fretting wear and in turn on the nonlinear dynamics of the system, thereby providing an understanding of the physical processes that impact the dynamic response over time.

Finally, the conclusions of this work will be presented in Chapter 7 along with some perspectives and recommendations for future work.

Chapter 2

Literature survey

2.1 Introduction

In this chapter an overview is given of the existing works that are most relevant to the present research. First of all, the most popular wear modelling techniques will be presented and discussed. After that, the few works considering the coupling between nonlinear dynamics and wear will be introduced. Finally, the state-of-the-art methods to predict the nonlinear dynamics of jointed structures such as bladed discs will be described.

2.2 Wear models

In order to predict the influence of fretting wear on the dynamic response of a structure, wear must first be evaluated. A large number of wear models has been developed in the past, as indicated by Meng and Ludema [109] who reported the existence of over 180 wear models but only a brief overview of the most commonly used models will be provided here. These models allow the direct computation of the wear volume, i.e. the volume of material removal due to the fretting wear process, which can then be used to update the contact conditions and in turn the nonlinear dynamic analysis, as will be described later in this chapter.

2.2.1 Archard's law

The law proposed by Archard for adhesive wear in 1953 [6] constitutes a recognised and well-accepted reference in terms of wear modelling. Despite its apparent simplicity, it has been validated against a wide variety of materials undergoing sliding wear by Archard and Hirst [7] and by Rabinowicz [151] who extended the law to abrasive wear. These models assume that wear is the result of adhesion between asperities followed by fracture. The volume of wear particles V is given by:

$$\frac{V}{s} = k\frac{N_0}{H} \tag{2.1}$$

where s is the sliding distance, N_0 the applied normal load, H the hardness of the material and k is the dimensionless wear coefficient which represents the probability that an asperity interaction results in the formation of a wear particle. The wear coefficient must be determined experimentally and can vary from 10^{-7} to 10^{-2} depending on the operating conditions and material properties. The following local form of Archard's law is often used in fretting wear analysis:

$$dh(x,t) = k' p(x,t) ds(x,t) \tag{2.2}$$

where dh is the local wear depth, p is the contact pressure and ds is the slip increment. $k' = \frac{k}{H}$.

2.2.2 Wear energy approach

In the last decade, some researchers such as Fouvry et al. [46] have investigated the link between the wear response and the energy dissipation of a tribo-system. A linear relationship between the wear volume and the frictional dissipated energy in a tribo-system based on experiments could be established. This approach takes into account the variations of the friction coefficient and can be easily calculated from a measured hysteresis loop, such as the one depicted in Fig. 2.1 in which the white area enclosed by the curve corresponds to the frictional dissipated energy per cycle Ed_i. The total wear volume obtained after N cycles is computed using the accumulated

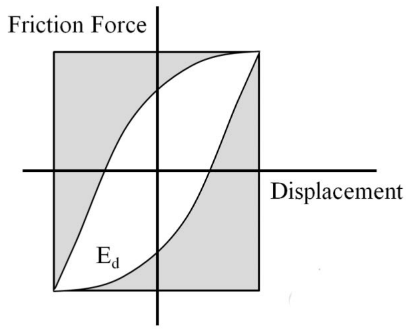

Fig. 2.1 Friction hysteresis loop

dissipated energy:

$$V = \alpha \sum_{i=1}^{N} Ed_i \tag{2.3}$$

where α is the wear coefficient determined experimentally. For adhesive wear tribocouples, a significant part of the energy dissipation is due to the debris ejection process. An increase of the applied sliding amplitude will promote an increase of the debris ejection rate and consequently of the energy wear rate. To capture this effect, a modified sliding reduced energy wear formulation has been proposed by Fouvry et al. [44, 122]:

$$V = \alpha \sum_{i=1}^{N} \frac{\delta g_i}{\delta g_{\mathrm{ref}}} Ed_i \tag{2.4}$$

where δg_i is the applied sliding amplitude and δg_{ref} is a reference sliding value, associated, for instance, to a key point loading condition.

2.2.3 Thermodynamics approach

Friction and wear are irreversible processes which disorder a system and generate irreversible entropy to agree with the second law of thermodynamics. Therefore, entropy appears like a natural candidate to describe and predict these two processes.
Klamecki [86] studied wear as a non-negative entropy production process and showed that friction is a dissipative process. He presented a thermodynamic model of wear for a system idealised as a single body to which heat and work are applied and from which mass transfer can occur.
Zmitrowicz [198, 199] built a thermodynamic model of contacting solids. This model includes the interfacial layer of wear products (third-body). A set of governing equations and a set of dependent variables describing the material properties of the bodies, the layer and the contact are derived from this model.
Doelling et al. [37] and Ling et al. [94] investigated the relation between the normalised entropy flow and normalised wear and reported a linear relationship between the two.
Bryant et al. [18] worked on a thermodynamic characterisation of degradation dynamics which employs entropy as the fundamental measure of degradation. They showed that components of material degradation can be related to the production of corresponding thermodynamic entropy by the irreversible dissipative processes that characterise the degradation.
Dragon-Louiset and Stolz [39] proposed a thermodynamical model for wear analysis of two contacting bodies with an interfacial fluid. Their model comprises the two bodies in contact and an interface made of the damaged part of both materials, the fluid and the wear debris. Based on the energy release rates, a wear criterion is formulated for each solid. Energy release rates are commonly used in fracture mechanics to describe crack propagation but in this model, they characterise the production of wear

debris by damage of solid and particle detachment. The interface is characterised by an internal variable φ which is the volume fraction of the particles and its thickness e. The conservation of mass for the three components of the interface, i.e. the debris of solid 1 and 2 and the fluid, link φ and e to the wear velocity and the relative velocity between the two solids.
The theoretical framework of the thermodynamics approach given in the above key papers is quite complicated and a large number of parameters and variables is required for the calculations. As for experimental studies, the major challenge is the measurement of entropy itself. Using simplifying assumptions, it seems to be predictable based on temperature measurements [3] but one can question the accuracy, robustness and range of application of this method.

2.3 Quasi-static wear analysis

Once a wear model has been selected, computational techniques are required to solve the contact problem and predict the amount of wear. Different techniques that can be used for this purpose will be presented in the following.

2.3.1 Finite Element and Boundary Element Methods

The Finite Element Method (FEM) is widely used in mechanical engineering since it provides good accuracy and robustness. Many commercial FEM tools are available and specific features can be easily added through subroutines into most of them, which is why the FEM is the most commonly used numerical tool to deal with wear.
In 1994, Johansson [76] presented a finite element solution that incorporates a local implementation of Archard's equation to evaluate changes of contact geometry. Following his work, other researchers [84, 108, 113, 123, 142, 200] successively developed improved finite element modelling for sliding and fretting wear. Based on Archard's law, the general idea is to update the worn surface profile during an iterative FEM process:

1. Initially, the contact problem is solved without any wear consideration. The resulting pressures, shears and slips are then extracted at each node and will be used as inputs for wear computation.

2. A local wear law, such as the local form of Archard's law in Eq. 2.2, is used to compute the local wear depth at each node.

3. Once the local wear volume is known, the mesh of the contacting surfaces is updated by adjusting the position of the nodes by the local wear depth.

4. The problem is solved with the updated mesh. This iterative process will be executed until either a maximum number of iterations or a maximum cumulated wear depth has been reached.

The Boundary Element Method (BEM) is an alternative to the FEM where the variables are only calculated at the boundaries instead of the whole domain. This method avoids discretising the entire volume into discrete finite elements and is therefore computationally less expensive. Nevertheless, it is based on the resolution of partial differential equations which must be formulated as integral equations [5], which is not always possible.

The BEM has been applied to sliding wear problems [173, 174] and more recently to fretting wear [85, 155]. The use of this method, together with Archard's law, is similar to the one used within the FEM framework. Its results have been compared to both FEM and experimental results and a good agreement was obtained.

2.3.2 Finite Discrete Element Method (FDEM)

The FDEM is a multiscale method coupling the Finite Element Method (FEM) with the Discrete Element Method (DEM) [103]. The DEM makes it possible to model discontinuous media such as the third body in a worn contact. It is commonly used for geological applications [32] but it has also been successfully applied to third body modelling [91, 192] and fretting wear [90, 92].

Within the FDEM, each particle of the third body is considered as a solid body and solid dynamics equations are applied to each particle. Then the macroscopic properties can be determined by integration or averaging: integration of elementary loads between a particle and its neighbours gives normal and tangential forces, and averaging of particle velocities at one section gives the velocity distribution. As for the first contacting bodies, they are modelled using finite elements.

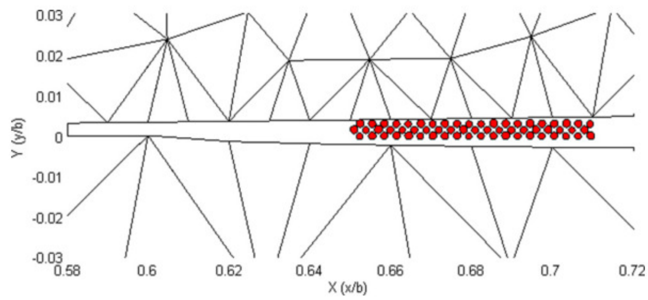

Fig. 2.2 Wear particles introduced in the slip zones of the contact [91]

In Leonard's approach [90–92], the third body particles are modelled by spherical rigid elements, depicted in Fig. 2.2, whose material properties are implemented

through a contact stiffness. The interactions between each contact pair are solved using the penalty method [92]. The Coulomb law is used for the frictional behaviour. The wear volume, which is linked to the number of third body particles to introduce in the contact area, has been computed using both Archard's law and the wear energy approach, and the two methods showed a very good agreement.
The iterative process used to solve the problem is very similar to the one described for the FEM: (a) calculation of one fretting cycle, (b) extraction of the pressure, shear and slip distributions, (c) calculation of the wear loss and the new surface profile using Archard's law (or the energy wear approach) and (d) update of the nodal coordinates and introduction of wear particles whose volume equals the current wear loss into slip zones of the contact.

2.3.3 Semi-Analytical Methods

An alternative to the use of the finite element method is what is called the semi-analytical method (SAM), derived from the boundary element method, which consists of a numerical summation of elementary solutions in a contact solver scheme [15, 99]. One of the main advantages of this technique is that only a small region of the boundary of the contacting bodies, the one enclosing the contact area, is to be meshed, leading to a dramatic decrease in computational cost compared to the finite element method, in which the entire bulk of the contacting bodies has to be meshed. Kalker [80] gave a mathematical formulation of this method and proposed an algorithm for its resolution. The key idea is to express the contact problem between two elastic bodies as a convex quadratic programming problem with non-negative constraints which can be solved using well-known optimisation algorithms for linear programming, such as the simplex algorithm or the conjugate gradient method. Another key feature of the method is that acceleration techniques, such as the Multigrid method [17, 101] and the fast Fourier transforms method [78, 97, 120, 144], can be used to further reduce its computational cost. Using such acceleration techniques, computations are now fast enough to perform numerical analysis of elastic rough contact. Recent developments in the literature include the introduction of a thermo-elastic behaviour [95], the effect of coatings [96, 124], elastic-plastic behaviour and thermo-elastic-plastic behaviour [14, 73, 107, 117–119, 191]. An interesting improvement and analysis of SAM can be found in the works of Gallego et al. [51] who proposed a computational method based on a three scale analysis to solve a fretting wear problem. It consists in coupling a semi-analytical (SA) contact solver, used to solve the local contact problem and compute wear, with the finite element method used to determine the structural behaviour of the macro-scale system. This method allows a fine discretisation of the contact zone while keeping the contact computations very fast. More recently, Vollebregt [188] showed that the number of conjugate gradient iterations could be significantly reduced by using a FFT-based preconditioner. Bemporad and Paggi [9] presented a comprehensive comparison of the available optimisation algorithms for the solution of the frictionless normal contact between rough surfaces and showed that the Non-Negative Least Squares (NNLS) algorithm was one order of magnitude faster that a constrained CG algorithm, which makes it the fastest algorithm available to date.

2.3.4 Molecular dynamics

Considering the micro-scale of wear mechanisms, the Molecular dynamics (MD) approach can be seen as an appropriate tool for wear analysis. This method has been used for cutting tool wear modelling [27, 57], as illustrated in Fig. 2.3, and more recently Aghababaei et al. [2] demonstrated its ability to reproduce the complex adhesive wear mechanisms observed in atomic force microscopy (AFM) experiments [12, 61, 72, 111, 163, 184]. Within this approach, the modelling goes down to the

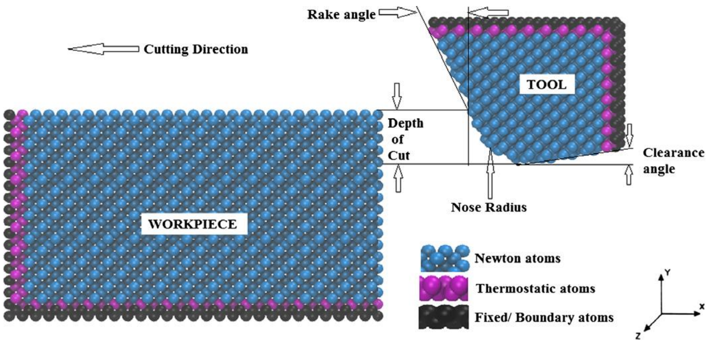

Fig. 2.3 Schematic of the MD simulation model [57]

atomistic level. The bulk materials are simulated by their constitutive atoms. The interactions between the atoms are determined with force fields: either intra-molecular forces (chemical bonds, bond angle, dihedral angles) or inter-molecular forces (Van der Waals or electrostatic). The key parameter is the distance between the atoms. Using an energy potential such as the Morse potential [20, 105] or the Tersoff potential [58, 182], the forces acting on the atoms can be calculated. After summing up all the forces acting on an atom, the Newton's equations of motion are used to calculate the acceleration of each atom. This value is then integrated to give the velocity and the position of the atom over time. Therefore, the volume of the wear particles and the composition of the contacting surfaces and of the third body can be obtained at any given time.

2.3.5 Movable Cellular Automata

The Movable Cellular Automata (MCA) presents the advantages of both classical cellular automaton and discrete element method. Within the MCA framework, the system consists of a set of interacting elements, the cellular automata. The dynamics of this set is defined by the mutual forces acting on the cellular automata and the rules for their relationships, coupled with the use of Newton's equations of motion, just as for the Molecular Dynamics method. The MCA has been applied to model friction and wear process in brake systems [115, 190]. Popov et al. [145] have worked on the theoretical framework of the MCA applied to tribology. They also applied it to real case studies of wear in combustion engines [146] and wheel/rail contacts [19].

2.3.6 eXtended Finite Element Method

The eXtended Finite Element Method (X-FEM) [1] is a method that has been developed to deal with discontinuities such as cracks, voids, inclusions and material interfaces. This is a mesh-less method based on the enrichment of the classical finite element nodal approximation. For the instance of a crack, two enrichment functions are used : the Heaviside enrichment that takes into account the jump displacement through the body of the crack and the crack tip enrichment which represents the singular stress and displacement fields at the crack tip. This enrichment is realised through the Partition of Unity concept which ensures the conservation of the sparsity of the matrix. The level-set method is used to track the crack path at all time and to determine the nodes that need to be enriched. This method looks very convenient to avoid the remeshing required by wear modelling. Instead of remeshing the part by moving the node by the local wear depth, it could be done by updating the level-set functions. This method has already been used for modelling of frictional contact problems [82] but, to the best knowledge of the author, the X-FEM method has yet to be used to perform a wear analysis.

2.3.7 Smoothed Particle Hydrodynamics (SPH)

The smooth particle hydrodynamics (SPH) is another mesh-less method. Originally developed by Lucy [102] and Gingold and Monaghan [56] to solve astrophysical problems in open space, it has since been used in solid and fluid dynamics problems. Recent applications include wear study of a machining tool [21, 179]. Within this approach, the problem domain is divided into a set of discrete elements, referred to as particles. Each particle carries all the properties of the assigned segment of the considered simulation domain such as its mass, position and velocity. In order to interpolate field variables, instead of using a grid and shape functions as done within the FEM method, a kernel interpolation (also called smoothing or weighting function) is used. The SPH particles have a spatial distance, called smoothing length parameter, over which their properties are "smoothed" by the kernel function, as illustrated in Fig. 2.4. The physical quantity of any particle can be obtained by summing the relevant properties of all the particles which lie within the range of the kernel. The most commonly used kernels are the Gaussian function and the cubic B-spline. Stresses and strains are derived from constitutive relations.

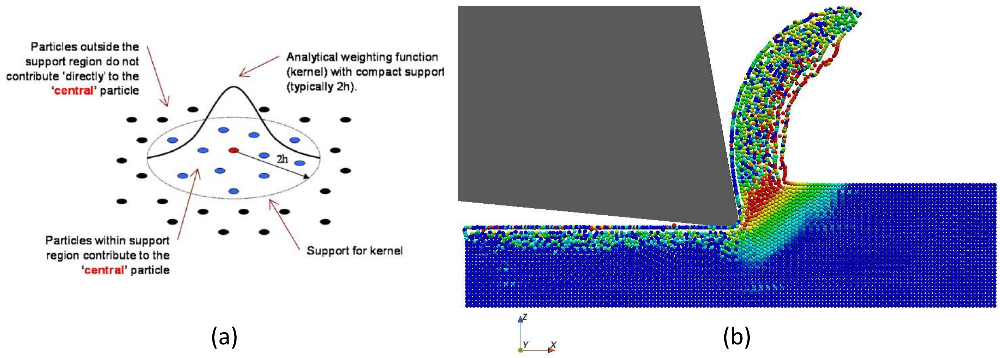

Fig. 2.4 (a) Representation of the kernel function [81] and (b) application to metal cutting [178]

2.4 Nonlinear dynamics predictions of jointed structures

2.4.1 Contact modelling

The past few decades have seen the development of a number of modelling approaches for jointed structures. Some examples include detailed finite element models of joint components [62, 83, 153], continuum element approaches using zero-thickness elements [59, 79] and thin-layer elements [35, 106, 175], lumped models [53, 63, 162], whole-joint modelling using hysteresis elements [70, 71, 169], and node-to-node coupling with friction contact elements [137, 165]. That last method is the one implemented in FORSE, the VUTC in-house multi-harmonic balance solver. This method has been used in the present research which is why it will be presented in more details hereafter. A more extensive survey of the very rich literature can be found in the review papers of Krack et al. [87], Rizvi et al. [154] and the book of Brake [16].

Node-to-node coupling with friction elements

A number of friction elements, describing a point-to-point contact, and based on the Coulomb friction law have been developed in the past. These friction elements can be one-dimensional [29], planar [161, 172], or three-dimensional [26, 148], where the relative motion is considered one-, two- or three-dimensional, respectively. Using this contact modelling, several methods were developed to analyse systems with friction interfaces such as bladed disc assemblies by Petrov [129], Charleux et al. [25], Cigeroglu et al. [28], Firrone and Zucca [43], Csaba [31]; tip shrouds by Yang and Menq [197], Petrov and Ewins [134], Menq et al. [110], Wagner and Griffin [189]; bladed disc with wedge dampers by Sanliturk and Ewins [161], Petrov [130], Petrov and Ewins [139], Panning et al. [121], Hohl et al. [68]; mechanical joints by Petrov and Ewins [139], Ferri [42], Wentzel [195], Putignano et al. [150].

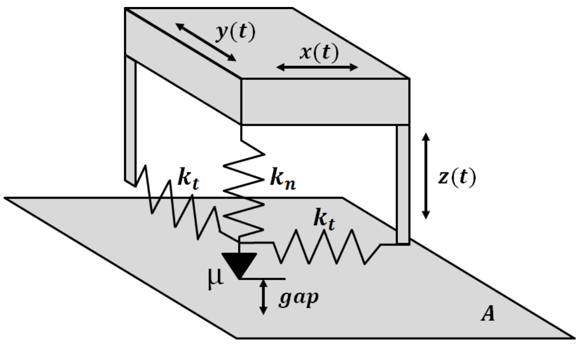

Fig. 2.5 3D friction element

The three-dimensional friction element implemented by Petrov into FORSE [134], depicted in Fig. 2.5, has been used in the present research. This friction element comprises two coupled Jenkins elements [11] allowing for 2D in-plane motion, and a third spring element allowing for normal load variation. Contact surface mechanical properties are described by a friction coefficient μ, and stiffness coefficients k_t and k_n which characterise the elastic deformation of the asperities of the contacting surfaces in the tangential and normal directions, respectively. Moreover, an initial static normal force N_0 can also be prescribed. The values of μ, k_n and k_t are usually determined experimentally as described in [164] and are assumed to remain constant throughout the analysis. The initial normal contact condition, i.e. the normal load N_0 and normal gap g_0, are usually obtained via a nonlinear static analysis using a Finite Element software. The normal contact force f_n is expressed as follows:

$$f_\mathrm{n} = \begin{Bmatrix} N_0 + k_\mathrm{n} z & \text{for contact} \\ 0 & \text{for separation} \end{Bmatrix} \tag{2.5}$$

The tangential contact force is given by:

$$f_t = \begin{cases} f_t^0 + k_t(x - x_0) & \text{for stick} \\ \xi \mu f_n & \text{for slip} \\ 0 & \text{for separation} \end{cases} \qquad (2.6)$$

where ξ is a sign function of the tangential force at the time of slip state initiation. One of the key advantages of this friction element is that it allows varying normal load and lift-off phenomena during the analysis, which play a critical role in the nonlinear dynamic response of the structure.

However, these elements present one limitation which is that they do not capture micro-slip effects implicitly. A single friction element can only undergo three states: stick and macro-slip when there is contact, and separation. Although using a large number of these friction elements to discretise the contact area could potentially capture micro-slip behaviour, as shown in [166], the microslip effects can more easily be captured by using hysteretic laws as illustrated in Fig. 2.6. Microslip strongly affects the shape of the fretting loop and therefore strongly influences the energy dissipation at the contact interface, which makes it an essential feature for accurate fretting wear predictions. Common examples of hysteretic models include the Dahl [33], the LuGre [34], the Bouc-Wen [194], the Iwan [168], the Valanis [185] and the Preisach [187] models. The Valanis model is currently being implemented into FORSE and could potentially be used in the future for wear predictions. The main features of that model are described hereafter.

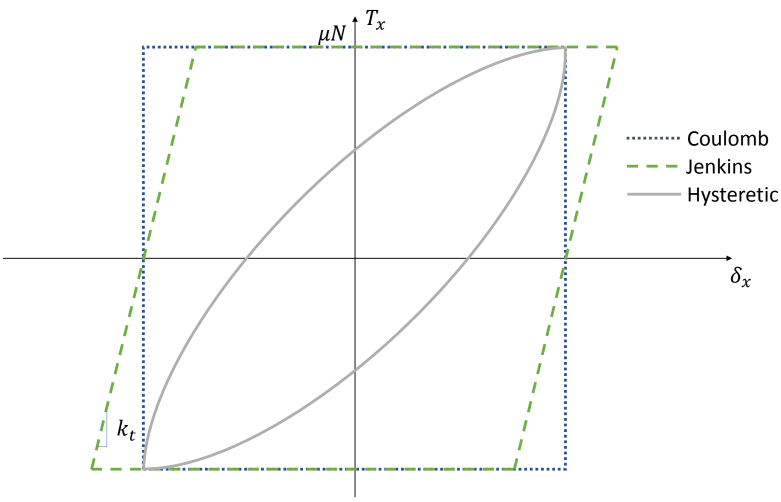

Fig. 2.6 Frictional hysteresis loop for different contact models

Valanis model

The Valanis model is an hysteretic model which was originally developed to describe the elasto-plastic behaviour of materials under cyclic loading conditions [185]. Since then, it has been successfully used in [53] to model the frictional hysteretic behaviour of a lap joint subject to harmonic excitation. In this approach, the friction limit is time-dependent which allows a full coupling between the tangential and normal relative displacements at the contact. The tangential friction force is defined as the solution to the following first order differential equation:

$$\dot{F} = E_0 \dot{q} \frac{1 + \frac{\lambda}{E_0} \frac{\dot{q}}{|q|} (E_t q - F)}{1 + k \frac{\lambda}{E_0} \frac{\dot{q}}{|q|} (E_t q - F)} = f(q, \dot{q}, F, \lambda) \tag{2.7}$$

where E_0 corresponds to the slope of the full stick region, which is the tangential contact stiffness, E_t is the slope of the macroslip region, k is a parameter which characterises the microslip transition, q is the contact tangential displacement, and λ is a parameter defined as:

$$\lambda = \frac{E_0}{\mu F_z(t)(1 - k\frac{E_t}{E_0})}$$

One of the advantages of the Valanis formulation is that, by defining a positive value for E_t, it allows to reproduce contact hysteresis loops in which the macroslip region has a slope. This contact behaviour has been observed experimentally in friction joints that are subject to fretting wear, as reported in [53, 167]. Another strong point of that model is that its parameters can easily be identified from a single hysteresis loop and an iterative fit of k, as shown in [127].

2.4.2 Numerical methods

Harmonic Balance Method (HBM)

In all assembled structures such as bladed discs, the equations of motion are nonlinear due to the frictional forces at the contact interfaces. There exist two main methods to solve these nonlinear equations. The first one is to perform a direct time integration of the equations of motion. This technique gives a high accuracy in the result, but is very time consuming. The faster alternative is to use the most common approximate method which is the harmonic balance method (HBM). This frequency-domain method proved to be useful for the analysis of systems having steady-state solutions [4, 64, 89, 129, 134, 176]. The harmonic balance method assumes a harmonic excitation consisting of a number of steady-state sinusoids and that the response of the system under such an excitation is also harmonic with the same frequency as that of excitation. The nonlinear forces and all the spatial variables are then expressed as truncated Fourier series, leading to a set of nonlinear algebraic equations by grouping the harmonic coefficients. Finally, the algebraic equations are solved by means of a standard iterative method, such as Newton-Raphson combined with a continuation scheme [137, 160]. Harmonic balance methods have been used to solve nonlinear dynamical problems for many years. Their application to various practical problems have been discussed in a number of papers [4, 64, 129, 134, 176]. Ferri and Dowell have done a significant amount of work in friction damping analysis using the HBM in [38, 40–42]. Whiteman and Ferri [196] used the HBM on a beam-like structure and compared the results obtained with exact time-domain methods. Griffin [63], Sinha [176], Petrov and Ewins [139] and Cigeroglu et al. [28] have applied the HBM and its extensions to the study of the forced response of gas turbine blades and discs. In the classical HBM, only the fundamental harmonics are taken into account. However, more harmonics must be considered for cases with strong nonlinearities for which the resonant frequencies of the system can be multiples of the fundamental excitation frequency [28]. The HBM formulated with multiple harmonics is called the multi-harmonic balance method (MHBM). Petrov and Ewins [134] used MHBM to develop a new friction model for bladed discs and they later included sticking and slipping transition times in the friction damping formulation [139]. Among other contributions, Süß and Willner [181] applied the MHBM to predict the dynamics of a bolted lap joint.

The Alternating Frequency-Time domain method (AFT)

The accurate evaluation of the nonlinear contact forces can be challenging with the harmonic balance method, and even more so with the MHBM. Research suggested that nonlinearities are more accurately solved in the time domain whereas the vibration problem as a whole is solved efficiently in the frequency domain. Based on that fact, Cameron and Griffin [22] introduced the alternating frequency-time domain method illustrated in Fig. 2.7. In this method, the nonlinear forces due to friction are calculated in time domain and transformed back into the frequency domain to be solved with the rest of the equation using simple Newton-like numerical schemes [116].

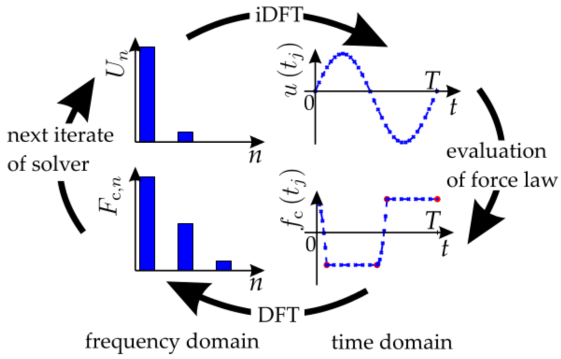

Fig. 2.7 Alternating frequency-time domain scheme [87]

Model reduction

The number of nodal degrees of freedom (DOF) of finite element models of a jointed structure such as a bladed disc can be considerable. In the industrial design process, typical numbers are in the order of magnitude of several millions, as shown in [131]. However, owing to the fact that nonlinear phenomena are usually very localised in specific areas such as the contact interfaces, model reduction can be used to reduce drastically the number of retained DOFs and therefore reduce to computational burden of the nonlinear dynamical analyses. Different techniques have been developed in the literature [11] although they are always based on classical modal analysis or on component mode synthesis (CMS) approach, the most popular CMS methods being the Craig-Bampton (CB) method [8] and the MacNeal-Rubin (MR) method [156].

2.5 Nonlinear dynamic wear analysis

Due to its complexity, there exist very few works on the coupling between fretting wear and vibrations. Jareland and Csaba [74] studied the effects of wear and mistuning on bladed disc vibrations. They used a simplified model consisting of beam elements for the blades and a rigid disc, as well as the bar model presented by Csaba [30] for the friction elements representing the underplatform dampers. The equations of motion are solved using the Harmonic Balance Method and wear is computed using the energy wear approach. For a tuned bladed disc, they showed that wear led to an increase of the resonance amplitude when macroslip is dominating and to a decrease of the resonance amplitude when microslip is dominating. For the mistuned case, they observed that the resonance amplitude increased slightly as the dampers got worn, which was supported by experimental results.

Petrov [133] also looked into the effects of wear on tuned and mistuned bladed discs. Based on the assessment of the frictional dissipated energy at all friction contact

interfaces, he simulated the progressive loss of the friction dampers. He showed that in the case of tuned blades, the amplitudes of resonance of the blade with the lost damper and the blades located next to it significantly increased, while the amplitude of the blades remote from the lost damper were barely affected. In the mistuned case, only the blades where the dampers were lost saw their forced response levels affected.
Salles et al. [157, 158] proposed a multiscale approach for the numerical treatment of fretting-wear under vibratory loading. In their approach, two separate time scales are used: a slow scale for tribological phenomena and a fast scale for dynamics. For a given number of vibration periods, a steady state is assumed and the variables are decomposed into Fourier series. An Alternating Frequency Time procedure is performed to calculate the nonlinear forces, after which a hybrid Powell solver is used. This work was the first to use numerical analysis to show the coupling between dynamic and tribological phenomena. They also showed that even with wear depths as small as a few microns, the vibratory response is greatly affected.
Other researchers worked on wear and vibrating systems, such as Levy [93], Sextro [171] or Pettigrew [141], but they focused more on the evaluation of wear resulting from the vibrations of the system, rather than the effects on wear on the dynamics.

2.6 Discussions

Wear modelling

Among all the methods available to solve a problem accounting for wear, the Finite Element Method coupled with Archard's law largely prevails, which can be easily explained by the following reasons. The FEM is widely used for engineering problems and many FEA commercial softwares are available; the wear law and automatic update of the geometry can be easily implemented through subroutines within these softwares; Archard's law is simple and straightforward to implement and, considering the number of experiments already performed, a large quantity of data (wear coefficients) is available to use this law. However, a few drawbacks of this method (FEM-Archard's law) must be pointed out: (i) Based on continuum mechanics, this approach is not ideal for modelling gross discontinuous material behaviour which occurs as a material wears out or fragments and new surfaces are created. (ii) The remeshing required to update the geometry of the contacting surfaces can be cumbersome and time-consuming. (iii) Archard's law does not integrate the coefficient of friction in its formulation. (iv) Considering the variability and the wide range of values for the Archard wear coefficient (10^{-7} to 10^{-2}), caution must be exercised if one intends to select an existing wear coefficient. Coupling the FEM with the energy wear approach enables to take into account the influence of the coefficient of friction. Furthermore, the energy wear approach has received more and more attention from the researchers and it is also very easy to implement, which makes it a promising alternative to the use Archard's law.

The use of the Boundary Element Method coupled with Archard's law reduces drastically the computational time of the remeshing. Another strong point of the BEM is that it provides the same accuracy for both stresses and displacements, which is a key advantage for wear computations. Despite these two advantages, this method presents two major drawbacks that excluded it from the present research. The first one is that, due to the use of fully populated nonsymmetric matrices, the BEM is not compatible with Finite Element solvers which are primarily designed to deal with sparse symmetric matrices. The second one is the compatibility of the BEM with dynamics calculations which seems challenging and has never been demonstrated, to the best knowledge of the author.

The Finite Discrete Element coupled with either Archard's law or the energy wear approach looks very promising since it makes it possible to model the two contacting bodies but also the wear particles, their evolution and their impact on the whole system. Despite this indisputable advantage, the main challenge of this approach is the determination of a valid interaction law between particles. Furthermore, the ease of implementation may also prove to be a major difficulty in an environment with no background in the Discrete Element Method.

Despite its theoretical ability to describe the behaviour of the contact interface at the microscopic level, by taking the wear particles into account and requiring no wear law nor friction model, the thermodynamics approach still seems far from being usable in industrial environment. The main reason for that is that most of the works that have been conducted on this approach are only giving a theoretical and very complex framework. Furthermore, the governing models comprise a very large number of parameters and variables. Among them, the free energy is probably the most difficult to obtain. As for the few existing experimental studies, they are centred on the entropy which is as much challenging to determine.

Again, theoretically, the Molecular Dynamics method is able to describe accurately the friction and wear process at the contact interface by modelling the interactions between each constitutive atoms, hence without any wear law nor friction model. However, it presents an obvious limiting drawback for the present work: the space and time scales imply extremely large computational times and storage requirements, which are not compatible with the current computational power at hand.

The Movable Cellular Automata, by modelling the system by interacting discrete elements, is able to describe several phenomena taking place in the contact area such as plastic deformation, mass transfer, oxidation or mixing of materials. The major difficulty is the determination of the interaction laws between the particles.

Similarly, the successful application of the SPH method pertains to the selection of appropriate constitutive equations that require the definition of a number of parameters. Furthermore, the computational times and storage requirements for SPH simulations are very large, which is another limiting factor for its application to fretting wear analysis.

So far, the X-FEM method has been mostly used for crack propagation study without considering the frictional contact between the crack lips. Despite some works on the application of the method to frictional contact, its ability to accurately capture stick-slip phenomena remains to be proved. Furthermore, in the context of fretting wear analysis, a refinement of the underlying finite element mesh would still be required in order to extract a fine description of the contact conditions necessary for the computation of wear.

The use of a Semi-Analytical Method (SAM) within a multiscale approach appears to be the most promising method for fretting wear predictions. SAM allows to make a zoom of the contact area, refine the mesh and extract accurate contact conditions (pressure, shear and slip distributions) which are key inputs for wear computation. All of this is done with a very low computational time compared to FEM, which means that using this approach, one can benefit of the advantages of the FEM-Archard's law approach with a much more accurate wear computation and with an acceptable computational cost. It should be noted, however, that this approach presents two shortcomings: (a) it does not take into account the influence of the third body and (b) it is based on the elastic half-space assumption which may affect the accuracy depending upon the problem at hand, as will be discussed in the third chapter of this thesis.

Nonlinear dynamics analysis

Considering the environment of the present research and the sponsorship of Rolls-Royce plc., the in-house nonlinear solver, FORSE, has been used to perform all the nonlinear dynamic analyses in the course of this PhD. Nevertheless, the proposed multiscale approach could also be coupled with other nonlinear solvers. In particular, the implemented contact solver could also be used to tune micro-slip models such as the Iwan or the Valanis models, as will be discussed in the final chapter of this thesis.

Nonlinear dynamics and wear

As highlighted in section 2.5 of this chapter, very few researchers have studied the coupling between fretting wear and nonlinear dynamics. The most advanced works are the ones conduced by Salles et al. [157, 158]. There are two major differences between these previous works and the present research: the first one lies in the additional use of two separate space scales: a macro-scale for the dynamic analysis and a micro-scale for the contact analysis and wear computation, which allows a better discretisation of the contact area and hence a higher accuracy. The second one is the tuning of the macro-slip friction elements using the developed contact solver.

Chapter 3

A contact solver based on boundary integral equations

3.1 Introduction

This chapter presents the development of the contact solver based on boundary integral equations. There are two main motivations for the development of such a solver. The first one is to provide accurate contact conditions, which are essential for fretting wear computation, at a low computational cost. The second motivation is the need to identify the parameters of the friction elements used in the nonlinear dynamic model in order to have a better local description of the contact and allow to capture specific local features such as the ones due to surface roughness. The first part of the chapter is dedicated to the theoretical aspects of the elastic contact. The objective here is to provide the reader with all the necessary background information to understand the key components of the developed contact solver, and to lay ground for its own implementation. In the second part, the numerical solutions of the contact problems and their implementation are described in detail. The idea here is to further allow the reader to reproduce the code implemented in this work, thereby addressing the lack of consistency in the existing literature. The verifications of the code against analytical solutions are the subject of the third part of this chapter. Finally, a discussion on the effects of the half-space assumption based on comparisons between the contact solver results and those obtained from the classical Finite Element Method is proposed. These comparisons also demonstrate the computational benefits of the solver.

3.2 Elastic contact theory

3.2.1 Elastic half-space

Based on the geometry of the contact area, two types of contact can be distinguished: conforming contacts and non-conforming contacts. A contact is said to be conforming if the surfaces of the two bodies fit exactly together without deformation [77]. If the contacting surfaces are dissimilar, then the contact is said to be non-conforming. The contact area between non-conforming bodies is generally small compared to the overall dimensions of the bodies. The contact stresses are therefore concentrated near the contact region and decrease rapidly with distance from the point of contact, so that the area of interest lies close to the contact interface. Thus, provided the dimensions of the bodies in contact are large compared to the dimensions of the contact area, the stresses in the region do not depend on the shape of the bodies distant from the contact area, nor on their boundary conditions. The stresses may be calculated to good approximation by considering each body as a semi-infinite elastic solid bounded by a plane surface, i.e. an elastic half-space. This idealisation, in which bodies of arbitrary surface profile are regarded as semi-infinite in extent and having a plane surface, is made almost universally in elastic contact stress theory. It simplifies the boundary conditions and makes available the large body of elasticity theory which has been developed for the elastic half-space. The following assumptions are also made:

- The semi-infinite bodies are homogeneous and isotropic.
- Deformations are small.
- There is a linear relationship between stresses and strains.
- The surfaces in contact are continuous and non-conforming.

Under this idealisation, analytical solutions which link the pressure and shear fields to the elastic deflections at the contact surface, can be used. Normal tractions $p(x,y)$ and tangential tractions $q_x(x,y)$ and $q_y(x,y)$ are applied to a closed surface S close to the origin, as depicted in Fig. 3.1. Neumann's problem consists in finding the elastic deflections u_x, u_y and u_z and stresses σ of components σ_x, σ_y, σ_z, τ_{xy}, τ_{yz} and τ_{zx}. The theory of potentials has been used by Boussinesq [15] and Cerruti [24] in order to solve this problem when considering a punctual force. This work has been extended by Love [98] to a rectangular surface $\Delta_x \times \Delta_y$ of center O and normally loaded using a constant pressure p, and by Vergne [186] to a constant shear q_x or q_y. Other valuable contributions are due to Galin [49], Lur'e [104] and Muskhelishvili [114] and are expressed in [77]. When body forces are neglected, Navier's equation reduces to the

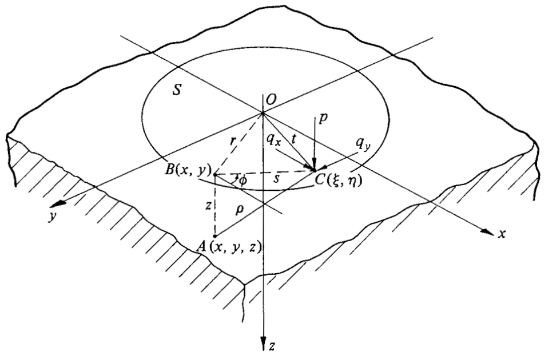

Fig. 3.1 Elastic half-space under normal and tangential loadings [77]

following Laplace's equation:

$$\nabla^2 \boldsymbol{u} = 0, \tag{3.1}$$

where ∇ is the Nabla operator. In order to satisfy Laplace's equation, the displacements $\boldsymbol{u}$ are expressed using bi-harmonic functions. They must also verify the boundary conditions in terms of displacements and loadings.

In what follows, we consider a loaded point C(ξ,η) on the surface and A(x,y,z) a point within the half-space. The distance between those two points is given by:

$$CA = \rho = \sqrt{(\xi - x)^2 + (\eta - y)^2 + z^2}.$$

The following potential functions, each satisfying Laplace's equation, are defined:

$$F_1 = \iint_S q_x(\xi,\eta)\Omega d\xi d\eta, \tag{3.2}$$

$$G_1 = \iint_S q_y(\xi,\eta)\Omega d\xi d\eta, \tag{3.3}$$

$$H_1 = \iint_S p(\xi,\eta)\Omega d\xi d\eta, \tag{3.4}$$

where $\Omega = z\ln(\rho + z) - \rho$.

$$F = \frac{\partial F_1}{\partial z} = \iint_S q_x(\xi,\eta)\ln(\rho + z) d\xi d\eta, \tag{3.5}$$

$$G = \frac{\partial G_1}{\partial z} = \iint_S q_y(\xi,\eta)\ln(\rho + z) d\xi d\eta, \tag{3.6}$$

$$H = \frac{\partial H_1}{\partial z} = \iint_S p(\xi,\eta)\ln(\rho + z) d\xi d\eta. \tag{3.7}$$

We now write:

$$\psi_1 = \frac{\partial F_1}{\partial x} + \frac{\partial G_1}{\partial y} + \frac{\partial H_1}{\partial z}, \tag{3.8}$$

$$\psi = \frac{\partial \psi_1}{\partial z} = \frac{\partial F}{\partial x} + \frac{\partial G}{\partial y} + \frac{\partial H}{\partial z}. \tag{3.9}$$

Love [98] proved that the elastic deflections u_x, u_y and u_z at the point A(x,y,z) can be expressed as follows:

$$u_x = \frac{1}{4\pi G}\left\{2\frac{\partial F}{\partial z} - \frac{\partial H}{\partial x} + 2\nu\frac{\partial \psi_1}{\partial x} - z\frac{\partial \psi}{\partial x}\right\}, \tag{3.10}$$

$$u_y = \frac{1}{4\pi G}\left\{2\frac{\partial G}{\partial z} - \frac{\partial H}{\partial y} + 2\nu\frac{\partial \psi_1}{\partial y} - z\frac{\partial \psi}{\partial y}\right\}, \tag{3.11}$$

$$u_z = \frac{1}{4\pi G}\left\{2\frac{\partial F}{\partial z} - (1-2\nu)\psi - z\frac{\partial \psi}{\partial z}\right\}. \tag{3.12}$$

Solutions of equations 3.10, 3.11 and 3.12 provide the surface elastic deflections at point A for both normal and tangential loadings applied in point C. In the following equations, subscript J may describe x, y or z.
The contributions of the pressure p on the elastic deflections on the surface are given by:

$$\begin{aligned}\frac{\bar{u_J}}{p} = K_J^p(x,y,E,\nu) &= U_J^p(x+\frac{\Delta x}{2}, y+\frac{\Delta y}{2}, E,\nu) + U_J^p(x-\frac{\Delta x}{2}, y-\frac{\Delta y}{2}, E,\nu)\\ &- U_J^p(x+\frac{\Delta x}{2}, y-\frac{\Delta y}{2}, E,\nu) - U_J^p(x-\frac{\Delta x}{2}, y+\frac{\Delta y}{2}, E,\nu),\end{aligned} \tag{3.13}$$

where

$$U_x^p = \frac{(1+\nu)(1-2\nu)}{2\pi E}\left[2x\arctan\left(\frac{\rho-y}{x}\right) - y\ln(\rho)\right], \tag{3.14}$$

$$U_y^p = \frac{(1+\nu)(1-2\nu)}{2\pi E}\left[2y\arctan\left(\frac{\rho-x}{y}\right) - x\ln(\rho)\right], \tag{3.15}$$

$$U_z^p(x,y,E,\nu) = \frac{(1-\nu^2)}{\pi E}\left[y\ln(\rho+x) + x\ln(\rho+y)\right], \tag{3.16}$$

with $\rho = \sqrt{x^2+y^2}$. E and ν are the Young's modulus and the Poisson ratio of the material.
The contributions of the shear q_x on the elastic deflections on the surface are given by:

$$\begin{aligned}\frac{\bar{u_J}}{q_x} = K_J^{q_x}(x,y,E,\nu) &= U_J^{q_x}(x+\frac{\Delta x}{2}, y+\frac{\Delta y}{2}, E,\nu) + U_J^{q_x}(x-\frac{\Delta x}{2}, y-\frac{\Delta y}{2}, E,\nu)\\ &- U_J^{q_x}(x+\frac{\Delta x}{2}, y-\frac{\Delta y}{2}, E,\nu) - U_J^{q_x}(x-\frac{\Delta x}{2}, y+\frac{\Delta y}{2}, E,\nu),\end{aligned} \tag{3.17}$$

where

$$U_x^{q_x} = \frac{1-\nu^2}{\pi E} x \ln(\rho + y) + \frac{1+\nu}{\pi E} \left[y \ln(\rho + x) - y \right], \tag{3.18}$$

$$U_y^{q_x} = -\frac{\nu(1+\nu)}{\pi E} \rho, \tag{3.19}$$

$$U_z^{q_x} = \frac{(1+\nu)(1-2\nu)}{2\pi E} \left[-2x \arctan\left(\frac{\rho - y}{x}\right) + y \ln(\rho) \right]. \tag{3.20}$$

The contributions of the shear q_y on the elastic deflections on the surface are given by:

$$\begin{aligned} \frac{\bar{u_J}}{q_y} = K_J^{q_y}(x,y,E,\nu) = U_J^{q_y}(x+\frac{\Delta x}{2}, y+\frac{\Delta y}{2}, E, \nu) + U_J^{q_y}(x-\frac{\Delta x}{2}, y-\frac{\Delta y}{2}, E, \nu) \\ - U_J^{q_y}(x+\frac{\Delta x}{2}, y-\frac{\Delta y}{2}, E, \nu) - U_J^{q_y}(x-\frac{\Delta x}{2}, y+\frac{\Delta y}{2}, E, \nu), \end{aligned} \tag{3.21}$$

where

$$U_x^{q_y} = -\frac{\nu(1+\nu)}{\pi E} \rho, \tag{3.22}$$

$$U_y^{q_y} = \frac{1-\nu^2}{\pi E} y \ln(\rho + x) + \frac{1+\nu}{\pi E} \left[x \ln(\rho + y) - x) \right], \tag{3.23}$$

$$U_z^{q_x} = \frac{(1+\nu)(1-2\nu)}{2\pi E} \left[-2y \arctan\left(\frac{\rho - x}{y}\right) + x \ln(\rho) \right]. \tag{3.24}$$

3.2.2 Discretisation of the contacting bodies

The potential contact area A_P is discretised into a regular grid of $N_x \times N_y$ points. The spacing between each point is Δ_x along the x direction and Δ_y along the y direction. Thus, each point is in the center of a rectangular area of surface $S = \Delta_x \Delta_y$ on which a constant pressure and shear field is applied, as illustrated in Fig. 3.2. Each point (i, j) is defined by its coordinates (x, y). The elastic deflections at each point are found by superimposing contributions of each element of the surface, using the coefficients of influence expressed in the previous section. However, elastic deflections found in the contact depend on elastic deflections of both elastic half-spaces. It must be noticed that, by definition, $p = p_1 = p_2$, $q_x = q_{x1} = -q_{x2}$ and $q_y = q_{y1} = -q_{y2}$, which leads

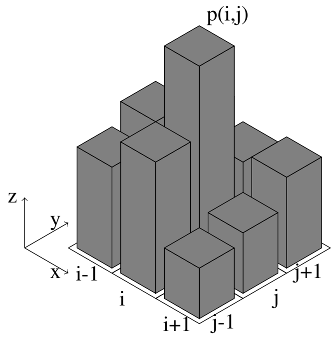

Fig. 3.2 Constant pressure on rectangular elements

to the following total normal and tangential displacements (with $J = x$ or y):

$$\begin{aligned} u_z(x_i,y_j) = &\sum_{l=1}^{N_x}\sum_{m=1}^{N_y} p(x_k,y_l)(K_z^p(x_l-x_i,y_m-y_j,E_1,\nu_1)+K_z^p(x_l-x_i,y_m-y_j,E_2,\nu_2)) \\ &+\sum_{l=1}^{N_x}\sum_{m=1}^{N_y} q_x(x_k,y_l)(K_z^{q_x}(x_l-x_i,y_m-y_j,E_1,\nu_1)-K_z^{q_x}(x_l-x_i,y_m-y_j,E_2,\nu_2)) \\ &+\sum_{l=1}^{N_x}\sum_{m=1}^{N_y} q_y(x_k,y_l)(K_z^{q_y}(x_l-x_i,y_m-y_j,E_1,\nu_1)-K_z^{q_y}(x_l-x_i,y_m-y_j,E_2,\nu_2)), \end{aligned} \tag{3.25}$$

$$\begin{aligned} u_J(x_i,y_j) = &\sum_{l=1}^{N_x}\sum_{m=1}^{N_y} p(x_k,y_l)(K_J^p(x_l-x_i,y_m-y_j,E_1,\nu_1)-K_J^p(x_l-x_i,y_m-y_j,E_2,\nu_2)) \\ &+\sum_{l=1}^{N_x}\sum_{m=1}^{N_y} q_x(x_k,y_l)(K_J^{q_x}(x_l-x_i,y_m-y_j,E_1,\nu_1)+K_J^{q_x}(x_l-x_i,y_m-y_j,E_2,\nu_2)) \\ &+\sum_{l=1}^{N_x}\sum_{m=1}^{N_y} q_y(x_k,y_l)(K_J^{q_y}(x_l-x_i,y_m-y_j,E_1,\nu_1)+K_J^{q_y}(x_l-x_i,y_m-y_j,E_2,\nu_2)). \end{aligned} \tag{3.26}$$

From these expressions, it can be seen that when the two contacting bodies have the same material properties, i.e. when $E_1 = E_2$ and $\nu_1 = \nu_2$, the contributions of the shear fields on the normal displacements, and the contributions of the pressure field on the tangential displacements are nil. The normal and tangential problems are then said to be uncoupled and therefore can be solved separately. However, it should be noted that due to the Coulomb friction law, the tangential problem always depends on the solution of the normal problem.

3.2.3 Normal contact problem

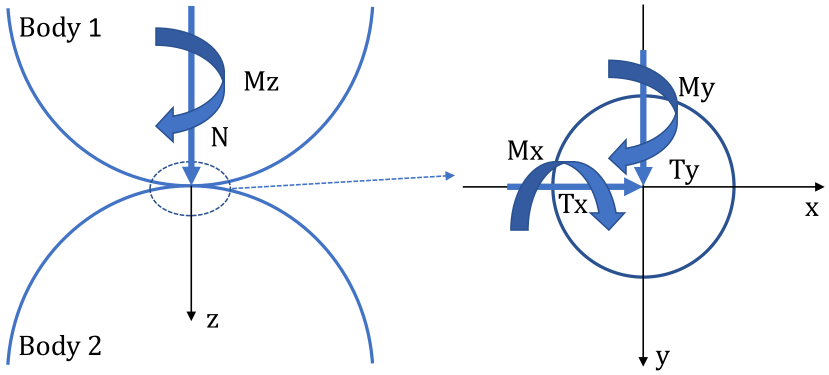

Fig. 3.3 Contact between two elastic half-spaces

The normal contact problem, illustrated in Fig. 3.3, consists in finding the pressure fields p_{ij} at the grid point (i, j), the normal elastic deflections u_{zij}, the contact area A_{C}, the rigid body displacement δ_z and the gap between the contacting bodies g_{ij}, while verifying the contact conditions described hereafter. The input parameters are the applied normal load N, the potential contact area A_{P} which must be larger than A_{C} and the initial separation between the contacting bodies h_{ij}. Solving the normal contact problem consists in finding the pressure distribution that gives a closed gap in the contact area and an open gap outside the contact area:

$$\begin{aligned} p_{ij} \geq 0,\ g_{ij} = 0,\ (i,j) \in A_{\mathrm{C}}, \\ p_{ij} = 0,\ g_{ij} \geq 0,\ (i,j) \notin A_{\mathrm{C}}, \end{aligned} \tag{3.27}$$

where $g_{ij} = u_{zij} + h_{ij} - \delta_z - y_j\phi_x + x_i\phi_y$.
$y_j\phi_x$ and $x_i\phi_y$ are the displacements resulting from small rigid body rotations ϕ_x and ϕ_y which appear when bending moments M_x and M_y are also transmitted through the contact.
The pressure fields must also verify the force and moment equilibrium equations:

$$\begin{aligned} \sum_{(i,j)\in A_{\mathrm{P}}} p_{ij}S = N, \\ \sum_{(i,j)\in A_{\mathrm{P}}} y_j p_{ij}S = -M_x, \\ \sum_{(i,j)\in A_{\mathrm{P}}} x_i p_{ij}S = M_y. \end{aligned} \tag{3.28}$$

3.2.4 Tangential contact problem

The tangential contact problem consists in finding the shear fields q_x and q_y, the relative tangential displacement fields u_x and u_y, the slipping region A_{SL}, the sticking region A_{ST} which is such that $A_{\mathrm{C}} = A_{\mathrm{SL}} \cup A_{\mathrm{ST}}$, the tangential rigid body displacements δ_x and δ_y and the slip fields s_x and s_y. The shear and slip fields must obey the Coulomb friction law, leading to the following constraint equations:

$$\begin{aligned} &\sqrt{q_x^2+q_y^2} \leq \mu p, \quad \sqrt{s_x^2+s_y^2} = 0, \quad (x,y) \in A_{\mathrm{ST}}, \\ &\sqrt{q_x^2+q_y^2} = \mu p, \quad \sqrt{s_x^2+s_y^2} \geq 0, \quad (x,y) \in A_{\mathrm{SL}}, \end{aligned} \tag{3.29}$$

where μ denotes the friction coefficient, A_{ST} the stick element set and A_{SL} the slip element set.
s_x and s_y are given by:

$$\begin{bmatrix} s_x \\ s_y \end{bmatrix} = \begin{bmatrix} u_x \\ u_y \end{bmatrix} - \begin{bmatrix} \delta_x + y\phi_z \\ \delta_y - x\phi_z \end{bmatrix}, \tag{3.30}$$

where ϕ_z is the rigid body rotation around the z direction and δ_x and δ_y are the rigid body translations along the x and y directions, respectively.
The equilibrium in terms of tangential loads is given by:

$$\begin{aligned} \sum_{(i,j)\in A_{\mathrm{P}}} q_{xij} S &= T_x, \\ \sum_{(i,j)\in A_{\mathrm{P}}} q_{yij} S &= T_y, \\ \sum_{(i,j)\in A_{\mathrm{P}}} \left(x_i q_{yij} - y_j q_{xij}\right) S &= M_z. \end{aligned} \tag{3.31}$$

The shear tractions q_x and q_y computed from the contact solver, must verify these equilibrium equations.

3.2.5 Weak formulations

Finding the solution to the contact problems previously described consists in minimizing the total complementary energy of the system, with the constraint that the pressure fields must be positive or equal to zero and the shear fields must obey the Coulomb friction law, leading to:

$$\begin{aligned} &\min \int_{A_{\mathrm{C}}} \left(h^* + \frac{1}{2}u_z\right) p dS + \int_{A_{\mathrm{C}}} \left(\mathbf{W}_\tau^* + \frac{1}{2}\mathbf{u}_\tau^t - \mathbf{u}_\tau^{t-1}\right) \mathbf{q} dS, \\ &p \geq 0, \\ &\|\mathbf{q}\| \leq \mu p, \end{aligned} \tag{3.32}$$

where h^* is the separation between the undeformed contacting bodies, including the initial separation and the rigid body displacements resulting from translations and rotations. Similarly $\mathbf{W}_\tau^*$ is the vector of the tangential displacements resulting from the rigid body motions. If we now assume that the normal and tangential problems are uncoupled, and if we use the discretisation and the influence coefficients previously described, Eq. 3.32 becomes, for the normal problem:

$$\begin{gathered}\min\left(\frac{1}{2}\mathbf{p}^\mathsf{T}\mathbf{K}_z^\mathbf{p}p + \mathbf{h}^{*\mathsf{T}}\mathbf{p} + c_\tau\right), \\ p_{ij} \geq 0\end{gathered} \tag{3.33}$$

where c_τ is the complementary energy of the tangential problem given by:

$$c_\tau = \frac{1}{2}q^\mathsf{T}K_\tau^q q + \left(-\Delta\delta_\tau^\mathsf{T} - \mathbf{u}_\tau^{t-1}\right)q.$$

As for the tangential problem, we obtain:

$$\begin{gathered}\min\left(\frac{1}{2}q^\mathsf{T}A_\tau^q q + W^{*\mathsf{T}}q + c_\mathrm{p}\right), \\ \left\|\mathbf{q_{ij}}\right\| \leq \mu p_{ij},\end{gathered} \tag{3.34}$$

where c_p is the complementary energy of the normal problem given by:

$$c_\mathrm{p} = \frac{1}{2}p^\mathsf{T}K_z^p p + (h - \delta_z)^* p.$$

Equations 3.33 and 3.34 show that the normal and tangential problems can be seen as the minimization of constrained quadratic forms. Polonsky and Keer [143] proposed a computationally efficient algorithm based on the conjugate gradient method (CGM) to minimize quadratic forms, which is why it has been used in the present work.
The conjugate gradient method and the discrete convolution - fast Fourier transform (DC-FFT) technique, which are two key components of the algorithm, will be introduced in the following section, after which the solutions of the normal and tangential contact problems will be presented.

3.3 Numerical solutions

3.3.1 Conjugate gradient method

The conjugate gradient method is used to solve both the normal and tangential contact problems in the present work. It dates back to the 50s and was initially proposed by

Hestenes and Stiefel [66]. This is an iterative method to solve the linear problems:

$$Ax = b, \tag{3.35}$$

where A is a $N \times N$ symmetric and positive definite matrix. This problem is equivalent to the minimization of the following quadratic form:

$$\varphi(x) = \frac{1}{2}x^{\mathsf{T}}Ax - b^{\mathsf{T}}x. \tag{3.36}$$

The conjugate gradient method (CGM) can therefore be seen as a method to solve linear systems or a technique to minimize convex quadratic forms. The gradient of φ is the residual of the linear system:

$$\nabla\varphi(x) = Ax - b = r(x). \tag{3.37}$$

The solution is obtained by making successive steps of length α_k in the descent directions p_k:

$$x_{k+1} = x_k + \alpha_k p_k. \tag{3.38}$$

The conjugate gradient method is a derivative of the conjugate descent method. All descent direction vectors p_k are conjugate between each other with respect to the linear application described by the positive definite matrix A, i.e. $p_i^{\mathsf{T}}Ap_j = 0$ for every $i \neq j$. This makes it an exact method which allows the minimization of φ in N iterations. The method is computationally effective and does not require much memory: in each iteration, the current conjugate direction is obtained from the preceding direction p_{k-1} alone. Therefore there is no need to store the previous iterations. More precisely, the new descent direct is the linear combination of the previous descent direction and the steepest descent which is $-\nabla\varphi(x_k) = -r_k$:

$$p_k = -r_k + \beta_k p_{k-1}, \tag{3.39}$$

where β_k is such that the conjugate condition is verified, i.e. $p_{k-1}^{\mathsf{T}}Ap_k = 0$.
The algorithm is as follows:

Adopt an initial guess for x_0
Initialise the variables: $r_0 \leftarrow Ax_0 - b$, $p_0 \leftarrow -r_0$, $k \leftarrow 0$
while $r_k \neq 0$ **do**

$$\begin{aligned}
\alpha_k &\leftarrow \frac{r_k^\mathsf{T} r_k}{p_k^\mathsf{T} A p_k} \\
x_{k+1} &\leftarrow x_k + \alpha_k p_k \\
r_{k+1} &\leftarrow r_k + \alpha_k A p_k \\
\beta_{k+1} &\leftarrow \frac{r_{k+1}^\mathsf{T} r_{k+1}}{r_k^\mathsf{T} r_k} \\
p_{k+1} &\leftarrow -r_{k+1} + \beta_{k+1} p_k \\
k &\leftarrow k+1
\end{aligned}$$

end while

The CGM can also be used to solve a linear system with constraints.

As seen before, the surface displacements are computed using the influence coefficients method. In the case of the normal problem, assuming a contact between two bodies of similar material, the surface normal displacement reduces to:

$$u_{zij} = \sum_{N_x} \sum_{N_y} p_{kj} K z_{ijkl} = K_z \otimes p, \tag{3.40}$$

where $\otimes$ denotes the discrete convolution product.

Assuming $N_x = N_y = N$, the number of operations required to compute this double sum is $\mathscr{O}(N^2)$. Therefore, for a large contact grid, the computational cost may become prohibitive, which justifies the need for acceleration techniques. To this end, the Discrete Convolution and Fast Fourier Transform, or DC-FFT has been proposed [78, 144]. This technique, presented is the following section, allows the computation of each double sum in $\mathscr{O}(N\log(N))$ operations.

3.3.2 DC-FFT technique

For continuous systems where all variables are continuous functions of time or location, Fourier analysis is a very powerful tool to tackle complicated problems [7]. With an input, $x(t)$, the output, $y(t)$, of a linear continuous system can be expressed as

$$y(t) = \int_{-\infty}^{+\infty} x(\tau) h(t-\tau) d\tau = x(t) * h(t), \tag{3.41}$$

where $y(t)$ is the linear convolution of $x(t)$ and $h(t)$, and $h(t)$ is a unit impulse response, which corresponds to a Green's function in contact problems. The variable t can be in the temporal and spatial domain. The continuous convolution theorem indicates that applying the Fourier transform (FT) to both sides of Eq. 3.41 should result in an equation with simple multiplication:

$$\tilde{y}(\omega) = \tilde{h}(\omega)\tilde{x}(\omega), \tag{3.42}$$

where $\tilde{y}$ denotes the Fourier transform of the variable y. The linear convolution for contact problems should be discretely converted into the cyclic convolution that can be efficiently and accurately handled by the DC-FFT method. The techniques of zero padding and wrap-around order are the necessary treatments for properly converting the linear convolution into the cyclic convolution [149]. The full procedure, as proposed by Liu [97], is as follows:

1. Compute the influence coefficients $\left\{K_j\right\}_N$
2. Expand $\left\{K_j\right\}_N$ into $\left\{K_j\right\}_{2N}$ using zero-padding and wrap-around order
3. Apply FFT to $\left\{K_j\right\}_{2N}$ and obtain $\left\{\hat{K}_s\right\}_{2N}$
4. Input pressure fields $\left\{p_j\right\}_N$
5. Expand pressure fields $\left\{p_j\right\}_N$ into $\left\{p_j\right\}_{2N}$ using zero-padding and wrap-around order
6. Apply FFT to $\left\{p_j\right\}_{2N}$ and obtain $\{\hat{p}_s\}_{2N}$
7. Compute the element-wise product in the frequency domain $\{\hat{u}_s\}_{2N} = \left\{\hat{K}_s\right\}_{2N}\{\hat{p}_s\}_{2N}$
8. Apply the iFFT to $\{\hat{u}_s\}_{2N}$ to obtain $\left\{u_j\right\}_{2N}$
9. Discard the spoiled terms and keep $\left\{u_j\right\}_{2N}$, $j \in [0, N-1]$

Zero-padding: nil pressures from N to $2N-1$ are added to the pressure distribution defined from 0 to $N-1$.
Wrap-around order: the influence coefficients are computed from 0 to $N-1$. The coefficient for N is set to 0. The coefficients from $N+1$ to $2N-1$ are obtained from the coefficients from 1 to $N-1$ but sorted in reverse order. A negative sign is applied to those extended coefficients if the influence coefficients function is odd.
Those two numerical treatment are depicted in Fig. 3.4.

3.3.3 Numerical solution of the uncoupled contact problem

A survey of the available literature about FFT and BEM-based contact solvers showed that all the necessary steps have been developed in the past and are available, but the

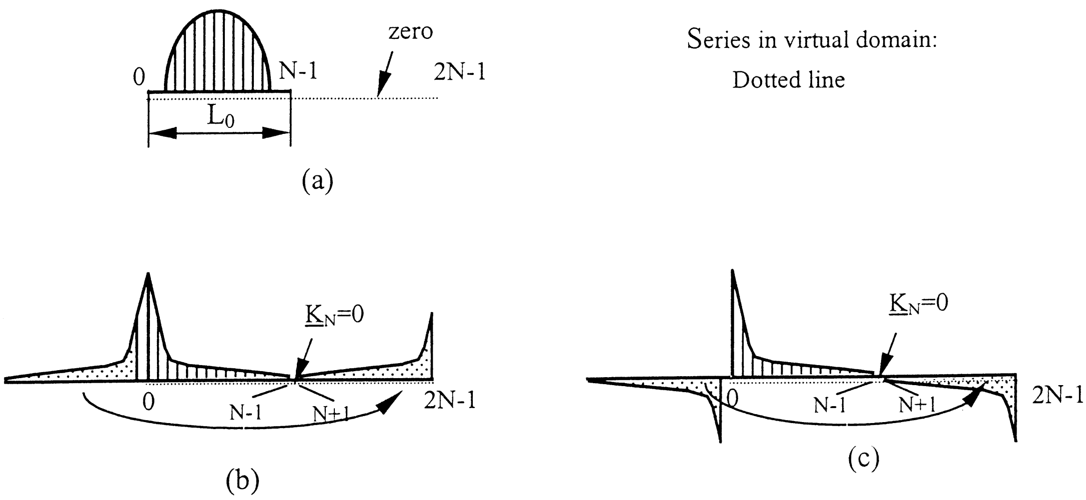

Fig. 3.4 Zero padding and wrap-around order. (a) Pressure distribution; (b) influence coefficients for normal pressure; (c) influence coefficients for tangential pressure. [97].

lack of a consistent implementation into a single framework prevented the successful application in a non academic environment. To overcome this lack of information, the implementation that was done in the present work is described in detail, therefore providing a readily usable solver. The presented procedure is mainly based on [50, 177] with a series of modifications to make it work for all the considered test cases. Given the similarities between the way the normal and tangential problems are solved, they are presented together. However, it is worth noting that the present work only considers the contact between similar elastic materials. Therefore, the normal and the tangential contact problems are uncoupled and can be solved separately. This assumption is valid for a large number of friction joints in aircraft engines which are based on steel-on-steel contact. In the normal problem, the entire grid A_{P} is assumed to be initially in contact. The actual contact area A_{C} and pressure p are obtained once the convergence of the numerical procedure is reached. These data are then used as inputs for solving the tangential problem in which the contact area is divided into two different regions: a stick region A_{ST} and a slip region A_{SL}. The implemented procedure is as follows:

1. The pressure p and shear q distributions for every point (i,j) of the grid are initialised using the following forms:

$$p(i,j) = a_{\mathrm{p}} + b_{\mathrm{p}}x(i) + c_{\mathrm{p}}y(j) \tag{3.43}$$

$$\begin{aligned} q_x(i,j) &= a_{\mathrm{q}} - c_{\mathrm{q}}y(j) \\ q_y(i,j) &= b_{\mathrm{q}} + c_{\mathrm{q}}x(i) \end{aligned} \tag{3.44}$$

The coefficients a_p, b_p and c_p are calculated using Eq. 3.43 and the equilibrium equations Eq. 4.6, leading to:

$$\begin{bmatrix} a_\mathrm{p} \\ b_\mathrm{p} \\ c_\mathrm{p} \end{bmatrix} = \frac{1}{S}\mathbf{M}_\mathrm{p}^{-1} \begin{bmatrix} N \\ M_y \\ -M_x \end{bmatrix}, \tag{3.45}$$

where

$$\mathbf{M}_\mathrm{p} = \sum_{(i,j)\in A_\mathrm{C}} \begin{bmatrix} 1 & x(i) & y(j) \\ x(i) & x(i)^2 & x(i)y(j) \\ y(j) & x(i)y(j) & y(j)^2 \end{bmatrix}.$$

The coefficients a_q, b_q and c_q are calculated using Eq. 3.44 and the equilibrium equations 3.31, leading to:

$$\begin{bmatrix} a_\mathrm{q} \\ b_\mathrm{q} \\ c_\mathrm{q} \end{bmatrix} = \frac{1}{S}\mathbf{M}_\mathrm{q}^{-1} \begin{bmatrix} T_x \\ T_y \\ M_z \end{bmatrix}, \tag{3.46}$$

where

$$\mathbf{M}_\mathrm{q} = \sum_{(i,j)\in A_\mathrm{ST}} \begin{bmatrix} 1 & 0 & y(j) \\ 0 & 1 & x(i) \\ y(j) & x(i) & x(i)^2+y(j)^2 \end{bmatrix}$$

2. The DC-FFT method is applied to the computation of the normal elastic displacements u_z and the tangential elastic displacements u_x and u_y.

3. The rigid body translation δ_z and the rigid body rotations ϕ_x and ϕ_y, around the x and y directions, respectively, can be obtained from the following system of equations:

$$\begin{bmatrix} \delta_z \\ \phi_x \\ \phi_y \end{bmatrix} = \mathbf{N}_\mathrm{p}^{-1} \sum_{(i,j)\in A_\mathrm{C}} \begin{bmatrix} u_z(i,j)+h(i,j) \\ u_z(i,j)+h(i,j)y(j) \\ u_z(i,j)+h(i,j)x(i) \end{bmatrix}, \tag{3.47}$$

where

$$\mathbf{N}_\mathrm{p} = \sum_{(i,j)\in A_\mathrm{C}} \begin{bmatrix} 1 & y(j) & x(i) \\ y(j) & y(j)^2 & x(i)y(j) \\ x(i) & x(i)y(j) & x(i)^2 \end{bmatrix}.$$

The rigid body translations δ_x and δ_y and the rigid body rotation around the z axis ϕ_z are calculated by solving the following system of equations:

$$\begin{bmatrix}\delta_x\\ \delta_y\\ \phi_z\end{bmatrix} = \mathbf{N}_\mathrm{q}^{-1} \sum_{(i,j)\in A_\mathrm{ST}} \begin{bmatrix} u_x(i,j) \\ u_y(i,j) \\ -u_x(i,j)y(j)+u_y(i,j)x(i)\end{bmatrix}, \tag{3.48}$$

where

$$\mathbf{N}_\mathrm{q} = \sum_{(i,j)\in A_\mathrm{ST}} \begin{bmatrix} 1 & 0 & y(j) \\ 0 & 1 & -x(i) \\ -y(j) & x(i) & -x(i)^2-y(j)^2\end{bmatrix}.$$

4. The conjugate gradient algorithm is started by computing the residuals r and the square sum of these residuals G:

   For the normal problem, the residuals of the CGM are the gaps in the contact area, leading to:

$$r_z(i,j) = h(i,j)+u_z(i,j)-\delta_z-\phi_x y(j)+\phi_y x(i), \tag{3.49}$$

$$G_z = \sum_{(i,j)\in A_\mathrm{C}} r_z(i,j)^2.$$

   For the tangential problem, the residuals are the slips in the stick region, which yields to:

$$\begin{aligned} r_x(i,j) &= u_x(i,j)-\delta_x-\phi_z y(j),\\ r_y(i,j) &= u_y(i,j)-\delta_y+\phi_z x(i), \end{aligned} \tag{3.50}$$

$$G_{xy} = \sum_{(i,j)\in A_\mathrm{ST}} (r_x(i,j)^2+r_y(i,j)^2).$$

5. The descent direction is calculated from the residuals and the previous descent direction:

   Normal problem:

$$\begin{aligned} d_z(i,j) &\leftarrow r_z(i,j)+\xi\frac{G_z}{G_\mathrm{zold}}d_z(i,j), && (i,j)\in A_\mathrm{C}\\ d_z(i,j) &\leftarrow 0, && (i,j)\notin A_\mathrm{C} \end{aligned} \tag{3.51}$$

Tangential problem:

$$
\begin{aligned}
d_x(i,j) &\leftarrow r_x(i,j) + \xi \frac{G_{xy}}{G_{\text{xyold}}} d_x(i,j), \quad && (i,j) \in A_{\text{ST}} \\
d_y(i,j) &\leftarrow r_y(i,j) + \xi \frac{G_{xy}}{G_{\text{xyold}}} d_y(i,j), \quad && (i,j) \in A_{\text{ST}} \\
d_x(i,j) &\leftarrow 0, && (i,j) \in A_{\text{SL}} \\
d_y(i,j) &\leftarrow 0, && (i,j) \in A_{\text{SL}}
\end{aligned} \tag{3.52}
$$

ξ is a variable linked to changes in the contact area. When a point enters or leaves the contact area A_{C} for the normal problem, and when a point enters the slip region for the tangential problem, ξ is set to zero, which resets the conjugate gradient. G is then stored into G_{old} for the next iteration.

6. The DC-FFT is applied to the descent direction and the step to be made in the descent direction α is calculated:

   Normal problem:

$$c_z = K_{zz} \otimes d_z \tag{3.53}$$

$$\alpha_z = \frac{\sum_{(i,j)\in A_{\text{C}}} r_z(i,j) d_z(i,j)}{\sum_{(i,j)\in A_{\text{C}}} c_z(i,j) d_z(i,j)} \tag{3.54}$$

   Tangential problem:

$$c_x = K_{xx} \otimes d_x + K_{xy} \otimes d_y$$

$$c_y = K_{yy} \otimes d_y + K_{yx} \otimes d_x$$

$$\alpha_{xy} = \frac{\sum_{(i,j)\in A_{\text{C}}} r_x(i,j) d_x(i,j) + r_y(i,j) d_y(i,j)}{\sum_{(i,j)\in A_{\text{C}}} c_x(i,j) d_x(i,j) + c_y(i,j) d_y(i,j)} \tag{3.55}$$

7. The pressure and the shears are updated by making a step of length α in the descent direction:

$$p(i,j) \leftarrow p(i,j) - \alpha_z d_z(i,j), (i,j) \in A_{\text{C}} \tag{3.56}$$

$$
\begin{aligned}
q_x(i,j) &\leftarrow q_x(i,j) - \alpha_x d_x(i,j), \quad (i,j) \in A_{\text{ST}} \\
q_y(i,j) &\leftarrow q_y(i,j) - \alpha_y d_y(i,j), \quad (i,j) \in A_{\text{ST}}
\end{aligned} \tag{3.57}
$$

8. Enforcement of the complementarity conditions: the points where the pressure is negative are excluded from the contact area and their pressure is set to zero. The points having a nil pressure and a negative gap will have their pressure

adjusted as follows:

$$p(i,j) = -\alpha h(i,j). \tag{3.58}$$

By doing this adjustment, the point (i,j) will re-enter the contact area, i.e. the active zone, and will be treated in the next iteration.

For the tangential contact problem, the points where the total shear traction $q = \sqrt{q_x^2 + q_y^2}$ is over the product μp are removed from the stick area A_{ST} and are transferred to the slip area A_{SL}. The shear tractions q_x and q_y of those points are adjusted as follows to obey the Coulomb friction law:

$$\begin{aligned} q_x(i,j) &\leftarrow \mu p(i,j)\frac{q_x(i,j)}{\sqrt{q_x(i,j)^2 + q_y(i,j)^2}}, \quad (i,j) \in A_{\mathrm{SL}} \\ q_y(i,j) &\leftarrow \mu p(i,j)\frac{q_y(i,j)}{\sqrt{q_x(i,j)^2 + q_y(i,j)^2}}, \quad (i,j) \in A_{\mathrm{SL}} \end{aligned} \tag{3.59}$$

9. The pressure and the shear tractions are adjusted according to the equilibrium equations using the following form:

$$p(i,j) \leftarrow p(i,j)[a + bx(i) + cy(j)] \tag{3.60}$$

$$\begin{aligned} q_x(i,j) &\leftarrow q_x(i,j) + a_q - c_q y(j) \\ q_y(i,j) &\leftarrow q_y(i,j) + b_q + c_q x(i) \end{aligned} \tag{3.61}$$

$$\begin{bmatrix} a \\ b \\ c \end{bmatrix} = \frac{1}{S}\mathbf{M}^{-1}\begin{bmatrix} N \\ M_y \\ -M_x \end{bmatrix} \tag{3.62}$$

where

$$\mathbf{M} = \sum_{(i,j)\in A_{\mathrm{C}}} p(i,j)\begin{bmatrix} 1 & x(i) & y(j) \\ x(i) & x(i)^2 & x(i)y(j) \\ y(j) & x(i)y(j) & y(j)^2 \end{bmatrix}$$

$$\begin{bmatrix} a_{\mathrm{q}} \\ b_{\mathrm{q}} \\ c_{\mathrm{q}} \end{bmatrix} = \mathbf{M}^{-1}\left(\frac{1}{S}\begin{bmatrix} T_x \\ T_y \\ M_z \end{bmatrix} - \sum_{(i,j)\in A_{\mathrm{C}}}\begin{bmatrix} q_x(i,j) \\ q_y(i,j) \\ yq_x(i,j) + xq_y(i,j) \end{bmatrix}\right) \tag{3.63}$$

where

$$\mathbf{M} = \sum_{(i,j)\in A_{\mathrm{C}}}\begin{bmatrix} 1 & 0 & -y(j) \\ 0 & 1 & x(i) \\ -y(j) & x(i) & x(i)^2 + y(j)^2 \end{bmatrix}$$

The step sequence 2-9 is repeated until the following condition on the residuals is verified:

$$error = \sqrt{G_{\text{old}} S} \leq error_{\text{lim}}. \tag{3.64}$$

The full numerical procedure, summarised in the flow chart Fig. 4.5, has been implemented into MATLAB. The necessary inputs are the material properties of the bodies in contact, their initial separation, and the loading conditions. Simulations can either be force-controlled or displacement-controlled. The outputs are the pressure, shear and slip distributions across the contact area. As will be shown in Chapter 5, it can also be used to extract the normal and tangential contact stiffness.

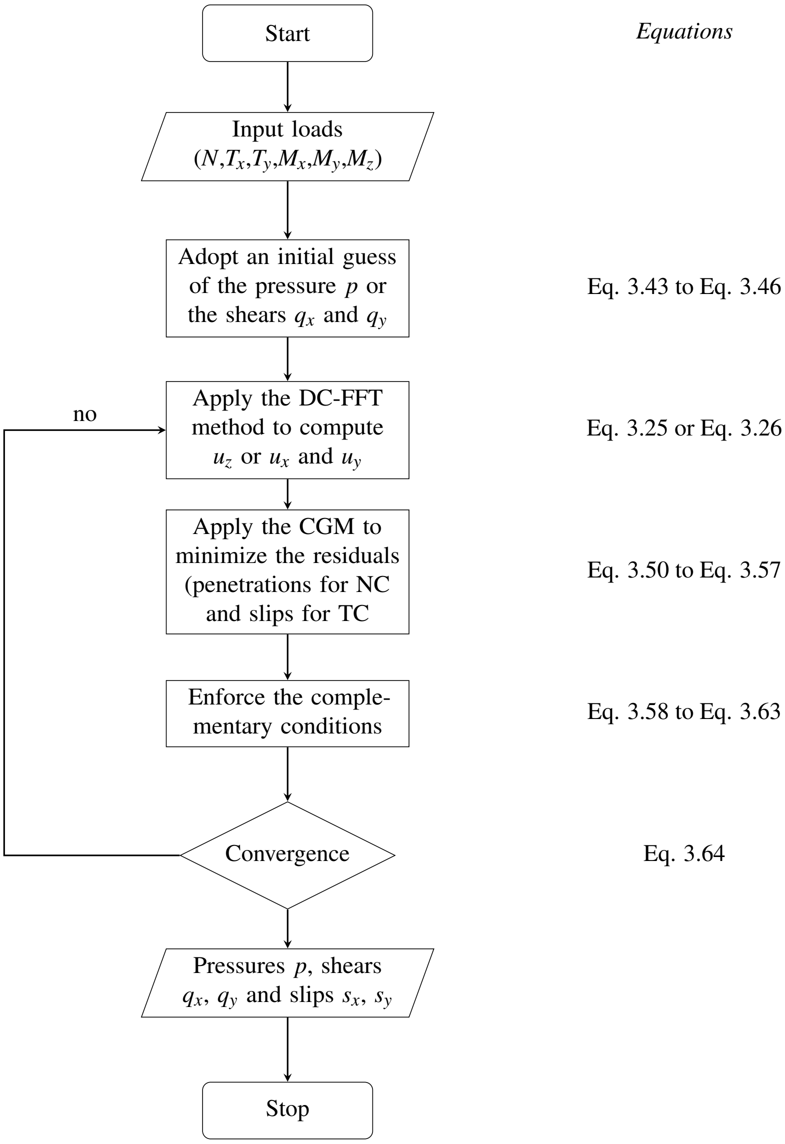

Fig. 3.5 Flow chart of the numerical procedure to solve the normal contact (NC) or the tangential contact (TC) problem

3.4 Verifications against analytical solutions

To verify the implementation of the algorithm described in the previous section and to provide confidence in the results, each of its components has been tested on contact problems for which an analytical solution is available. The first three problems have been used in the past to verify such an algorithm. The present verification also includes an original test case which is more industry relevant and proves the ability of the code to handle bending moments, which makes it the most thorough verification of such a contact algorithm. The verification is done by comparing the pressure and shear distributions obtained from the contact solver against the ones given by the analytical solutions.

3.4.1 Spherical Contact

The first verification problem is based on the smooth contact between two spheres considered as elastic half-spaces, described in Fig. 3.6. The spheres are pressed

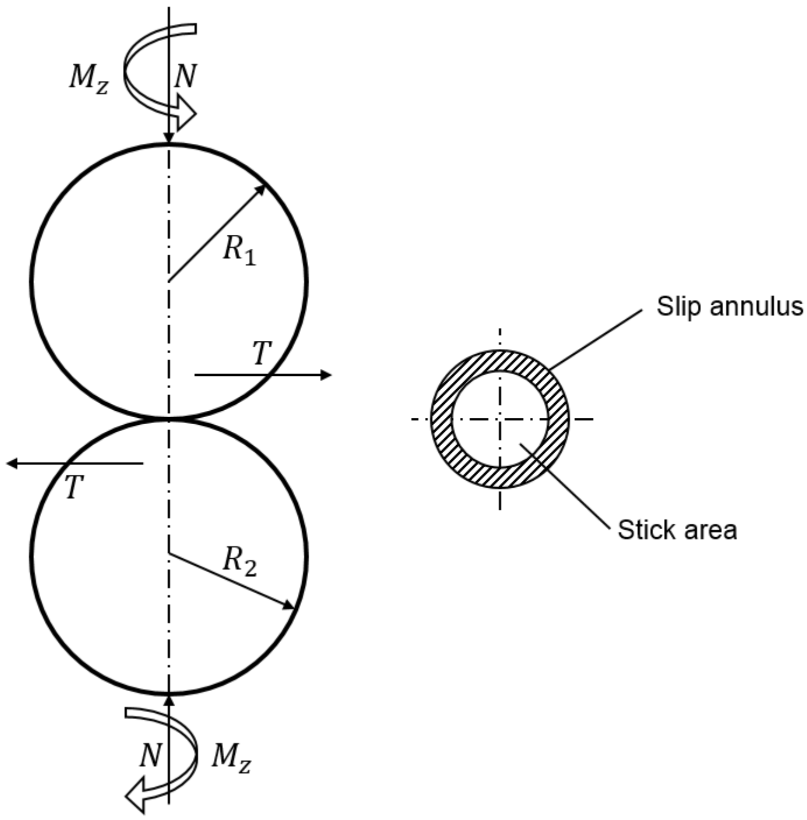

Fig. 3.6 Smooth contact between two spheres

together with a normal load N, and depending on the case under consideration, a tangential load T or a twisting moment M_z is also applied, both of which are chosen to produce partial slip conditions. All calculation parameters are given in Tab. 3.1 . The

Table 3.1 Hertzian contact - calculation parameters

Parameter	Value
Young's modulus of sphere 1, E_1 [GPa]	210
Young's modulus of sphere 2, E_2 [GPa]	210
Poisson ratio of sphere 1, ν_1	0.3
Poisson ratio of sphere 2, ν_2	0.3
Friction coefficient, μ	0.1
Radius of sphere 1, R_1 [m]	0.2
Radius of sphere 2, R_2 [m]	0.2
Normal load, N [N]	1,000
Tangential load, T_x [N]	[0 - 1] * μN
Limit twisting moment, M_{lim} [N.mm]	51.0257
Twisting moment, M_z [N.m]	[0 - 1] * M_{lim}
Maximum Hertzian pressure, p_0 [MPa]	636.3057
Hertzian contact radius, a [mm]	0.8662

results were obtained on a regular grid of 512×512 elements with $-1.5a < x < 1.5a$ and $-1.5a < y < 1.5a$, where a is the radius of the contact area. Figure 3.7 illustrates the 3D pressure and shear distributions that are obtained from the developed contact solver. In what follows, all the comparisons are plotted in a cutting plane ($y = 0$) of those 3D distributions to ease the visualization.

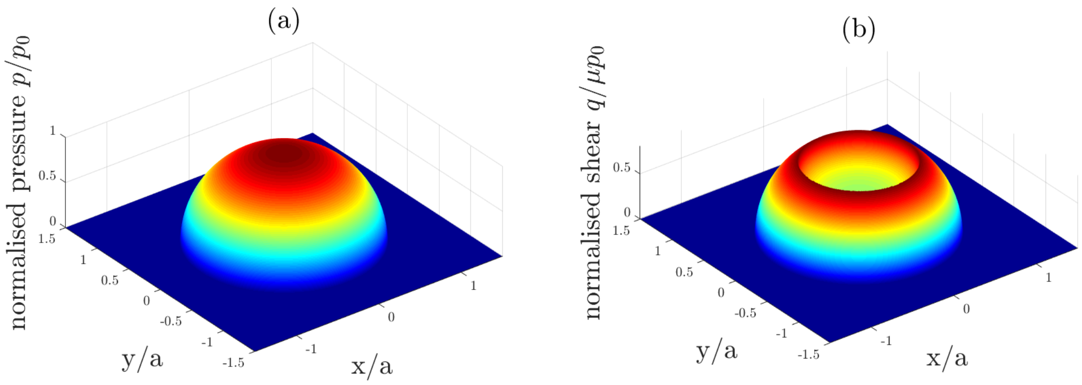

Fig. 3.7 Pressure (a) and shear (b) distributions obtained with the contact solver

Hertzian contact

Hertzian contact refers to the contact under a normal load N between two paraboloidal non-conforming elastic bodies. In the particular case of a contact between two spheres, the results due to Hertz [65] are as follows:

The contact region is a circle whose radius is:

$$a = \left(\frac{3NR}{4E^*}\right)^{1/3}, \tag{3.65}$$

where R is such that $\frac{1}{R} = \frac{1}{R_1} + \frac{1}{R_2}$ and E^* is such that $\frac{1}{E^*} = \frac{1-\nu_1^2}{E_1} + \frac{1-\nu_2^2}{E_2}$. These are respectively the radius and the Young's modulus of the sphere whose contact against a half-plane would lead to the same solution as the contact between the two spheres of radii R_1 and R_2 and Young's modulus E_1 and E_2.
The pressure distribution is given by:

$$p(x,y) = p_0 \left\{1 - \left(\frac{r}{a}\right)^2\right\}^{1/2}, \tag{3.66}$$

where p_0 is the maximum pressure equal to $\frac{3N}{2\pi a^2} = \left(\frac{6NE^{*2}}{\pi^3 R^2}\right)^{1/3}$.
Finally, the depth of indentation, δ_z is given by:

$$\delta_z = \frac{a^2}{R} = \left(\frac{9N^2}{16RE^{*2}}\right)^{1/3}. \tag{3.67}$$

Figure 3.8 compares the pressure distribution p obtained with the contact solver to the Hertzian theory [65] for a centrally applied normal load. The results are normalised by the maximum Hertzian pressure p_0 and the Hertzian contact radius a. The good agreement between the calculated pressure distribution and the analytical solution verifies the implementation of the normal part of the contact solver. Table 3.2 shows

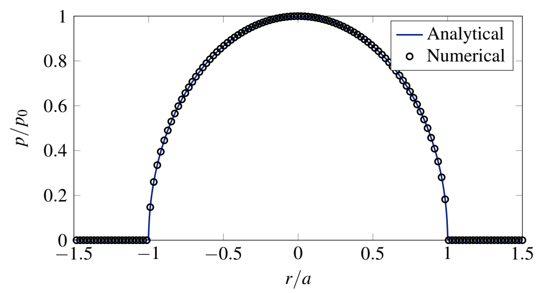

Fig. 3.8 Contact solver pressure distribution (numerical) against the Hertzian theory (analytical)

the CPU times as well as the relative errors on the contact radius a and the maximum contact pressure p_0 between the numerical and the analytical solution for different sizes of the grid. As can be seen, the Hertzian pressure can be reproduced with a high accuracy at a very low computational cost.

Grid size	16×16	32×32	64×64	128×128	256×256	512×512
relative error on a [%]	2.95	1.73	1.07	0.35	0.12	0.06
relative error on p_0 [%]	0.84	0.18	0.05	0.01	0.003	0.0003
CPU time [s]	0.025	0.043	0.072	0.274	1.147	5.441

Table 3.2 Normal contact solution: CPU times and relative errors for different grid sizes

Cattaneo-Mindlin problem

Cattaneo [23] and Mindlin [112] provided the solution to the problem of partial slip when the spherical contact is subjected to a tangential load T limited to μN by the Coulomb friction law. The contact area is now divided into two regions: a stick area and a slip annulus, as depicted in Fig. 3.6. The stick area is a circle of radius c given by:

$$\frac{c}{a} = \left(1 - \frac{T}{\mu N}\right)^{1/3}. \tag{3.68}$$

The shear tractions inside this circle and inside the slip annulus are as follows:

$$\begin{aligned} q(x,y) &= \mu p_0 \left\{1 - \left(\frac{r}{a}\right)^2\right\} - \mu \frac{c}{a} p_0 \left\{1 - \left(\frac{r}{c}\right)^2\right\}, && r \le c \\ q(x,y) &= \mu p_0 \left\{1 - \left(\frac{r}{a}\right)^2\right\}, && c < r \le a \end{aligned} \tag{3.69}$$

where $r = \sqrt{x^2+y^2}$.
The rigid body displacement in the tangential direction is:

$$\delta_x = \frac{3\mu N}{16a}\left(\frac{2-\nu_1}{G_1} + \frac{2-\nu_2}{G_2}\right)\left\{1 - \left(1 - \frac{T}{\mu N}\right)^{2/3}\right\}, \tag{3.70}$$

where G_1 and G_2 are the shear moduli of the contacting spheres.
The magnitude of the slips occurring in the slip annulus is expressed by:

$$\begin{aligned} s_x = \frac{3\mu N}{32Ga^3} r^2 \Bigg[& 2(2-\nu)\left\{\left(1 - \frac{2}{\pi}\arcsin\frac{c}{r}\right)\left(1 - 2\frac{c^2}{r^2}\right) + \frac{2c}{\pi r}\sqrt{1 - \frac{c^2}{r^2}}\right\} \\ & -\nu \left\{\left(1 - \frac{2}{\pi}\arcsin\frac{c}{r}\right) + \left(1 - 2\frac{c^2}{r^2}\right)\frac{2c}{\pi r}\sqrt{1 - \frac{c^2}{r^2}}\right\}\cos 2\theta \Bigg] \end{aligned}, \tag{3.71}$$

where $\theta = (\widehat{x,y})$.
Figures 3.9 and 3.10 display respectively the shear and the slip distributions for different values of the dimensionless tangential load $\bar{T}_x = \frac{T_x}{\mu N}$. The present results show a good agreement with the analytical solution. They also prove the ability of the implemented solver to handle partial slip contact: while a central circular part of the

contact is fully stuck, a slip annulus can be observed near the edges of the contact area, in which the shear equals its Coulomb limit μp.

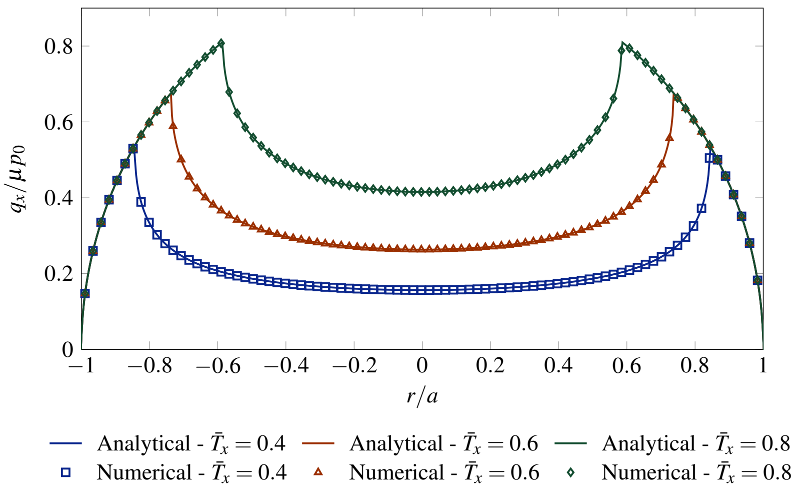

Fig. 3.9 Contact solver shear distribution (numerical) against Cattaneo-Mindlin theory (analytical)

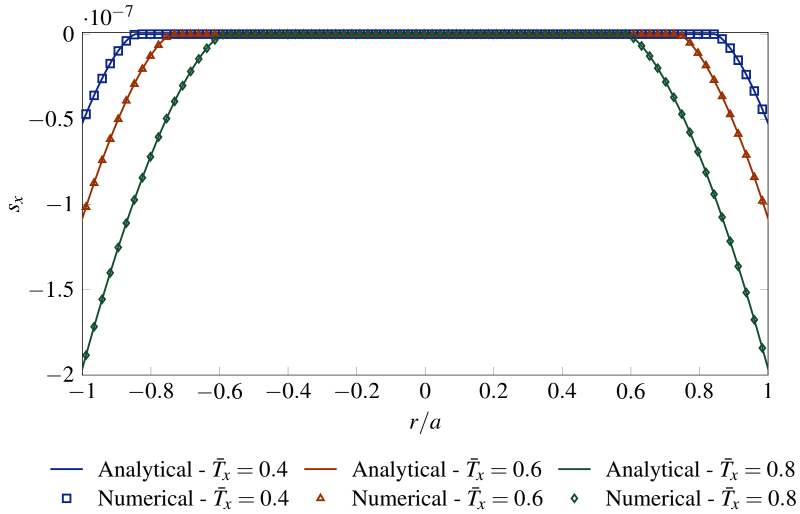

Fig. 3.10 Contact solver slip distribution (numerical) against Cattaneo-Mindlin theory (analytical)

Based on the previous expressions, Johnson [77] provided the solution of the same circular contact subjected to a tangential load oscillating between $-Q_*$ and Q_*, therefore undergoing the fretting loop shown in Fig. 3.11. Between the points O and A, the shear tractions are given by Eq. 3.69. Between A and C, i.e. during the unloading

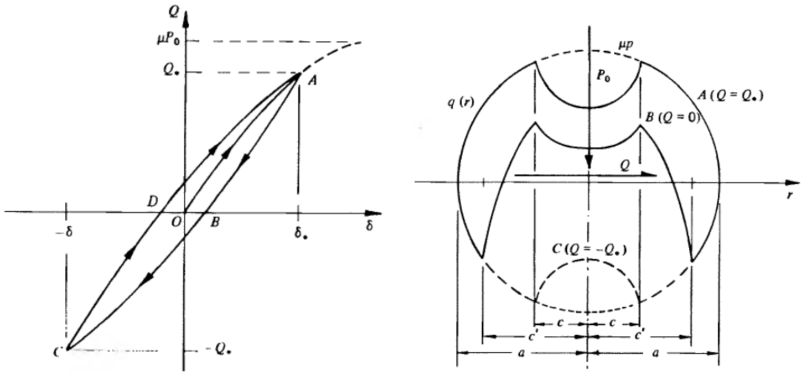

Fig. 3.11 Fretting loop (left) and resulting shear tractions (right) [77]

phase, the shear tractions are:

$$
\begin{aligned}
q(x,y) &= -\frac{3\mu p_0}{2\pi a^3}\left\{\left(a^2-r^2\right)^{1/2}-2\left(c'^2-r^2\right)^{1/2}+\left(c^2-r^2\right)^{1/2}\right\}, && r\leq c\\
q(x,y) &= -\frac{3\mu p_0}{2\pi a^3}\left\{\left(a^2-r^2\right)^{1/2}-2\left(c'^2-r^2\right)^{1/2}\right\}, && c\leq r\leq c'\\
q(x,y) &= -\frac{3\mu p_0}{2\pi a^3}\left(a^2-r^2\right)^{1/2}, && c'\leq r\leq a
\end{aligned}
\tag{3.72}
$$

where c' defines the new extent of the slip annulus and whose value can be extracted from the following equation:

$$
\frac{c'^3}{a^3}=\frac{1}{2}\left(1+\frac{c^3}{a^3}\right). \tag{3.73}
$$

The rigid body displacement is now equal to:

$$
\delta_x=\frac{3\mu N}{16a}\left(\frac{2-\nu_1}{G_1}+\frac{2-\nu_2}{G_2}\right)\left\{2\left(1-\frac{Q_*-Q}{2\mu p_0}\right)^{2/3}-\left(1-\frac{Q_*}{\mu p_0}\right)^{2/3}-1\right\}. \tag{3.74}
$$

The applied fretting loadings are shown in Fig. 3.12: the normal load is kept constant while the tangential load oscillates between $-0.8\mu N$ and $0.8\mu N$. Figure 3.13 displays the shear tractions corresponding to different points of these fretting loadings. Figure 3.14 shows the load-displacement curve for the cycle A-B-C-D and proves the capacity of the implemented contact solver to estimate the fretting hysteresis loop. Table

Grid size	16×16	32×32	64×64	128×128	256×256	512×512
relative error on c [%]	3.534	2.571	1.866	0.456	0.275	0.131
relative error on $q(r=0)$ [%]	1.533	0.440	0.058	0.018	0.007	0.0004
CPU time [s] for 1 load increment	0.066	0.059	0.205	0.763	3.609	17.066
CPU time [s] for 1 fretting cycle	0.370	1.007	4.307	21.161	133.231	839.206

Table 3.3 Tangential contact solution: CPU times and relative errors for different grid sizes

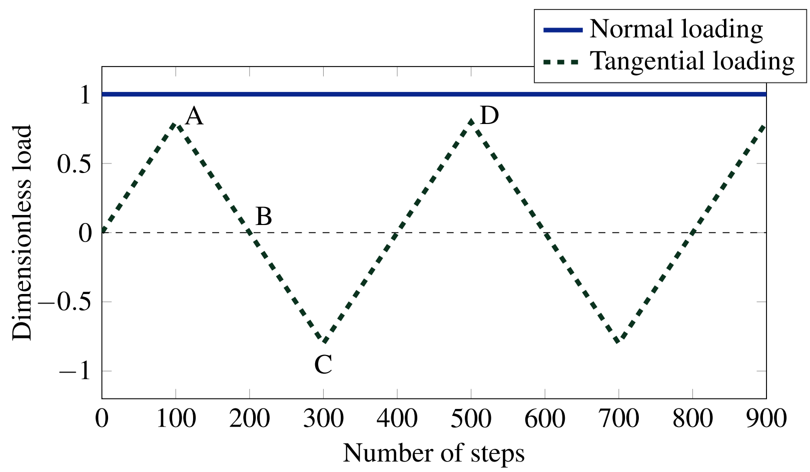

Fig. 3.12 Fretting loading

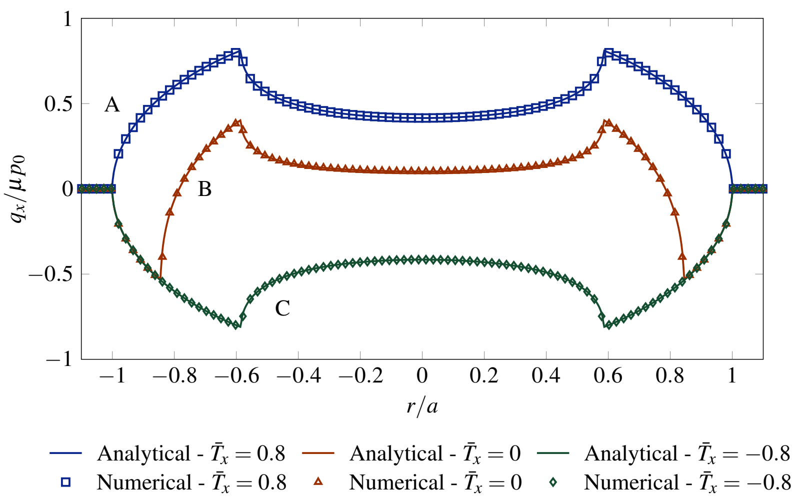

Fig. 3.13 Contact solver shear distribution (numerical) against Cattaneo-Mindlin theory (analytical) for an oscillating tangential force

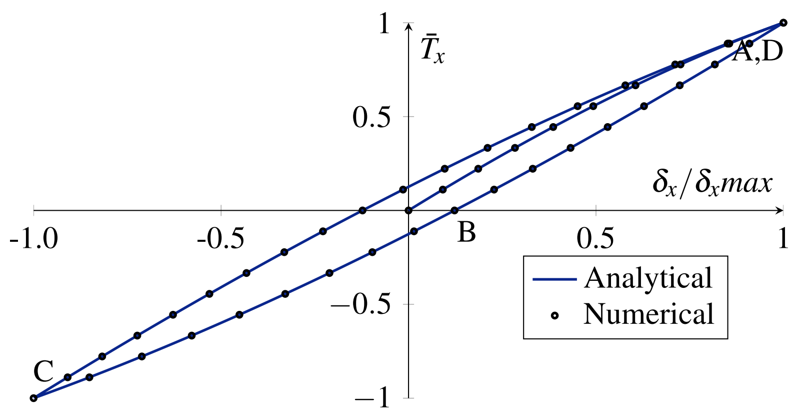

Fig. 3.14 Load-displacement cycle: Contact solver (numerical) against Cattaneo-Mindlin theory (analytical)

3.3 shows the CPU times as well as the relative errors on the radius of the stick area c and the shear stress at the centre of the contact area between the numerical and the analytical solution for different sizes of the grid. The CPU time for 1 fretting cycle corresponds to 36 load increments, used to obtain the fretting loop shown in Fig. 3.14. From these data, it can be observed that a compromise between accuracy and computational speed is highly desirable if it is intended to simulate many fretting cycles with a reasonable computational effort. In this particular case, a grid size of 128×128 would be a good compromise since it leads to less than 1% error while keeping a CPU time 20 times smaller than the 512×512 grid.

Lubkin problem

The solution to the contact problem where the two spheres are pressed together and then subjected to a torsional couple M_z was derived by Lubkin [100]. Similar to the Cattaneo & Mindlin problem, the contact area, under partial slip condition, comprises a stick circular region and a slip annulus. In order to remain under partial slip condition, the applied torque has to be smaller than the following limiting value:

$$M_{\lim} = \frac{3\pi}{16}\mu N a. \tag{3.75}$$

The extent of the stick area, c, is linked to the parameter k (or its trigonometric complement $k' = \sqrt{1-k^2}$) via the following equation:

$$k = \left(1 - \frac{c^2}{a^2}\right)^{1/2}. \tag{3.76}$$

The parameter k is related to the applied dimensionless torque $T = \frac{M}{\mu N a}$ via:

$$\begin{aligned} T(k) = \frac{1}{4\pi}\Bigg\{ & \frac{3\pi^2}{4} + k'k\left[6K(k) + \left(4k'^2 - 3\right)D(k)\right] - 3kK(k)\arcsin(k') \\ & -3k^2\left[K(k)\int_0^{\pi/2}\frac{\arcsin(k' sin(\alpha))d\alpha}{(1-k'^2 sin(\alpha)^2)^{3/2}} - D(k)\int_0^{\pi/2}\frac{\arcsin(k' sin(\alpha))d\alpha}{(1-k'^2 sin(\alpha)^2)^{1/2}}\right]\Bigg\}, \end{aligned} \tag{3.77}$$

with

$$D(k) = \frac{K(k) - E(k)}{k^2}, \tag{3.78}$$

where K and E are the complete elliptic integrals of the first and second kind (see Appendix A).

In a cylindrical coordinate system, the shear tractions are given by:

$$\begin{aligned} q_\theta &= \frac{3\mu N}{2\pi a^2}\left(1-\frac{r^2}{a^2}\right)^{1/2}, && c < r \leq a \\ q_\theta &= \frac{3\mu N}{(\pi a)^2}\left(1-\frac{r^2}{a^2}\right)^{1/2}\left[\frac{\pi}{2}+k^2\mathbf{D}(k)\mathbf{F}(k',\varphi)-\mathbf{K}(k)\mathbf{E}(k',\varphi)\right], && r \leq c \end{aligned}, \tag{3.79}$$

where $F(k',\varphi)$ and $E(k',\varphi)$ are the elliptic integrals of first and second kind (see Appendix A) and

$$\varphi = \arcsin\frac{1}{k'}\sqrt{\frac{k'^2-(r/a)^2}{1-(r/a)^2}}. \tag{3.80}$$

Lubkin also derived the following equation for the dimensionless relative twist angle:

$$\theta = \frac{3}{4\pi}k^2 D(k), \tag{3.81}$$

where $\theta = \frac{\beta G a^2}{\mu N}$ and G is the shear modulus.
Instead of using the full solution for the torque versus angle given by Eq. 3.77, which is very challenging to invert, the following approximation, proposed by Segalman [170], was used:

$$T_p(\theta) = \frac{a_0+a_1\theta+a_2\theta^2+a_3\theta^3+a_4\theta^4}{b_0+b_1\theta+b_2\theta^2+b_3\theta^3+b_4\theta^4}, \tag{3.82}$$

where

$$\begin{array}{lllll} a_0 = 0 & a_1 = 16/3 & a_2 = 6.0327 & a_3 = 19.6951 & a_4 = 42.5359 \\ b_0 = 1 & b_1 = 5.1193 & b_2 = 15.6833 & b_3 = 30.8099 & b_4 = 72.2111. \end{array}$$

From an applied torque T, the twist angle θ can be determined using Eq. 3.82. Then, the parameter k can be calculated using Eq. 3.81. Once k is known, the values of k', c, φ can be obtained and finally the shear fields can be computed. Figure 3.15 compares the results obtained from the contact solver and the analytical solution for different values of the applied torque. This particular test case demonstrates that the contact solver correctly accounts for the coupling between the two tangential directions.

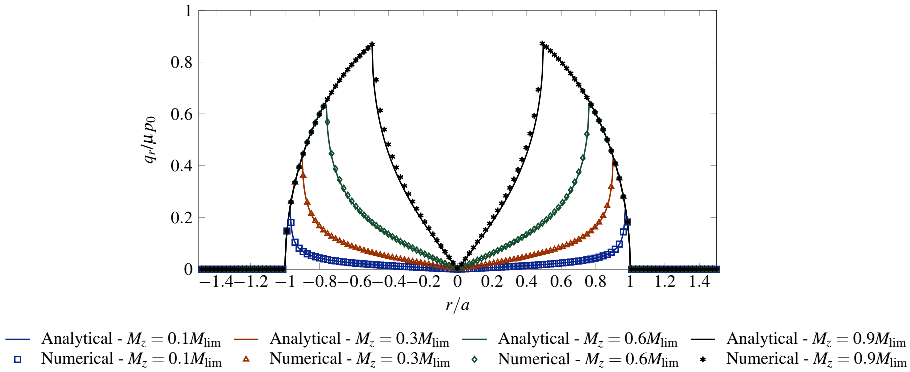

Fig. 3.15 Computed shear distribution (numerical) against Lubkin's theory (analytical)

3.4.2 Inclined Punch With Rounded Edges

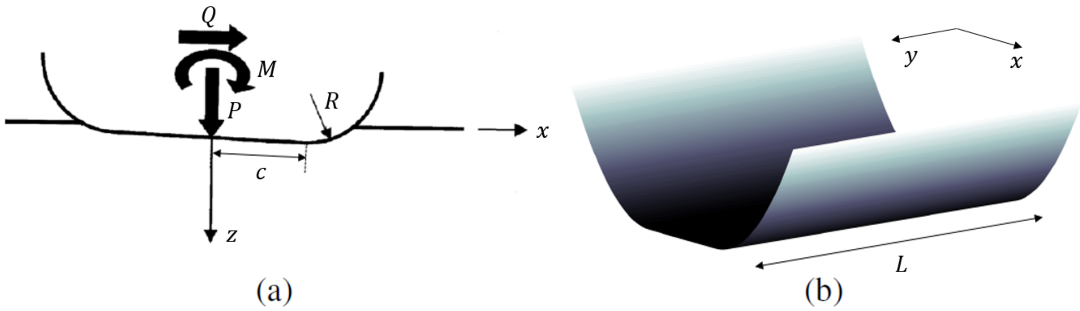

Fig. 3.16 Contact geometry used in Goryacheva [60] (a) and in the contact solver (b)

To complete the verification of the implemented contact solver, an additional test case, based on the contact between an inclined punch with rounded edges and a flat elastic half-plane, was applied for the first time to verify a semi-analytical contact solver. This particular test case verifies the handling of the two bending moments M_x and M_y. The analytical solution of this contact problem was established by Goryacheva [60]. Unlike the previous analytical solutions, this one cannot be summarised in a few equations. Therefore, its description is omitted here for brevity and the reader is invited to refer to the original paper [60] for further details.

It is worth noting that this analytical solution is given for the two-dimensional contact problem. To allow the comparison with the contact solver, which is three-dimensional, the punch has been extended in the out-of-plane direction so that its length is much larger than its width, as shown in Fig. 3.16. The results are compared at mid-length of the punch to reduce the boundary effects. To better understand the impact of these boundary effects, Fig. 3.17 shows the pressure distribution under normal loading for different ratios between the width (2c) and the length (L) of the punch. For large values of the ratio $L/2c$, the pressure distribution at $y = 0$ (mid-length of the punch) obtained with the contact solver becomes similar to that calculated by Goryacheva on the 2D

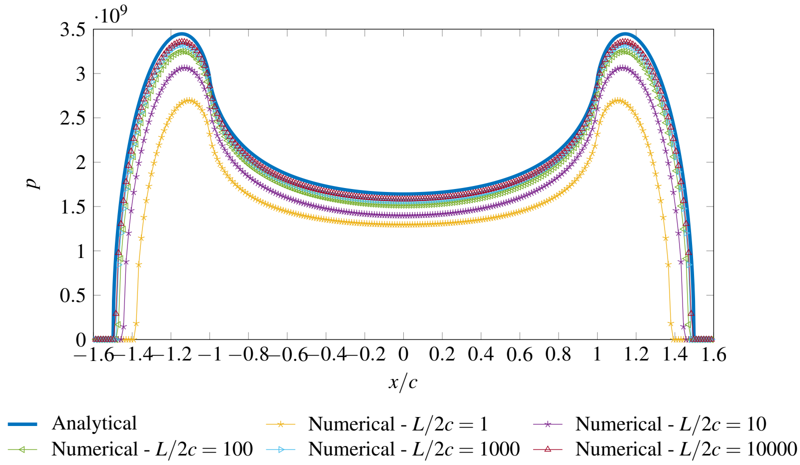

Fig. 3.17 Pressure distribution under normal load: contact solver results (numerical) for different ratios $L/2c$ against Goryacheva theory (analytical)

Table 3.4 Inclined punch contact - calculation parameters

Parameter	Value
Young's modulus E [GPa]	210
Poisson ratio, ν	0.3
Friction coefficient, μ	0.1
Width of the punch base $2c$ [m]	3.0
Radius of curvature R [m] at $\pm c$	10.0
Length of the punch L [m]	30,000
Normal load, N [N]	1.29e11
Tangential load, T_x [N]	[0 - 1] * μN
Bending moment, M_y [N]	[0 - 1] * 9e10

contact problem. This proves the relevance of the proposed comparison and highlights that the 2D hypothesis is a very strong assumption for the analysis of real contact problems. The pressure distributions of the punch in Fig. 3.18 were obtained under a constant normal load N and for different bending moments around the y direction M_y. The values of these loads as well as the other calculation parameters are given in Tab. 3.4. Figure 3.19 displays the shear tractions under a constant normal load and bending moment, and for different values of the normalised tangential force $\bar{T}_x = \dfrac{2T_xR}{\mu E^* c^2}$. The good agreement between the solver results and those obtained from Goryacheva's analytical solution verifies the capacity of the solver to handle the bending moment M_y. The same procedure has been applied for the bending moment M_x, leading to the same good agreement.

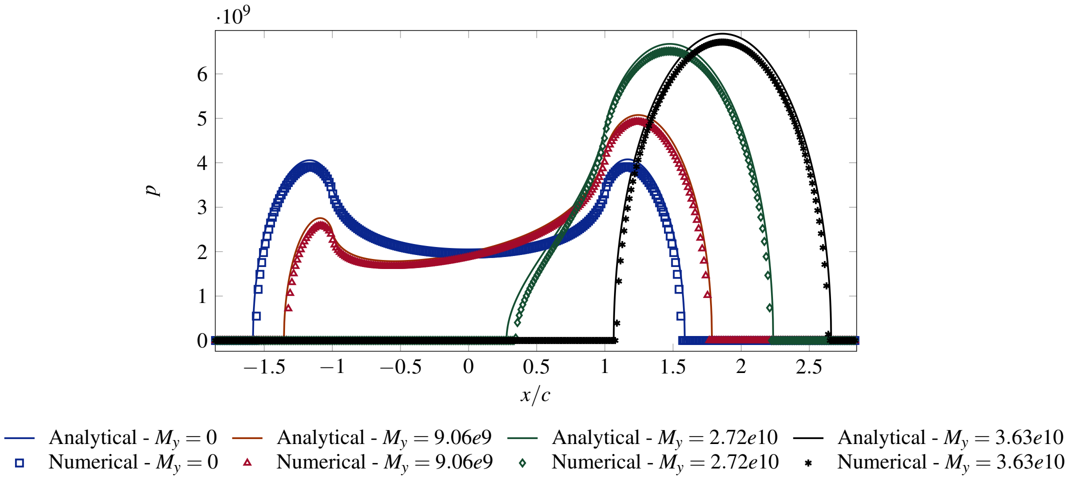

Fig. 3.18 Pressure distribution under varying bending moment M_y : contact solver results (numerical) against Goryacheva theory (analytical)

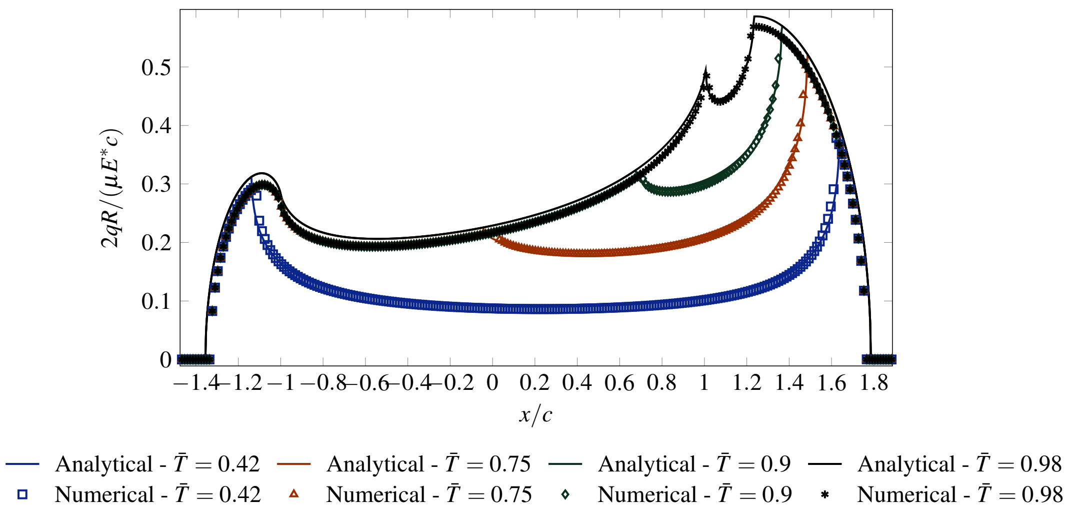

Fig. 3.19 Shear distribution under constant bending moment M_y and varying tangential load T_x : contact solver results (numerical) against Goryacheva theory (analytical)

3.5 Impact of the elastic half-space assumption

The correct computation of the contact stresses and stick-slip transitions for industrial applications is of highest relevance, since they will influence the contact conditions at the interface and influence potential energy dissipation in a vibration environment, the sealing capabilities of the contact interface, wear behaviour, and in the worst case the integrity of the connection. Therefore, an evaluation of the accuracy of the proposed framework is necessary to understand the impact of the half-space assumption on the results. To better understand this impact, and provide some guidelines for the use of the implemented contact solver for a practical application, three different test cases have been studied: the contact between two similarly elastic spheres, the contact between a rigid ball and an elastic plate, and the contact between a rigid punch with rounded edges and an elastic plate. The three contact problems have been modelled with great detail using the Finite Element software Abaqus and the computed results were compared to those obtained with the contact solver to investigate the impact of the half-space assumption on the computed pressure distribution. The computational benefits of the solver over the Finite Element Method are also demonstrated.

3.5.1 Elastic Spherical Contact

In order to capture the pressure distribution accurately, the mesh size is particularly small in the region enclosing the contact area. Mesh convergence analysis was conducted to ensure the contact solver results were compared to the converged FE solutions. The FE mesh is described in detail for the first test case, with similar meshes being used for the others two cases. To avoid FE convergence issues inherent to the non-conforming nature of the spherical contact, all FE simulations were displacement-controlled. The contact solver analysis can either be load-controlled or displacement-controlled, so a direct comparison with the FE results is possible. The Augmented Lagrange approach and a direct solver are used to solve the normal contact problem in Abaqus/Standard. In addition, the contact is assumed to be frictionless. The pressure distributions obtained from FEM and the contact solver are compared based on the relative error on the maximum contact pressure which is defined as follows:

$$relative\ error\ (\%) = 100 * \frac{\left|P_{\text{Abaqus}} - P_{\text{Solver}}\right|}{P_{\text{Abaqus}}}.$$

A similar approach has been used for the two other test cases. The associated FE meshes are not presented for brevity. The mesh depicted in Fig. 3.20, identical for both spheres, is composed of approximately 83,000 8-node hex elements and 88,000 nodes. The mesh size is particularly small in the region enclosing the contact area, where the radial spacing of the elements is approximately 1 mm (the hemisphere radius is 200 mm and each element spans 7.5° circumferentially, leading to approximately 2,500 elements. A vertical displacement is applied on the top surface of one sphere, while the bottom surface of the other is fixed. The material properties are the same as those given in Tab. 3.1.

Figure 3.21 shows that the bigger the ratio R/a, the closer the contact solver results are to the FE results. This is consistent with the half-space definition; the smaller the contact area compared to the dimensions of the contacting bodies, the closer we get to the half-space assumption.

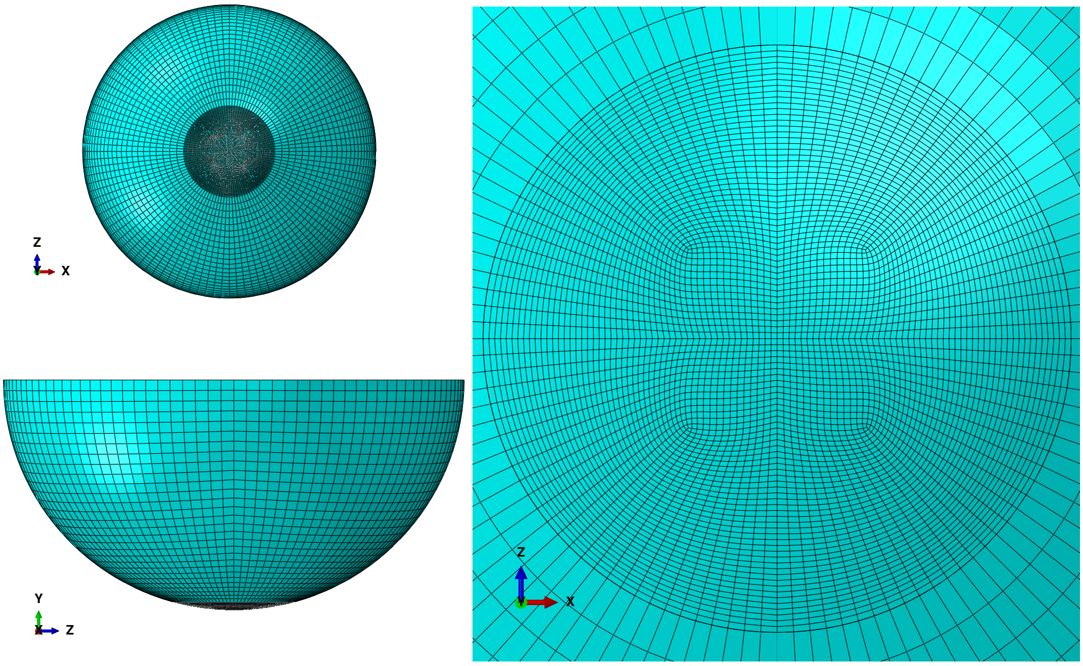

Fig. 3.20 Finite element mesh of sphere 1

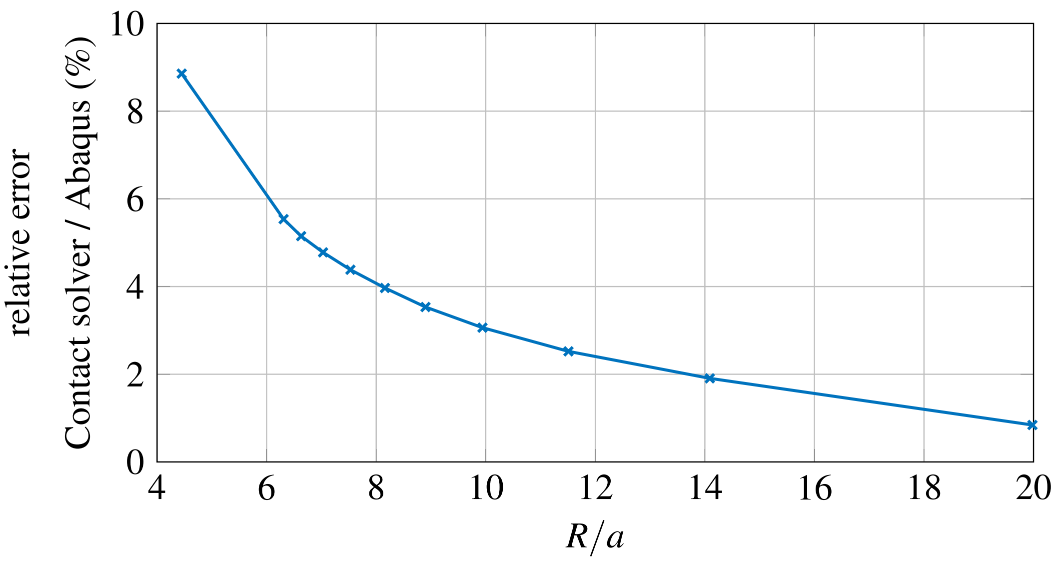

Fig. 3.21 Error on maximum pressure value between the contact solver and Abaqus for different R/a ratios

3.5.2 Rigid Ball on Elastic Plate Contact

The second contact geometry, depicted in Fig. 3.22, consists of a rigid ball on an elastic flat plane of thickness t, width w and length L. The dimensions and material properties of the contacting bodies are summarised in Tab. 3.5. A vertical displacement is applied on the rigid ball, while the bottom and side faces of the plate are fixed. The radius of the ball and the imposed displacement were kept constant, while the dimensions of the plate were varied to evaluate the influence of the half-space assumption. Figure 3.23

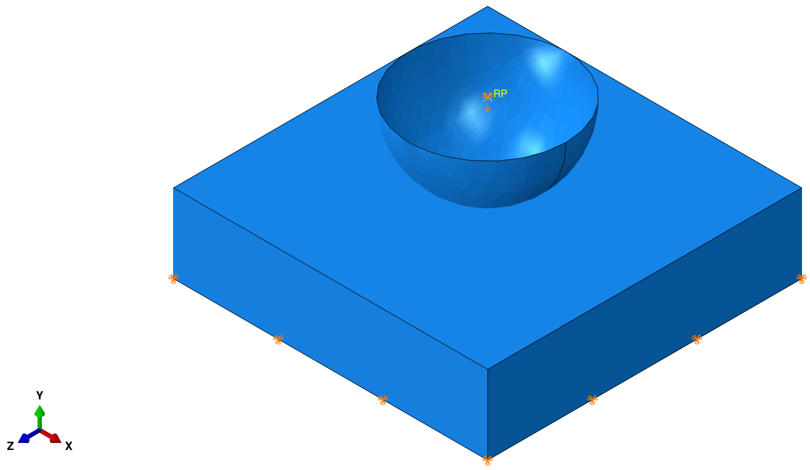

Fig. 3.22 Ball-on-plate contact geometry

Table 3.5 Ball-on-plate contact - calculation parameters

Parameter	Value
Plate thickness, t [mm]	[5 - 50]
Plate width, w [mm]	[10 - 50]
Plate length, L [mm]	[10 - 50]
Young's modulus of the plate, E [GPa]	210
Poisson ratio of the plate, ν	0.3
Radius of the ball, R [mm]	10.0
Imposed normal displacement, u_z [mm]	1.0
Maximum Hertzian pressure, p_0 [GPa]	46.4577
Hertzian contact radius, a [mm]	3.16

shows the relative error between the contact solver and Abaqus for different values of the ratio between the thickness of the plate t and the radius of the contact area a; the width w and length L of the plate were kept constant such that $w/a = L/a = 15.81$. It can be seen that for high values of the ratio t/a, the error between the contact solver and FEM reduces and tends to zero. A similar behaviour is obtained when the ratio w/a is changed, as illustrated by Fig. 3.24. These results were obtained for a fixed ratio $t/a = 3.16$. This time, it can be observed that the error does not tend to 0% but 10%, which is due to the chosen ratio $t/a = 3.16$ (see Fig. 3.23).

Assuming that the influence of the thickness of the plate is uncoupled from the influence of the width/length of the plate (this assumption has been confirmed on several combinations of t/a and w/a), the errors due to the ratios t/a and $w,L/a$ can be linearly combined to obtain the error iso-lines presented in Fig. 3.25. These iso-lines allow a quick estimation of the error resulting from the use of the half-space assumption to solve a contact problem for different values of the dimensionless ratios

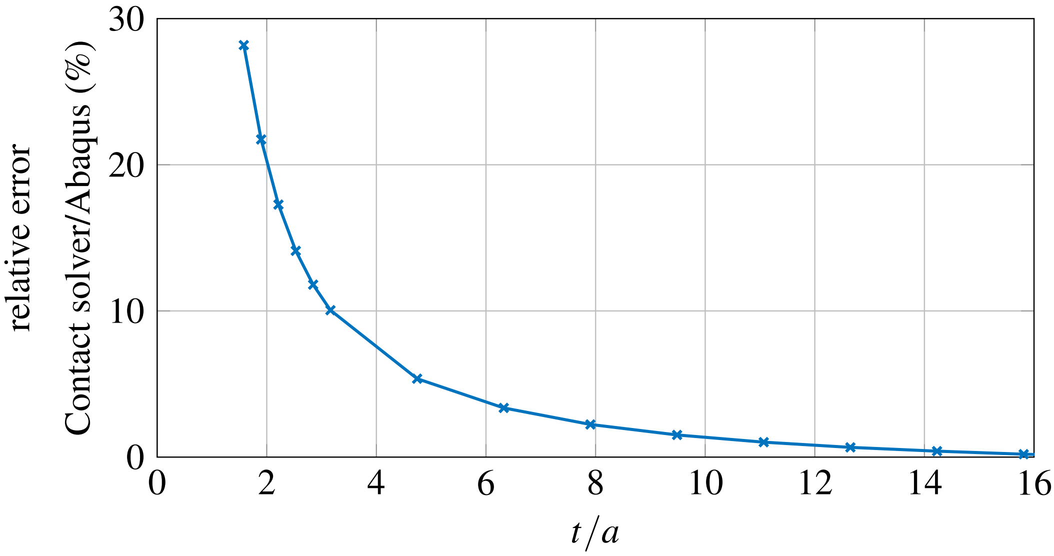

Fig. 3.23 Error on pressure distribution between the contact solver and FEM for different t/a

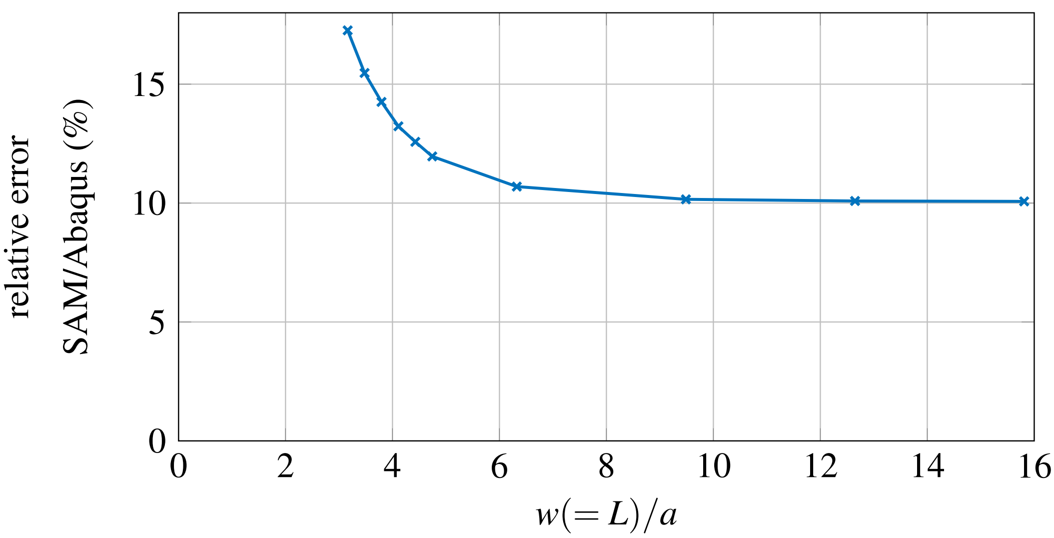

Fig. 3.24 Error on pressure distribution between the contact solver and Abaqus for different $w(=L)/a$ ratios

t/a and $w,L/a$ and as such are a useful tool to estimate the accuracy of the contact solver results for engineering contacts.

3.5.3 Rigid Punch With Rounded Edges on Elastic Plate Contact

The same analysis has been conducted for the contact between a rigid punch with rounded edges and an elastic plate, Fig. 3.26, which is much more representative of a real industrial contact problem. The considered dimensionless ratios are t/c where t is the thickness of the plate and c the radius of the flat base of the punch, and $w,L/c$

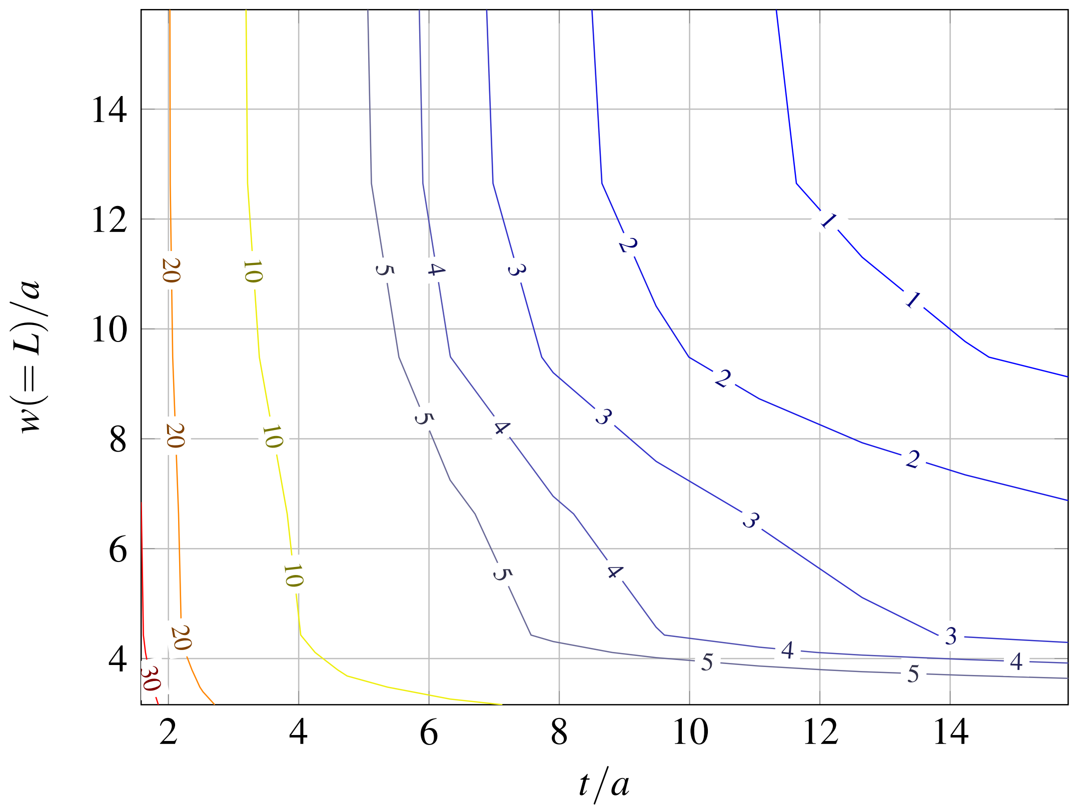

Fig. 3.25 Ball-on-plate contact - Isolines of relative error (%)

where w and L are the width and the length of the plate, respectively. The calculation parameters are given in Tab. 3.6. Once more, the plate was fixed at its bottom and

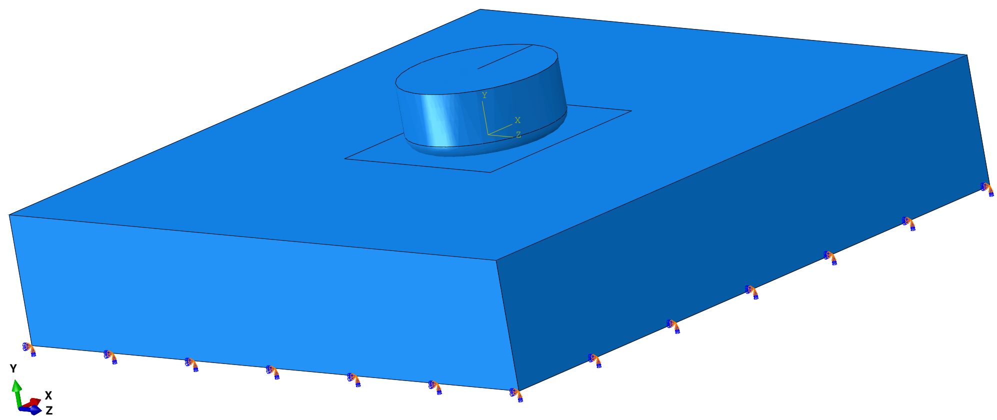

Fig. 3.26 Punch-on-plate contact geometry

side faces, and its thickness, width and length were varied while the dimensions of the punch were kept constant. Figure 3.27 shows the computed relative error when changing the ratio t/c. Similar to the previous test case, the relative error between the contact solver and Abaqus reduces when increasing the ratio t/c. It can be shown

Table 3.6 Punch-on-plate contact - calculation parameters

Parameter	Value
Plate thickness, t [mm]	[10 - 80]
Plate width, w [mm]	[20 - 90]
Plate length, L [mm]	[20 - 90]
Young's modulus of the plate, E [GPa]	210
Poisson ratio of the plate, ν	0.3
Width of the punch base, $2c$ [mm]	100
Radius of curvature R [mm] at $\pm c$	10.0
Imposed normal displacement, u_z [mm]	1.0

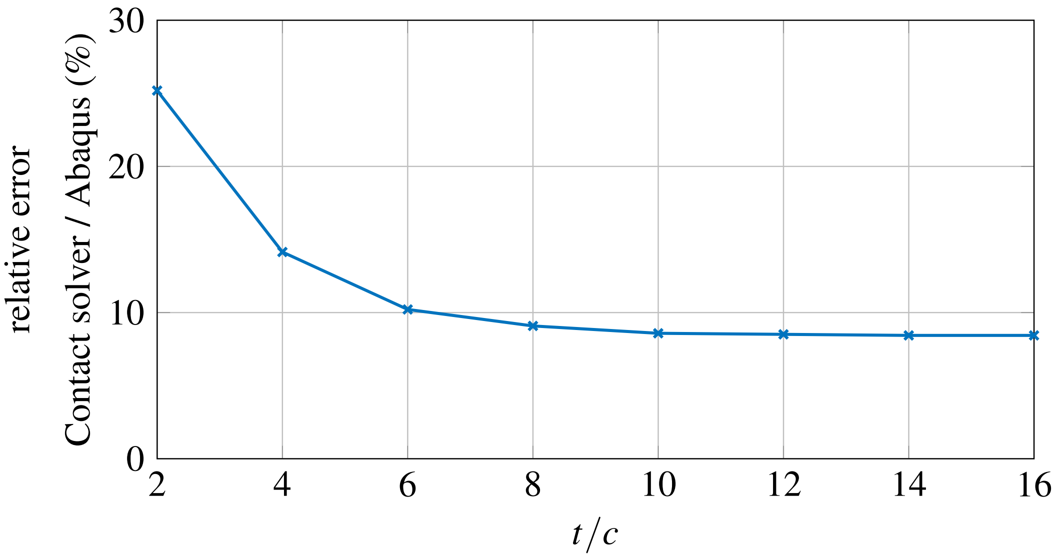

Fig. 3.27 Error on pressure distribution between the contact solver and Abaqus for different t/c ratios

that the remaining error of approximately 8% is due to the influence of the chosen length and width parameters. The same behaviour is observed when changing the ratio $w(=L)/c$ as illustrated by Fig. 3.28. The resulting iso-lines of error are shown in Fig. 3.29.

All three presented test cases show the same result: the bigger the contacting bodies are compared to the contact area, the better the half-space assumption, and the more accurate the computed results with the contact solver. The presented results, and in particular the isolines, give a quantitative estimation of the impact of using the half-space assumption. For all tested dimensions, the induced error on the maximum pressure ranges from nearly 0% to 30%. This error has to be evaluated for engineering joints such as flange joints and this can be done using the presented iso-lines. This loss of accuracy of the contact solver should, however, be set against the huge computational benefits of the method compared to FE simulations as demonstrated in Tab. 3.7 which

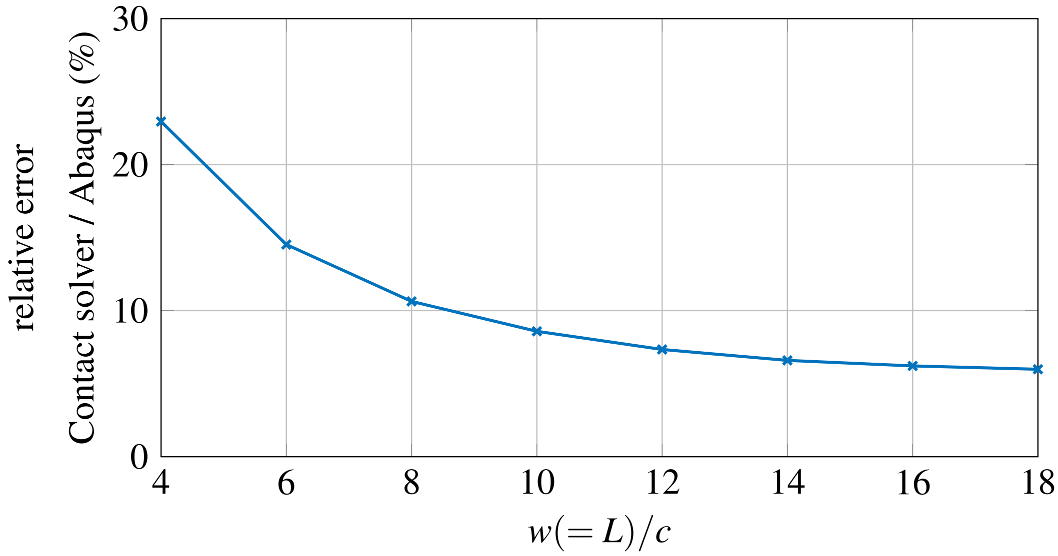

Fig. 3.28 Error on pressure distribution between the contact solver and Abaqus for different $w(=L)/c$ ratios

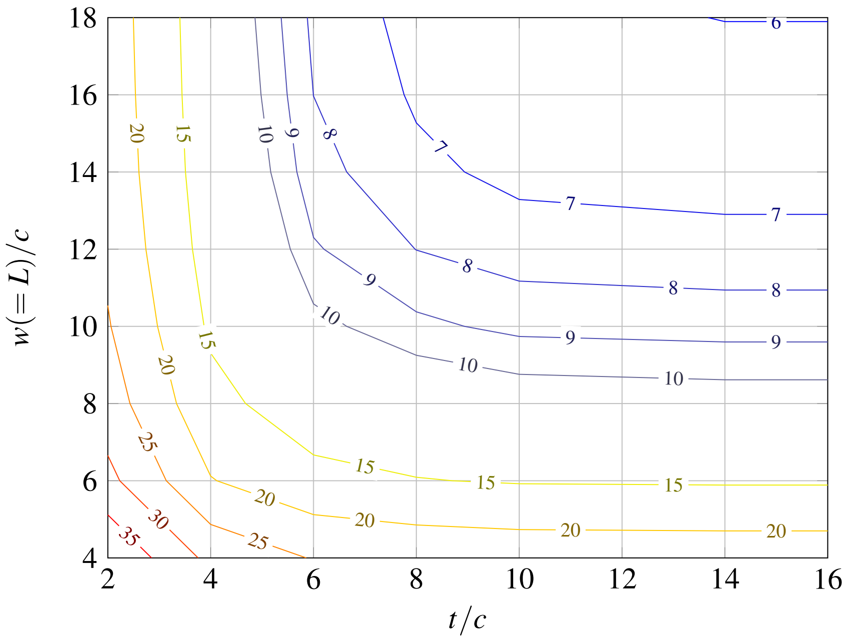

Fig. 3.29 Punch-on-plate contact - Isolines of relative error (%)

shows the memory usage and CPU times of the contact solver and Abaqus for the three test cases (the computations have been performed using an Intel Core i7 Processor); the contact solver is shown to be a hundred times faster than the FEM to solve the considered contact problems. Furthermore, when used within a multi-scale approach as proposed in [51], where the contact analysis is performed at a micro-scale, the contact solver results will show less sensitivity to the boundary conditions applied to the overall body. Additionally, taking into account the roughness of the material should further reduce the impact of the half-space assumption.

Table 3.7 FEM computational time compared to the contact solver's

		Method	
		FEM	Contact solver
Sphere-on-Sphere	Memory usage	8.1 GB	689 MB
	CPU time [s]	1385	4.83
Ball-on-Plate	Memory usage	9.3 GB	688 MB
	CPU time [s]	781	13.85
Punch-on-Plate	Memory usage	12.3GB	630 MB
	CPU time [s]	665	9.56

3.6 Conclusions

In this chapter, the underlying theory and the key components of the implemented contact solver have been presented. The main advantage of this solver is its low computational cost stemming from the fact that only the boundaries of the contacting bodies, i.e. the contact surfaces, are analysed. These computational benefits were demonstrated based on comparisons against Finite Element simulations for three different test cases. These comparisons also allowed to illustrate and estimate the loss of accuracy resulting from the use of the elastic half-space description, which is one of the underlying assumptions of the implemented contact solver.

The results obtained from the implemented contact solver for a wide range of test cases have been compared and verified against available analytical solutions. It was shown that the implemented contact solver is able to handle the six possible loads (normal, two tangential, two bending moments and twisting moment) correctly, and the presented approach can therefore be considered as fully verified. Furthermore, the calculated pressure and slip distributions make it possible to couple the contact solver with Archard's law [6] to calculate wear. The computed load-displacement cycle also makes it possible to use the energy wear approach [46] for wear computation, as will be shown in the next chapter.

Chapter 4

Multiscale approach for fretting wear analysis applied to smooth contact interface

4.1 Introduction

In this fourth chapter, a multiscale approach is proposed in order to model and account for fretting wear in a nonlinear dynamic analysis. A detailed description of the approach is provided in the first section of the chapter. The following three sections will illustrate how the approach works and its potential on an underplatform damper system test case. In the last section of the chapter, the results and their implications from a turbomachinery design perspective will be discussed.

4.2 Description of the approach

As discussed at great length in the literature review chapter, fretting wear is a complex multiscale problem and therefore a multiscale approach seemed natural to tackle this problem. In the proposed multiscale approach, two separate space scales are considered: a macro-scale for the dynamic analysis and a meso-scale for the contact analysis and wear computation, which allows a better discretisation of the contact area and hence a higher accuracy. Two separate time scales are also considered: a fast scale for the dynamic analysis and a slow scale for tribological phenomena. The proposed multiscale approach, that allows the prediction of fretting wear as well as its effects on the nonlinear dynamic response of a system, is based on three separate tools: (i) a nonlinear dynamic solver providing a multiharmonic vibration response of the system, (ii) the contact solver based on boundary integral equations, presented in Chapter 3, that allows a refined contact analysis at the contact interface, and (iii) an energy wear approach to calculate the fretting wear of the contacting surfaces. The full approach is summarised in Fig. 4.1.

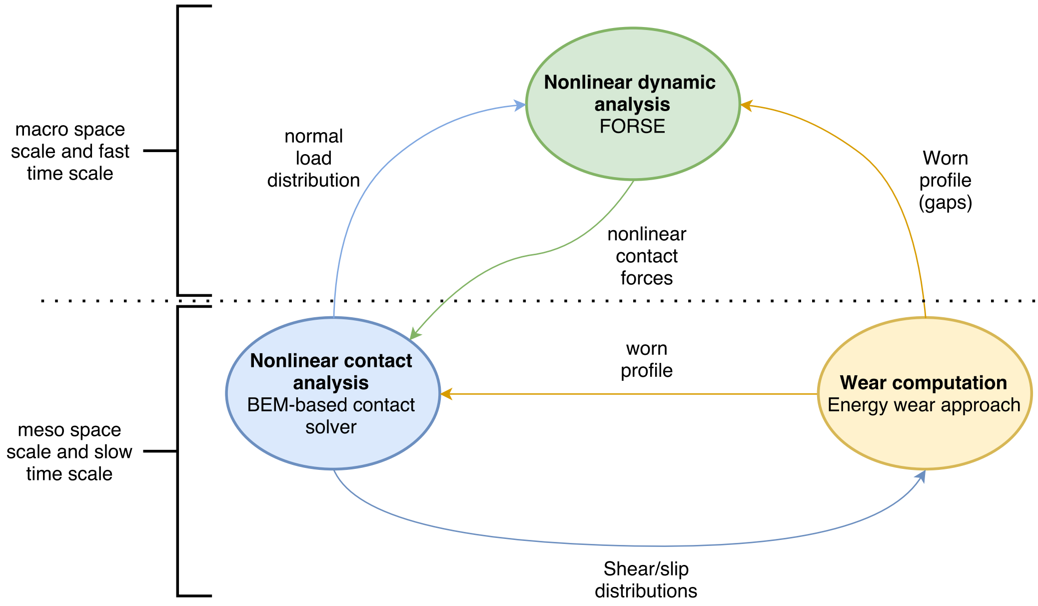

Fig. 4.1 Scheme of the multiscale analysis

It is worth noting that two assumptions were made in this approach for simplification:

- The depth of wear is considered to be (and was actually found to be, see Section 4.5.1) very small compared with the characteristic dimensions of the structures in contact, which is why the changes due to wear of the mass and stiffness matrices used in the dynamic analysis are neglected.
- The dynamic and refined contact analyses are solved separately and in an uncoupled iterative way. Therefore, wear is assumed to remain constant during the dynamic analysis, and similarly, the nonlinear dynamic contact forces are assumed to remain constant during the wear computations.

In what follows, the nonlinear dynamic analysis as well as the wear computation are described and then the proposed multiscale approach is described in detail.

4.2.1 Nonlinear dynamic analysis

The in-house code, FORSE, is used to analyse the nonlinear response of the system. FORSE is based on the multiharmonic representation of the steady-state response and allows large scale realistic friction interface modelling. The main features of the methodology can be found in [132, 135, 136, 138, 167]; in this section only a brief overview of the analysis is presented. The equation of motion of a friction joint system consists of a linear part, which is independent of the vibration amplitudes, and a nonlinear part resulting from friction at the joint interface. It can be written in the following form:

$$\mathbf{M}\ddot{\mathbf{q}}(t)+\mathbf{C}\dot{\mathbf{q}}(t)+\mathbf{K}\mathbf{q}(t)+\mathbf{f}\left[\mathbf{q}(t),\dot{\mathbf{q}}(t)\right]=\mathbf{p}(t) \tag{4.1}$$

where $\mathbf{q}(t)$ is a vector of displacements for all degrees of freedom (DOFs) in the

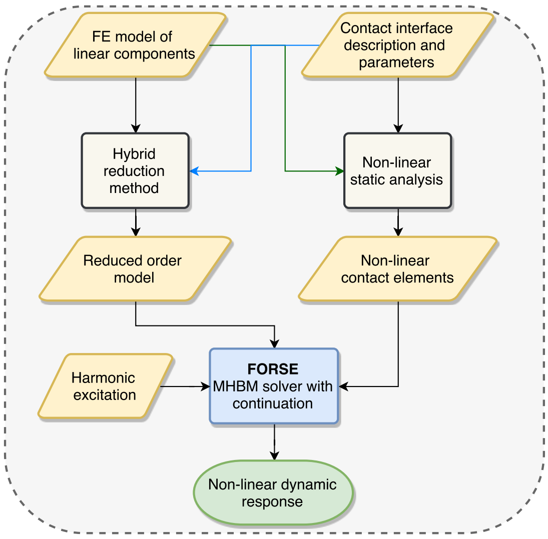

Fig. 4.2 Scheme of the forced response analysis

system; $\mathbf{K}$, $\mathbf{C}$, and $\mathbf{M}$ are stiffness, damping, and mass matrices of the linear model; $\mathbf{f}\left[\mathbf{q}(t),\dot{\mathbf{q}}(t)\right]$ is a vector of nonlinear, friction interface forces, which is dependent on displacements and velocities of the interacting nodes; and $\mathbf{p}(t)$ is a vector of periodic exciting forces. The variation of the displacements in time is represented by a restricted Fourier series, which can contain as many harmonic components as necessary to approximate the solution, i.e.,

$$\mathbf{q}(t)=\mathbf{Q}_0+\sum_{j=1}^{n}\left(\mathbf{Q}_j^c\cos m_j\omega t+\mathbf{Q}_j^s\sin m_j\omega t\right) \tag{4.2}$$

where $\mathbf{Q}_j^{c,s}$ are vectors of harmonic coefficients for the system degrees of freedom (DOFs); n is the number of harmonics that are used in the multiharmonic displacement representation; and ω is the principal vibration frequency. The flow chart of the calculations performed with the code is presented in Fig. 4.2. The contact interface elements developed in [135], for which analytical expressions for the multiharmonic representation of the nonlinear contact forces and stiffnesses were derived, are used in the analysis. In order to reduce the size of the problem and therefore its computational cost, a hybrid reduction method developed by Petrov [132, 140] is used. The nonlinear algebraic system of the resulting reduced model in the frequency domain is:

$$\tilde{\mathbf{Q}} = \mathbf{A}(\omega)(\tilde{\mathbf{F}} - \tilde{\mathbf{F}}_{\text{nl}}(\tilde{\mathbf{Q}})), \tag{4.3}$$

where $\tilde{\mathbf{Q}}$ is the vector of the Fourier coefficients of the displacements at the interface, $\mathbf{A}(\omega)$ the frequency response, $\tilde{\mathbf{F}}$ the vector of the Fourier coefficients of the excitation force and $\tilde{\mathbf{F}}_{\text{nl}}$ the vector of the Fourier coefficients of the nonlinear contact forces. This nonlinear system is solved by means of the alternating frequency time procedure (AFT) [157, 159] depicted in Fig. 4.3 where $\mathbf{s}$ denotes the tangential slips, $\mathbf{g}$ are the normal gaps and $\mathbf{w}$ are the wear depths. $\mathbf{N}_0$, k_{n} and k_{t} are contact parameters which are described in the following paragraph. DFT and iDFT refer to the Discrete Fourier Transform and the inverse Discrete Fourier Transform, respectively. $\boldsymbol{f}_{pre}$ is the prediction of the nonlinear contact forces in time domain based on a penalty method and $\boldsymbol{f}_{cor}$ is the correction of these contact forces to ensure the frictional contact laws are respected.

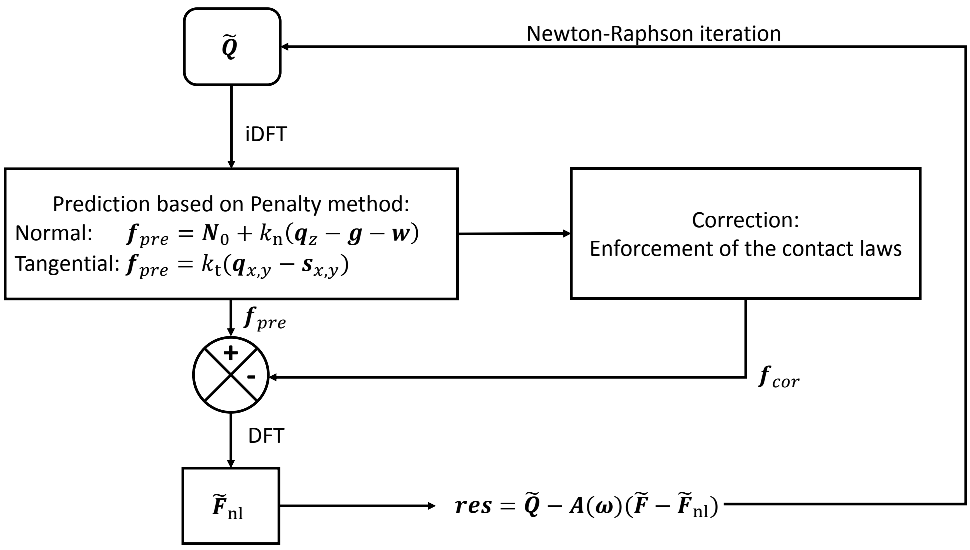

Fig. 4.3 Scheme of the AFT procedure

Prior to the analysis, a detailed Finite Element model of the system is used to extract the modal properties required for the model reduction. This Finite Element model, and more specifically the matching FE nodes on both sides of the contact interface, are also used to define the nonlinear contact elements used in the nonlinear dynamic analysis. Each friction element, depicted in Fig. 4.4, comprises two coupled Jenkins elements [54] allowing for 2D in-plane motion, and a third spring element allowing for normal load variation. Five parameters characterize its properties: the friction coefficient μ, the initial normal load N_0, a normal gap g and the tangential k_{t} and normal k_{n} contact stiffness. The values of μ, k_{n} and k_{t} are usually determined experimentally as described in [164] and are assumed to remain constant throughout the analysis. The initial normal contact condition, i.e. the normal load N_0 and normal gap g_0, are usually obtained via a nonlinear static analysis using a Finite Element software.

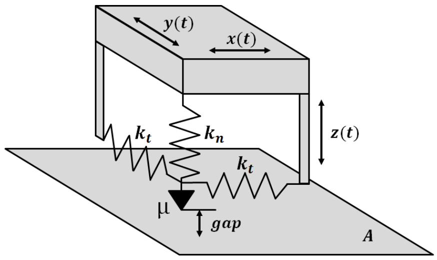

Fig. 4.4 Friction interface element

4.2.2 Wear computation

Once the normal and tangential contact conditions have been calculated with the BEM-based contact solver, the energy wear approach [45, 69, 122, 152] is used to compute fretting wear. In this approach, the total wear volume obtained after N_{cycles} is assumed to be proportional to the accumulated dissipated energy:

$$V = \alpha \sum_{n=1}^{N_{\text{cycles}}} Ed_n \tag{4.4}$$

where α is a wear coefficient and Ed_n is the dissipated energy due to friction during the n_{th} cycle.

In order to perform a refined local contact analysis accounting for wear, a local form of Eq. 4.4 is used:

$$\Delta h_{ij} = \alpha \int_0^T \left\|\mathbf{q}_{ij}(t)\right\| \left\|\Delta \mathbf{v}_{ij}(t)\right\| dt \tag{4.5}$$

where Δh_{ij} is the wear depth at each node after one cycle, $\mathbf{q}_{ij}$ and $\Delta \mathbf{v}_{ij}$ are respectively the vectors of the two tangential shear stresses and the relative tangential velocities at the grid point (i, j), and T is the duration of one vibration cycle.

As can be seen in Eq. 4.5, the accuracy of the wear computation highly depends on the accuracy of the wear coefficient α. Therefore, dedicated fretting wear measurements should be performed on the used couple of materials and on a test rig representative of the operating conditions of the system in order to obtain an accurate energy wear coefficient and hence accurate wear predictions.

Due to the lack of such relevant experimental data, the wear coefficient used in the analysis presented in Section 4.5.1 is based on Leonard [90] and is equal to $2 \times 10^3\,\mu m^3\,J^{-1}$ for a steel-steel fretting contact.

4.2.3 Proposed multiscale approach

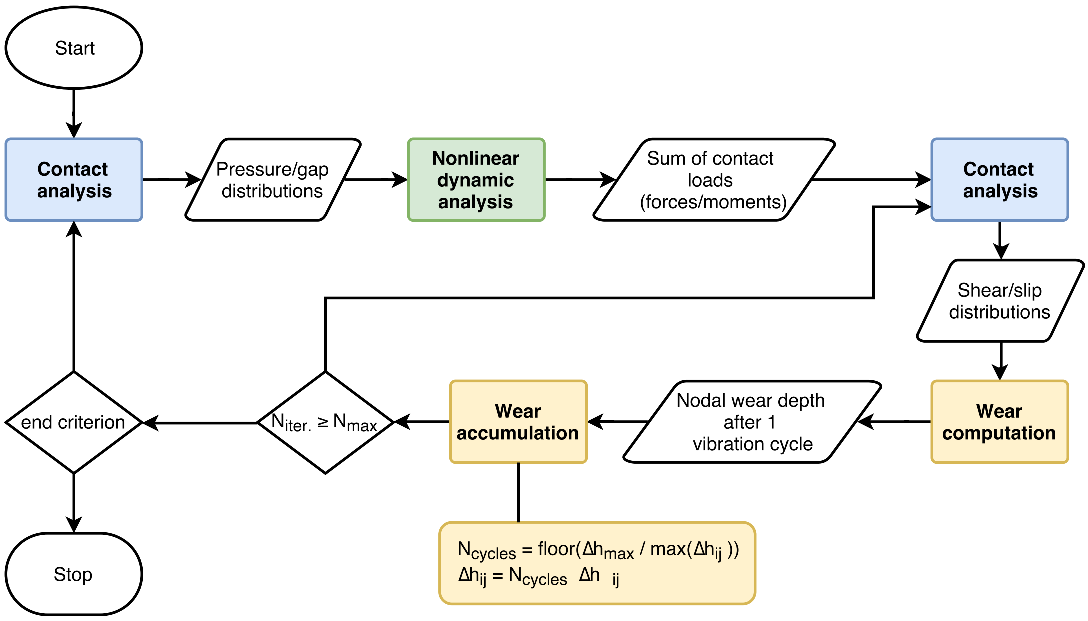

Fig. 4.5 Detailed scheme of the multiscale analysis

The multiscale approach, summarised in the flow chart in Fig. 4.5, is as follows. First of all, an initial contact analysis is performed using the BEM-based contact solver to provide the static pressure and gap distributions required for the definition of the 3D contact elements used in FORSE. The necessary input for this first contact analysis is the total normal load, known to be transmitted through the contact area. Then, a nonlinear dynamic analysis is conducted in FORSE to obtain the unworn nonlinear dynamic response and the contact loads (forces and moments) at the interface. The sum of the contact loads at resonance, including the normal force N, the two tangential forces T_x and T_y, the two bending moments M_x and M_y and the torsional moment M_z, are then computed at the centre of the contact area using the following expressions:

$$\begin{aligned} N &= \sum_i N_i, \\ T_x &= \sum_i T_{x_i}, \\ T_y &= \sum_i T_{y_i}, \\ M_x &= \sum_i -N_i y_i, \\ M_y &= \sum_i N_i x_i, \\ M_z &= \sum_i \left(T_{x_i} y_i - T_{y_i} x_i\right), \end{aligned} \tag{4.6}$$

where i denotes the i-th friction element and x_i and y_i are the distance between the i-th friction element and the centre of the contact area along the x and y direction respectively. These loads are converted from the frequency domain into the time domain using an inverse Discrete Fourier Transform, so that the contact loads over one vibration cycle are obtained. The resulting forces and moments are input into the contact solver to obtain refined pressure, shear and slip fields for each time step of the fretting cycle. The convergence of the solution for each time step is ensured by enforcing the residuals of the conjugate gradient to be minimum within a given tolerance, as described in Chapter 3.

The energy wear approach is then used to calculate the wear depth across the contact surface. The wear obtained after only one vibration cycle is so small that it would not result in any noticeable change of the contact conditions, and consequently would not impact the nonlinear dynamic response in any significant way. For that reason, a number of cycles N_{cycles} are accumulated before the refined contact analysis is performed again (referred to as a 'wear iteration'). This number of cycles, which represents a factor that makes the analysis faster, is defined as follows:

$$N_{\text{cycles}} = floor\left(\frac{\Delta h_{\max}}{\max \Delta h_{ij}}\right) \tag{4.7}$$

where $\Delta h_{\max}$ is the maximum allowed wear depth during one wear iteration and $\max \Delta h_{ij}$ is the maximum computed wear depth across the contact interface after one fretting cycle. It is worth noting that, based on this formula, each wear iteration can correspond to a different number of cycles. This factor is a very critical parameter of the analysis since it will determine the computational cost of the contact analysis, as well as the stability of the explicit scheme used to update the contacting surface profile with wear:

$$h_{ij} = h_{ij} + N_{\text{cycles}} \Delta h_{ij} \tag{4.8}$$

A large value of the factor will lead to a reduced computational time but also to a more likely occurrence of singularities in the worn profile that will reduce the accuracy of the analysis.

The nonlinear dynamic model is updated at a lower frequency which can be based on a given number of wear iterations or on the total wear volume. In other words, a number of wear iterations are computed within the contact solver until the changes of surface profile due to wear, leading to changes in the pressure distribution, are thought to have a noticeable impact on the nonlinear dynamic response of the system. This number of allowable wear iterations is the second critical parameter of the analysis since it will also determine the computational cost of the approach as well as its accuracy. Moreover, it is very difficult to find the appropriate value for this parameter *a priori*, especially due to the fact that it may change over time depending on the wear dynamics. Therefore, a number of trials are required before finding an optimum value for that parameter. The same goes for the wear accumulation factor.

Once an appropriate number of wear iterations have been performed, the 3D nonlinear contact element definition is updated with the new worn profile and the corresponding new static pressure distribution obtained from the contact solver, and a new nonlinear dynamic response is computed, which provides an updated set of contact forces to the wear computation. This procedure is continued until either a maximum total number of cycles or a maximum total wear volume at the contact interface has been reached.

4.3 Underplatform damper system test case

The test case selected to demonstrate the developed analysis technique is a blade-damper system, which is a very common mechanical structure in high pressure turbines (HPT) with a well-understood nonlinear dynamic behaviour. Past experience indicates that significant wear can occur at the damper during operation, but its effects on the bladed-disk dynamics are normally neglected. A simplified blade-damper geometry of a recently developed underplatform damper test rig [128] will be used to demonstrate the change in the nonlinear dynamic response due to damper wear.

4.3.1 Linear Finite Element Model

Using the Rolls-Royce in-house finite element (FE) code SC03, a full three-dimensional finite element model, depicted in Fig. 4.6, has been generated with quadratic hexahedral elements for both blades ($54,972$ elements) and the damper ($3,620$ elements).

Particular care has been taken to refine the mesh at the contact interfaces to allow the introduction of a sufficient number of friction elements for the nonlinear dynamic analysis. This fine discretisation of the contact is required to capture local microslip effects which play a critical role in the wear process. The wear analysis will focus on the first out-of-phase flap mode of the two blades (see Fig. 4.6) which shows no damper rotation and therefore maximises the dissipated energy and wear at the contact interfaces.

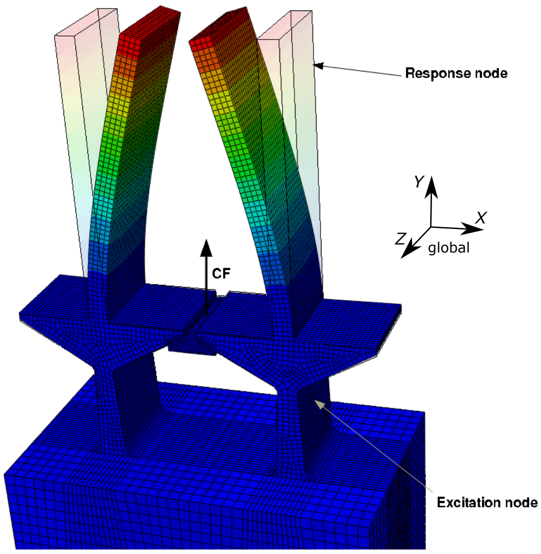

Fig. 4.6 1st out-of-phase flap mode of the two blades

4.3.2 Nonlinear Contact Model

The coupling between the blades and the damper is achieved by 152 full three-dimensional friction elements at each blade-damper interface, as shown in Fig. 4.7 where each sphere represents a friction element. The chosen number of elements

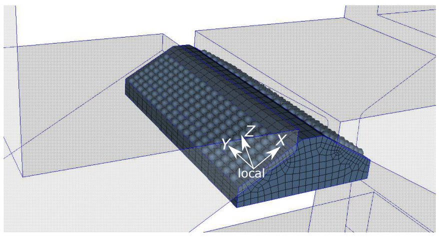

Fig. 4.7 Nonlinear contact element locations

enables a good discretisation of the contact area, while keeping the computational time acceptable. Each friction element has a normal and tangential contact stiffness of $6 \times 10^4\,\mathrm{N\,mm^{-3}}$, based on experimental measurements [164].

Table 4.1 Underplatform damper - calculation parameters

Parameter	Value
Young's modulus of the blade, E_1 [GPa]	210
Young's modulus of the damper, E_2 [GPa]	210
Poisson ratio of the blade, ν_1	0.3
Poisson ratio of the damper, ν_2	0.3
Friction coefficient, μ	0.6
Damper angle, θ [deg]	30
Normal load, N [N]	428.81

4.4 Nonlinear dynamic predictions of the unworn system

4.4.1 Static Normal Load

The BEM-based contact solver was used to solve the normal contact problem between the damper and the blade; this provides the accurate static normal load required to perform the initial nonlinear dynamic analysis. The input parameters for this computation are given in Tab. 4.1. The normal load on each contact patch is derived from the centrifugal load $CF = 1 \times 10^3$ N, applied to the damper, as shown in Fig. 4.8, using the following formula:

$$N = \frac{1}{2} \frac{CF}{(\cos(\theta) + \mu \sin(\theta))} \tag{4.9}$$

where θ is the damper angle and μ is the friction coefficient. This expression of N is coming from the force equilibrium of the damper assuming that the damper angle θ satisfies the slip condition, i.e. $\tan(\theta) \geq \mu$, in which case the tangential force between the damper and the blade surfaces equals its Coulomb limit μN.

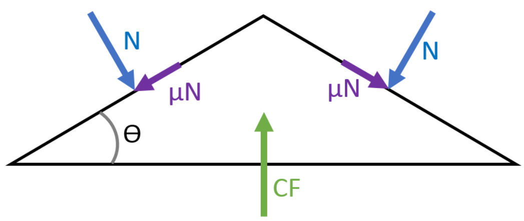

Fig. 4.8 Damper geometry and applied loads

Each face of the blade-damper contact interface is discretised into a regular grid of 128 × 128 elements for the contact analysis since it was shown to be a good compromise between accuracy and computational cost in Chapter 3. The contacting surfaces are assumed to be perfectly flat and smooth such that there is no initial separation between the damper and the blade. The calculated pressure distribution, presented in Fig. 4.9., led to a uniform central part and exhibited higher values along the boundaries of the contact area, which is expected given the singularity of the stress fields at these locations. From this very detailed pressure distribution, the value at each

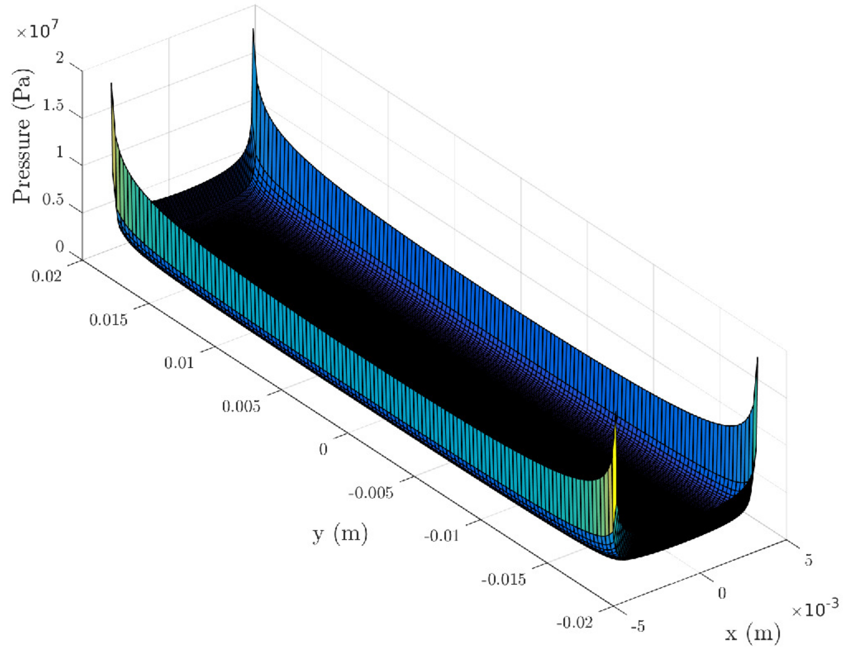

Fig. 4.9 Initial pressure distribution

nonlinear contact node was linearly interpolated to provide the initial static pressure required for the nonlinear dynamic analysis in FORSE. A scaling factor was applied to these interpolated values to ensure the load equilibrium was still fulfilled after interpolation. None of the nonlinear nodes is located on the boundaries of the contact area, which mitigates the impact of the boundary effects inherent to the flat-on-flat contact geometry.

4.4.2 Nonlinear dynamic behaviour of the unworn system

An initial nonlinear dynamic analysis was performed on the unworn system. In that analysis, as well as in the subsequent ones, the first three harmonics, plus the harmonic 'zero' (static term), were included in the Fourier truncated representation of the response, since it was shown in [128] that these were enough to accurately capture the nonlinear behaviour of this system. The excitation and response node locations, as well as the global coordinate system, are shown in Fig. 4.6; the excitation and response are in the X direction of that coordinate system. Figure 4.10 shows the nonlinear frequency response functions of the first out-of-phase flap mode of the unworn blade-damper system under a very low excitation level (0.1 N) that leads to a linear behaviour, and under a higher excitation (17 N) for which a strong nonlinear behaviour can be observed. The nonlinear behaviour is due to the transition of some

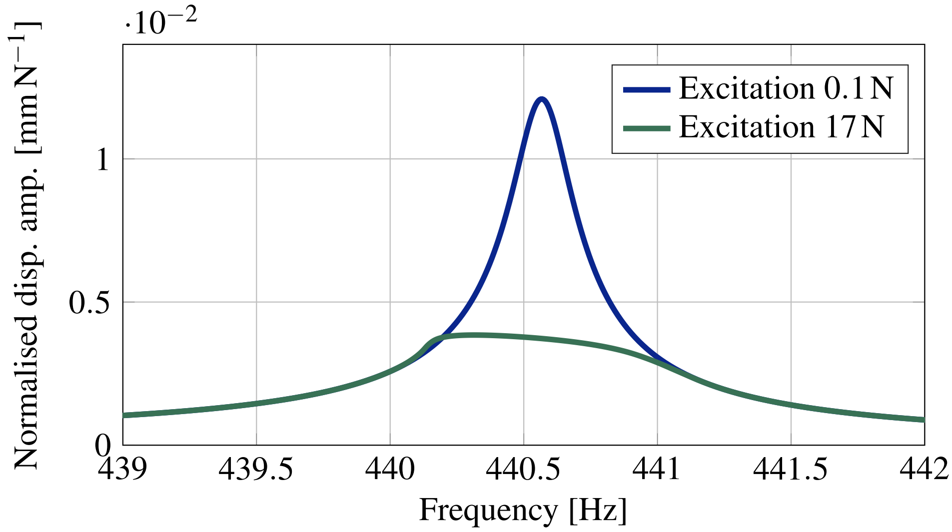

Fig. 4.10 Frequency response function of the unworn system

of the frictional elements in the contact area from stick to slip at resonance. This behaviour is illustrated in Fig. 4.11 which shows the state of the nonlinear contact elements at resonance under the 17 N excitation. It can be seen that the lower parts

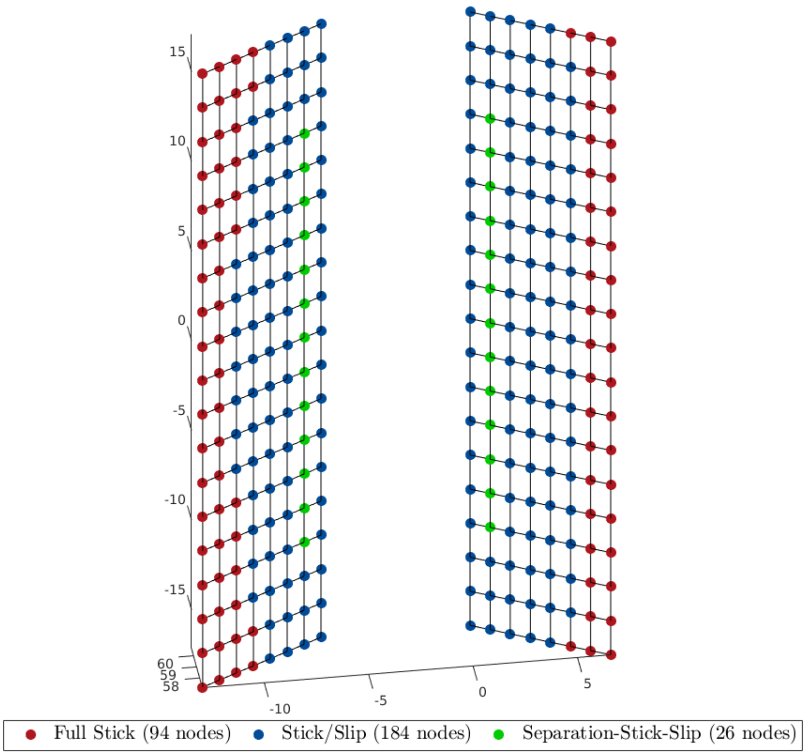

Fig. 4.11 Contact conditions at resonance

of the damper remain fully stuck while the rest of the elements experience stick-slip transitions. A line of contact elements (green color in the plot) near the upper edge of the patch even experiences separation during the vibration cycle. This separation is due to the widening of the upper gap between the platforms during a vibration cycle.

Figure 4.12 shows the normal and tangential force fields at resonance at the point in the vibration cycle when the total tangential force is maximum. It can be seen that the tangential forces at the nodes F_t are mostly orientated in the x direction (of the local coordinate system shown Fig. 4.7), and that the normal load F_n shows a gradient along the x direction, which results in the moment M_y shown in Fig. 4.14. These results

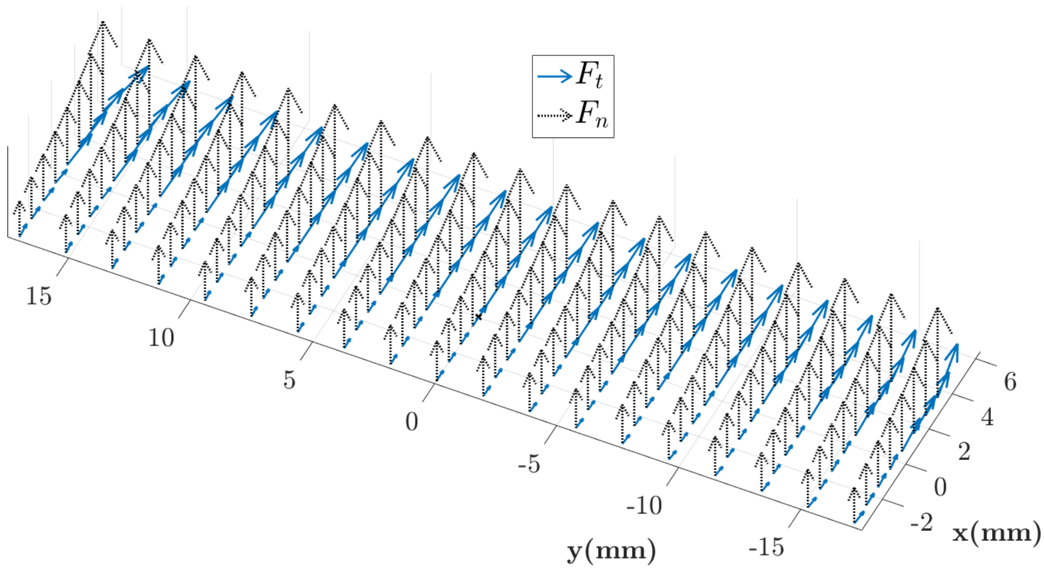

Fig. 4.12 Normal and tangential force fields at resonance

are consistent with the expected physical behaviour of the blade-damper system; for the first out-of-phase flap mode, the damper is moving straight up and down, leading to only one component of tangential forces (F_x) combined with the normal force F_n. Furthermore, when the damper experiences this pure translation, a relative rotation around an off-centred line between the two contact surfaces generates a moment M_y, as can be observed in the vector plot of Fig. 4.12.The moments M_y on the right and left side of the damper are equal and opposite, so that they have no effect on the damper motion. As previously discussed, the contact solver requires the total forces and moments at the centre of the contact patches as inputs. Figure 4.13 shows the sum of the nodal forces on the left contact patch during one vibration cycle at resonance for a 17 N excitation and Fig. 4.14 shows the sum of the moments. The total loads on the right contact patch are nearly identical to those on the left contact patch due to the symmetry of the system and of the considered mode, which is why they are omitted here.

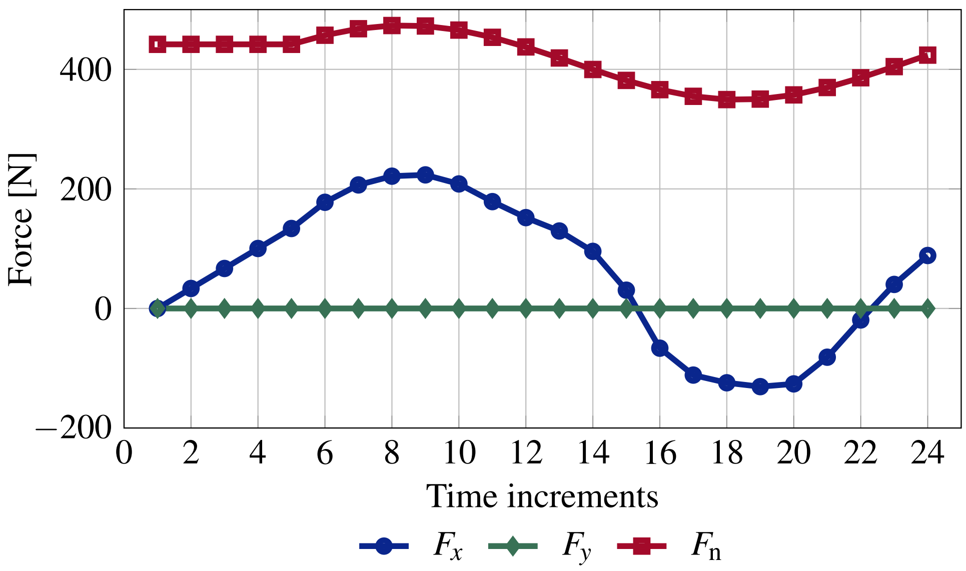

Fig. 4.13 Total forces at the centre of the left contact patch

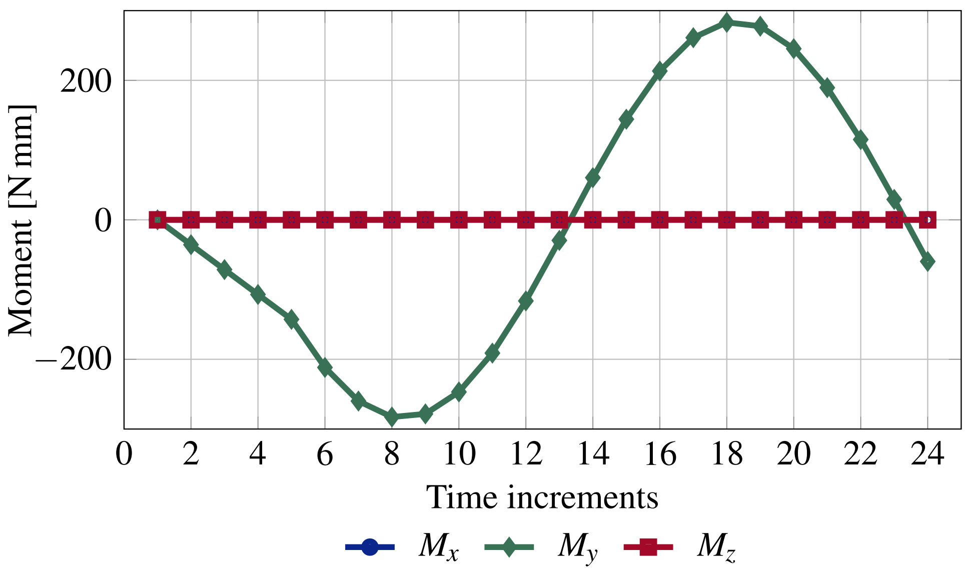

Fig. 4.14 Total moments at the centre of the left contact patch

4.5 Fretting wear predictions and impact on the dynamic response

4.5.1 Refined contact analysis and wear computations

Following the computation of the nonlinear forces at the centre of the contact interfaces, these values are input into the contact solver to obtain more accurate contact conditions for the wear calculation. For this analysis, the input parameters were the same as those presented in Tab. 4.1. The results are used in conjunction with the energy wear approach to compute the fretting wear at the contact interface.

Figure 4.15 shows the total wear depth obtained after 500 and 1,000 wear itera-

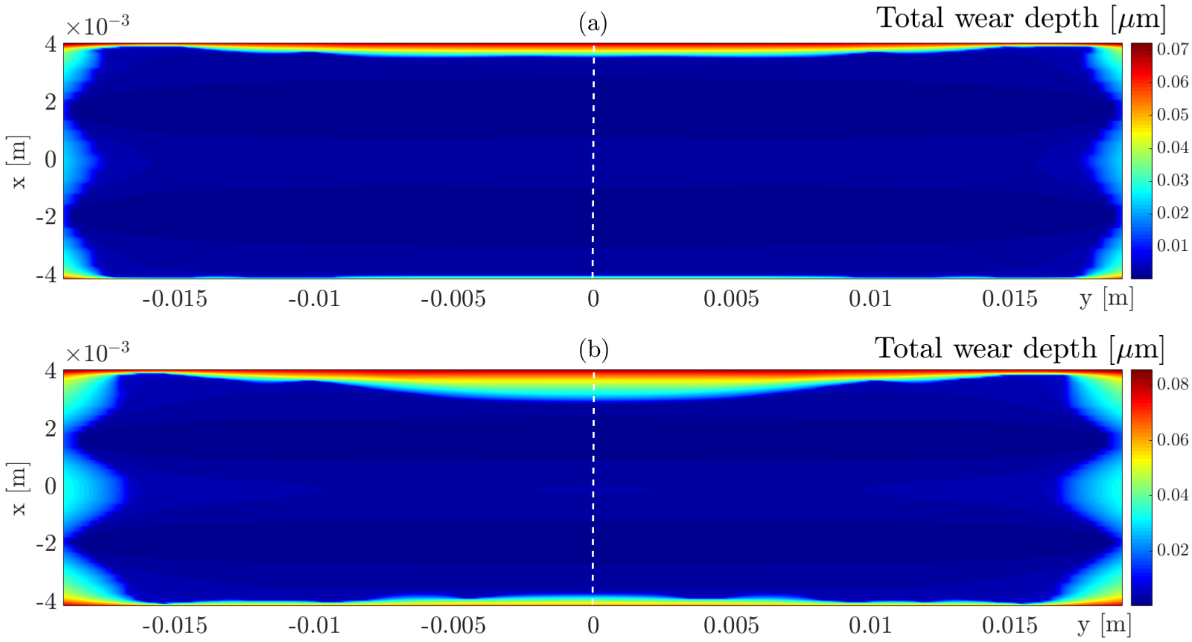

Fig. 4.15 Wear patterns after (a) 500 and (b) 1,000 iterations

tions (which corresponds to approximately 5.7e9 and 1.1e10 vibration cycles). It can be seen that the wear is concentrated along the four edges of the contact patch where the moment M_y around the y-axis leads to a slightly asymmetric pressure and more wear on the top edge of the contact patch. Figure 4.16 displays the evolution of the pressure distribution with wear along the white dotted line drawn in Fig. 4.15. Once

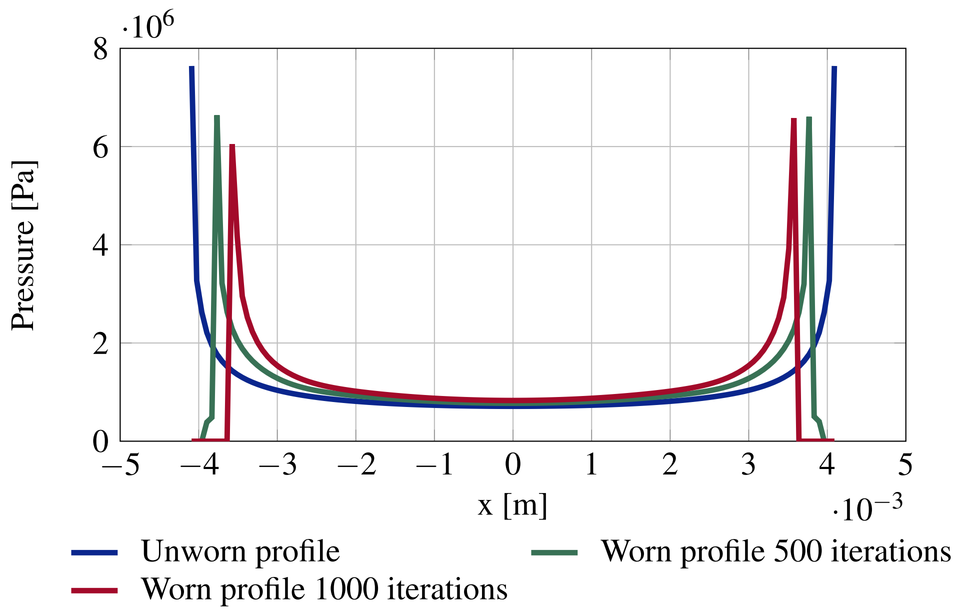

Fig. 4.16 Impact of wear on pressure distribution

the edges of the contact patch are worn out, the pressure distribution is no longer singular at these locations and bounded peaks are now observed at the boundaries of the newly worn contact patch. This redistribution of the pressure leads to a slight increase at the centre of the contact interface, creating a new initial condition for the nonlinear dynamic analysis. These results were obtained using MATLAB on a regular workstation (Intel Core i3-4340 3.6GHz); each wear iteration took approximately 80 seconds (wall clock time).

4.5.2 Impact of wear on the nonlinear dynamic response

Figure 4.17 shows the nonlinear FRFs obtained for three different worn configurations: for the first two configurations, the nonlinear dynamic model is updated only once after 500 and 1,000 wear iterations. For the third configuration, the nonlinear dynamic model is updated every 500 iterations. These simulations were run on a cluster node with a 20-core CPU Intel Xeon E5-2620 2GHz and lasted approximately 5h45min each (wall clock time).

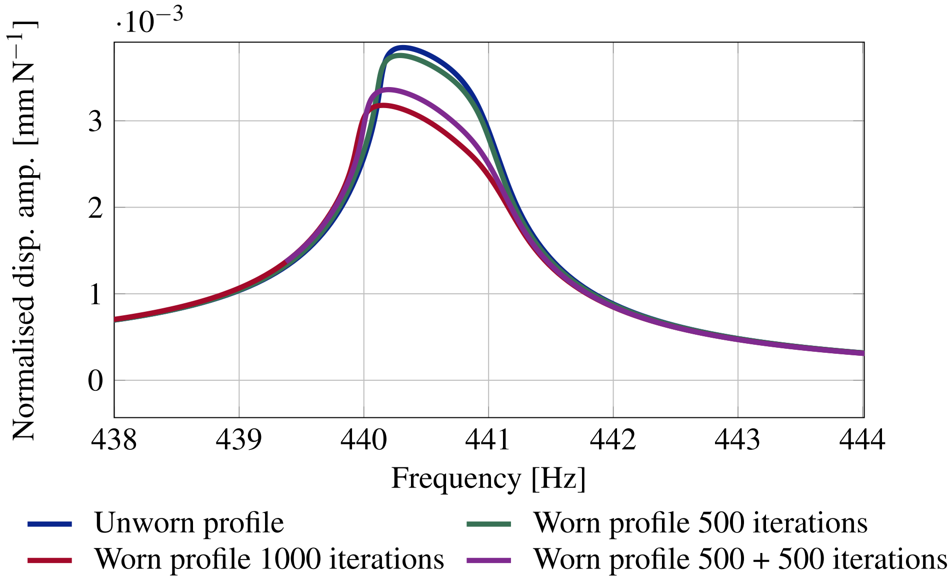

Fig. 4.17 Impact of wear on the nonlinear FRF

It is very interesting to see that even with a wear scar covering only a small area and a maximum local wear depth smaller than 0.1 µm, a significant impact on the nonlinear response of the system can be observed, especially in terms of damping. A notable difference can be seen between the response obtained after updating the nonlinear dynamic model every 500 and 1,000 iterations, which indicates that the nonlinear dynamic model should be updated more often. As previously discussed, updating the nonlinear dynamic model after every wear iteration would not be sound because the amount of wear at each iteration is so small that it would result in no noticeable impact on the dynamic response. Furthermore, the computational cost of such a process would be prohibitive, which is why an optimum number of wear iterations should be computed before updating the nonlinear dynamic model. From the presented FRFs, since the responses after $1,000$ wear iterations with (purple line in Fig. 4.17) and without (red line in Fig. 4.17) an update of the dynamic model every 500 wear iterations do not line up, it means that the dynamic model should be updated after less than $1,000$ wear iterations, but it cannot be concluded that an update every 500 wear iterations is enough based on these results alone. Further investigation will be led in Chapter 6 to determine the optimal number of wear iterations before updating the nonlinear dynamic model.

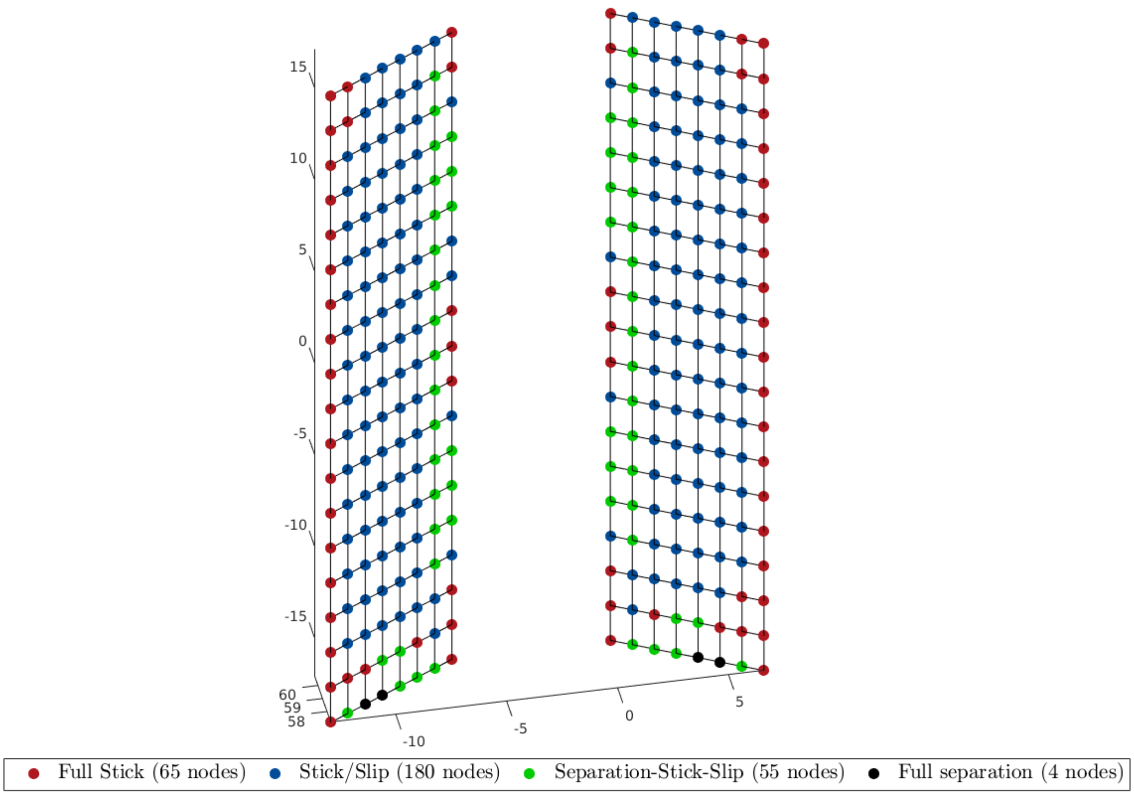

Fig. 4.18 Contact conditions at resonance with the worn profile

Figure 4.18 shows the contact conditions at resonance obtained with the worn profile after $1,000$ wear iterations. The lower pressure at the edges of the contact area, as seen in Fig. 4.16, results in more nodes experiencing separation and stick-slip transitions during the vibration cycle, which in turn leads to a lower resonance frequency and a larger energy dissipation.

4.6 Discussions from a turbomachinery design perspective

The dynamic responses shown in Fig. 4.17 may lead to a very appealing conclusion with regards to wear which is that the damping increases with wear. This means that over time, the turbine blades in this particular case, will be subjected to vibrations of lower amplitude, which will increase their performance and extend their lifetime. However, what may happen is that after a higher number of wear iterations, a turning point may occur at which the damping will decrease and therefore the vibration amplitude will increase again. The only conclusion that can be asserted at this point is that the effects of wear are such that they must be included in the design analysis.

Another question that may be raised by a design engineer is the loading case used in the wear simulations. As discussed earlier, the wear has been computed at resonance since it was thought to be the point where the vibration amplitude would be maximum and therefore where maximum frictional dissipated energy would be observed. However, under operating conditions, and more precisely during each flight cycle, the blade-damper system will not be excited at resonance all the time. Therefore, computing wear at resonance frequency alone would not be representative of the conditions experienced by the system. On top of that, assuming that the damping due to wear is maximum at resonance frequency, it would not be conservative to use this as the only loading case.

For the analysis of a real turbomachinery, what should actually be considered is the static wear due to the take-off and landing phases for a given operation cycle and a combination of that static wear with the vibration wear, that has been studied here, at resonances. Although the tools presented in this chapter were only used to compute wear at resonance, the BEM-based contact solver could also be used in combination with the energy wear approach to compute the static wear, as long as the operation cycle quasi-static loads are available inputs.

4.7 Conclusions

In this chapter, a multiscale approach was proposed to evaluate fretting wear and predict its impact on the nonlinear dynamic response of a blade-damper system. A combination of a multiharmonic balance solver, a BEM-based contact solver and the energy wear approach allowed an accurate and computationally efficient contact analysis and wear computation. The presented results highlight the sensitivity of the nonlinear dynamic response to changes at the contact interface; the wear patterns led to a redistribution of the contact pressure, which in turn changed the underlying nonlinear mechanisms at the interface from sliding at the edges only to sliding over a larger part of the contact interface. As a result, wear must be included in the analysis in order to accurately predict the nonlinear dynamic response of an assembled structure over its lifetime. Two parameters were shown to be critical with respect to the computational cost and the accuracy of the proposed approach: the wear accumulation factor and the number of wear iterations after which the nonlinear dynamic model should be updated.

Chapter 5

Extension of the multiscale approach to rough contact analysis

5.1 Introduction

Chapter 5 presents an upgrade of the proposed multiscale approach to include the effects of surface roughness in the analysis and therefore have a more realistic modelling of the contact interface. After introducing a few key roughness concepts and showing how to numerically generate rough surfaces, the contact solver results will be discussed. After that, an upgrade of the previously presented multiscale approach will be introduced and then the effects of surface roughness on contact conditions and in turn on the nonlinear dynamics response will be illustrated on a single bolted joint system.

5.2 Roughness concepts

In this section, a few basic roughness concepts will be presented in order to provide the necessary background to understand the work presented here. Much more detailed informations about surface roughness and rough contact modelling can be found in [67, 77, 125, 126, 147, 183]. In contact mechanics, surface morphology plays an essential role in determining how solids interact with one another, with significance in many processes including friction and wear. The classic Hertzian contact theory considers elastic solids with smooth profiles of curved surfaces connecting the applied force and indentation depth, by assuming a distribution of normal pressure in the contact area. However, this assumption neglects topological features of real surfaces and the interaction between individual contact regions. Due to surface roughness, only a certain number of peaks or asperities are actually in contact. Since the true contact

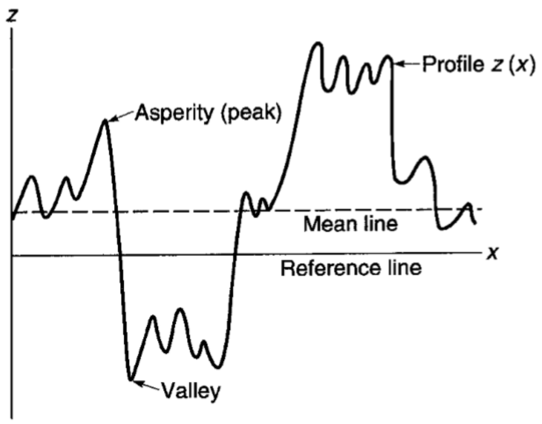

Fig. 5.1 Rough surface profile [13]

area at an individual asperity can be of nano-scale dimensions, the real contact area between two surfaces is typically orders of magnitude smaller than the apparent or nominal contact area.

Surface roughness is a measure of the topographic height variations of the surface. The roughness can arise from polishing marks, machining marks, marks left by rollers, dust or other particles and is basically shaped by the full history of the surface from the forming stages to the finishing processes. Rough surfaces are commonly divided into the subcategories of deterministic and random surfaces. Deterministic surfaces have a prescribed shape, usually of a simple form such as triangular, rectangular or sinusoidal and are as such easily implemented in surface modelling applications. Random surfaces, on the other hand, are stochastic and a result of a random process and are usually characterised using terms from probability theory such as standard deviation and covariance, as presented hereafter. This second type of rough surfaces, which is more realistic, has been used in this work.

Standard deviation is a well accepted statistical measure for a surface roughness description. It quantifies surface height variability with regards to the average value of surface heights and can be defined as:

$$\sigma = \sqrt{\frac{1}{N}\sum_{1}^{N}(h_i - \bar{h})^2} \tag{5.1}$$

where $\bar{h}$ is the height average value, also called R_a roughness or centre line average (CLA) and defined as:

$$\bar{h} = R_\mathrm{a} = CLA = \frac{1}{N}\sum_{i=1}^{N}|h_i| \tag{5.2}$$

The root-mean-squared height is very similar to the standard deviation except that it is not defined relative to the average height value, which means that it estimates an

Roughness N ISO Grade Numbers	Roughness values R_a micrometers (μm)	Roughness values R_a microinches (μin)	RMS roughness microinches (μin)
N12	50	2,000	2,200
N11	25	1,000	1,100
N10	12.5	500	550
N9	6.3	250	275
N8	3.2	125	137.5
N7	1.6	63	64.3
N6	0.8	32	32.5
N5	0.4	16	17.6
N4	0.2	8	8.8
N3	0.1	4	4.4
N2	0.05	2	2.2
N1	0.025	1	1.1

Table 5.1 Roughness parameters for different grade numbers

absolute magnitude of height variation:

$$R_q = \sqrt{\frac{1}{N}\sum_{1}^{N} h_i^2} \tag{5.3}$$

Table 5.1, extracted from the ISO 1302, gives typical values of R_a and R_q roughness for different grade numbers.

These first three parameters are amplitude parameters, describing the surface variation in the vertical direction. The surface variation in the lateral directions can be described using the autocovariance function and the correlation lengths. The autocovariance function ACF describes the covariance (correlation) of the surface with versions translationally shifted of a lag value l_j:

$$ACF(l_j) = \frac{1}{N}\sum_{i=1}^{N} h(x_i)h(x_i + l_j) \tag{5.4}$$

The correlation length is defined as the value for which the autocovariance function falls below $1/e$ of its zero lag value. A physical interpretation is that it describes a typical distance between two similar features (e.g. hills or valleys).

5.3 Generation of rough surfaces

For modelling and simulating purposes, random rough surfaces with Gaussian statistics can be generated using a method outlined by Garcia and Stoll [52], where an uncorrelated distribution of surface points using a random number generator (i.e. white noise) is convolved with a Gaussian filter to achieve correlation. This convolution is most efficiently performed using the discrete Fast Fourier Transform (FFT) algorithm, which in MATLAB is based on the FFTW library [48]. This method has been used in the present work. The associated MATLAB code is provided by David Bergstrom [10]. The necessary inputs are the number of surface points N, the length of the surface L, the root-mean-squared roughness R_q and the correlation lengths cl_x and cl_y along x and y directions respectively. The outputs are the heights of a surface having a Gaussian height distribution and Gaussian autovariance functions in both x and y directions.

Figure 5.2 shows the Gaussian rough surfaces generated on a grid of 256×256 points for different values of RMS roughness and correlation lengths. The heights of these profiles have been magnified 100 times to allow visualisation of the roughness.

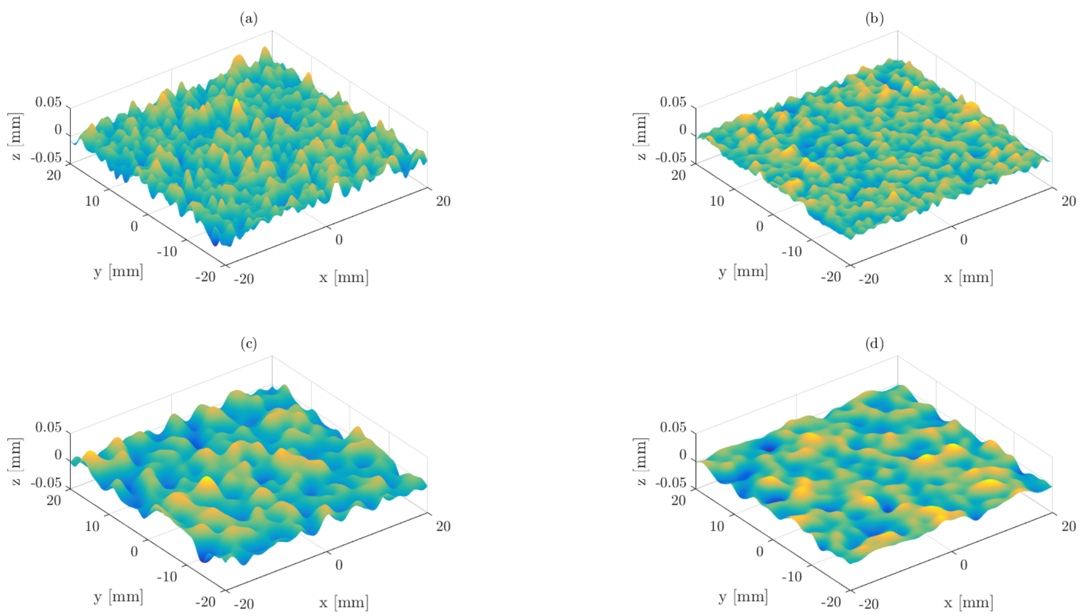

Fig. 5.2 Gaussian rough surface with (a) $R_q = 10\,\mu\text{m}$; $cl_x = cl_y = 1\,\text{mm}$, (b) $R_q = 5\,\mu\text{m}$; $cl_x = cl_y = 1\,\text{mm}$, (c) $R_q = 10\,\mu\text{m}$; $cl_x = cl_y = 2\,\text{mm}$ and (d) $R_q = 5\,\mu\text{m}$; $cl_x = cl_y = 2\,\text{mm}$

In order to evaluate the quality of the generated surfaces with regards to the input parameters, equations 5.3 and 5.4 have been used to recompute the characteristics of the generated surfaces. It was shown that using 256×256 points and a ratio $\dfrac{L}{cl_x} = 70$ allowed to obtain less than 1% error between the specified roughness parameters and the simulated one.

5.4 Refinement of the multiscale approach

The multiscale approach presented in chapter 4 was initially developed for the analysis of smooth contact. Significant modifications and refinements to this initial approach were necessary to allow rough contact analysis. In this new version of the approach, the normal and tangential contact stiffnesses are now also computed using the BEM-based contact solver, in addition to the normal load and gap, which provides improved input data, depending on surface roughness, to the friction elements used in the nonlinear dynamic analysis.

Initially, a refined contact analysis is performed using the contact solver on the whole contact interface. The applied loading is the total normal load transmitted through the contact area, which in case of a bolted joint corresponds to the tightening force of the bolt. The result of this analysis is a normal load and gap distribution which can be used to define all the 3D nonlinear contact elements used in FORSE. This was part of the proposed multiscale approach introduced in Chapter 4.

The refinement consists in performing a separate contact analysis to extract the normal and tangential contact stiffness. The normal problem is first solved for the whole contact surface for a normal load varying between 99% and 101% of the tightening force of the bolt. From these simulations, the characteristic 'normal load - indentation' curve can be computed for each part of the contact area representing a nonlinear friction element. The slope of the tangent to that curve for a normal load equal to the tightening force of the bolt gives the localised normal contact stiffness k_n. Then, the tangential problem is solved for a few values of load which are small enough to keep the contact in full stick condition, for which the tangential force evolves linearly with the relative tangential displacement. The tangential contact stiffness k_t of each nonlinear friction element can be extracted from the obtained linear part of the frictional hysteresis loop.

Prior to applying this updated multiscale approach to a more complex system, the extraction of the normal and tangential contact stiffness from the contact solver was tested and validated against analytical solutions for the smooth Hertzian contact. A normal load varying from 10 N to 1,000 N has been applied to the spherical contact described in Chapter 3. The indentation depth was computed for each normal load so that a normal load vs indentation depth curve and therefore the normal contact stiffness could be obtained. On the other hand, the analytical expression of the stiffness can be derived from Eq. 3.67:

$$\delta_z = \left(\frac{9N^2}{16RE^{*2}}\right)^{1/3} \tag{5.5}$$

where R is such that $\frac{1}{R} = \frac{1}{R_1} + \frac{1}{R_2}$ and E^* is such that $\frac{1}{E^*} = \frac{1-\nu_1^2}{E_1} + \frac{1-\nu_2^2}{E_2}$.

$$\frac{d\delta_z}{dN} = \left(\frac{9}{16RE^{*2}}\right)^{1/3} * \frac{2}{3} * N^{-1/3} \tag{5.6}$$

$$k_\mathrm{n} = \frac{dN}{d\delta_z} = \frac{3}{2}\left(\frac{16RE^{*2}N}{9}\right)^{1/3} \tag{5.7}$$

Figure 5.3 shows the comparison between the numerical solution obtained using the contact solver and the analytical solution, and shows that an accurate normal contact stiffness can be extracted from the contact solver. Similarly, numerical values of

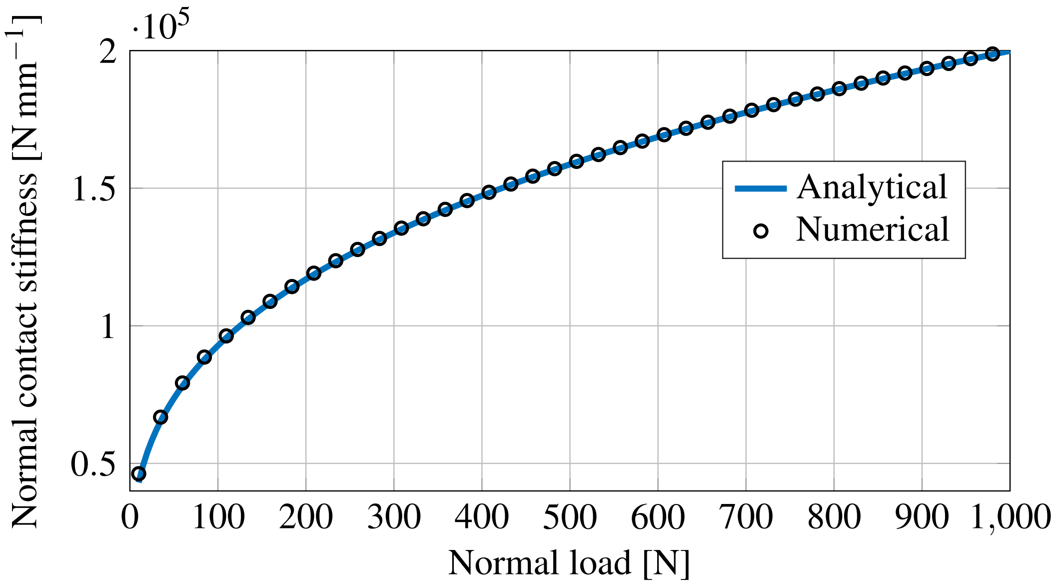

Fig. 5.3 Normal contact stiffness for different normal loads

tangential contact stiffness were extracted from the contact solver for each value of the normal load N. The analytical expression of that contact stiffness can be derived from Eq. 3.74, which yields to:

$$\frac{1}{k_\mathrm{t}} = \frac{1}{4a}\left(\frac{(2-\nu_1)(1+\nu_1)}{E_1} + \frac{(2-\nu_2)(1+\nu_2)}{E_2}\right) \tag{5.8}$$

The comparison between the numerical prediction and the analytical expression of the tangential contact stiffness is presented in Fig. 5.4 which shows that the tangential contact stiffness can also be accurately extracted using the contact solver. Expectedly, since both the normal and tangential contact stiffnesses, extracted from the contact

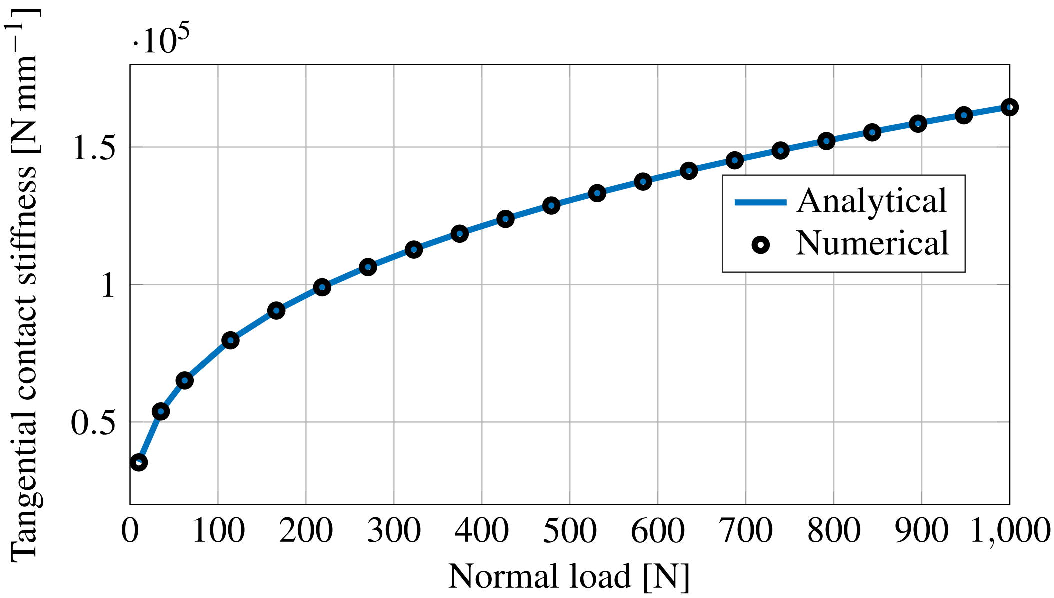

Fig. 5.4 Tangential contact stiffness for different normal loads

solver, are in line with their analytical counterparts, the ratio between k_t and k_n verifies Mindlin formula 5.9, as shown in Fig. 5.5.

$$\frac{k_\mathrm{t}}{k_\mathrm{n}} = \frac{2(1-\nu)}{(2-\nu)}, \tag{5.9}$$

where ν is the Poisson ratio of the material.

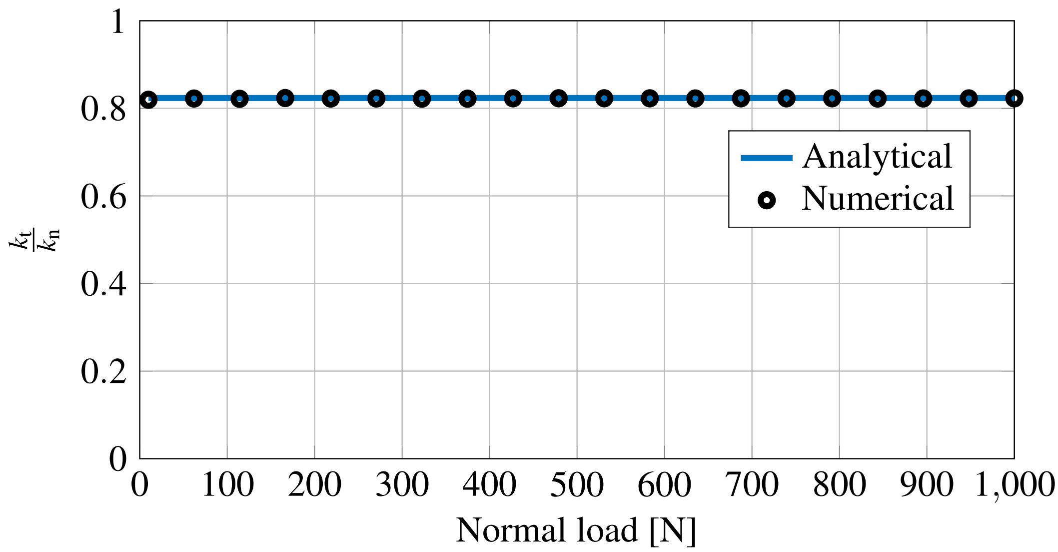

Fig. 5.5 Ratio $k_\mathrm{t}/k_\mathrm{n}$ for different normal loads

5.5 Application to a single bolted joint system with smooth contact interface

The effects of roughness on contact stiffnesses and in turn on the dynamic response will be investigated on a lap joint with a single bolt, depicted in Fig. 5.6, and previously proposed and studied by Süß and Willner [180, 181]. The setup consists of an oscillator which is made of stainless steel and primarily consists of two masses which are connected through a bending spring and a bolted lap joint. As both parts of the structure are monolithic, the only joint in the system is the central bolted joint which can be investigated in an isolated manner.
Before moving to the rough contact analysis results, the model of the resonator system will be described in detail and its nonlinear dynamic response with a smooth contact interface will be presented. The effects of surface roughness will be presented and discussed in section 5.6.

5.5.1 Linear finite element model

A full three-dimensional finite element model (see Fig. 5.6) has been generated in Abaqus with linear hexahedral elements for both masses (19,504 elements) and the bolt (7,830 elements). The bolt is rigidly connected to each mass via “tie constraints” underneath the head of the bolt. Particular care has been taken to refine the matching meshes at the contact interfaces to allow the introduction of a sufficient number of friction elements for the nonlinear dynamic analysis. This fine discretisation of the contact is required to capture local microslip effects which play a critical role in the energy dissipation of the system. All linear components of the system have the same material properties which are a Young’s modulus of 198,400 MPa, a Poisson ratio of 0.3 and a density of 7,949 $\mathrm{kg\,m^{-3}}$ [180, 181].

5.5.2 Nonlinear contact model

In order to observe the nonlinear dynamic behaviour of the studied system, and more precisely the first breathing mode of the leaf spring (with motion occuring only along x direction) depicted in Fig. 5.7, an initial nonlinear dynamic analysis was performed. In this analysis, a number of 3D nonlinear contact elements has been introduced at the contact interface. Each friction element connects a linear finite element node from one side of the contact to its matching node on the opposing side of the contact and transmits the nonlinear forces. A convergence analysis, based on the resulting FRFs, showed that 340 friction elements were sufficient to obtain a converged dynamic response for the mode of interest. This number of friction elements has been used in

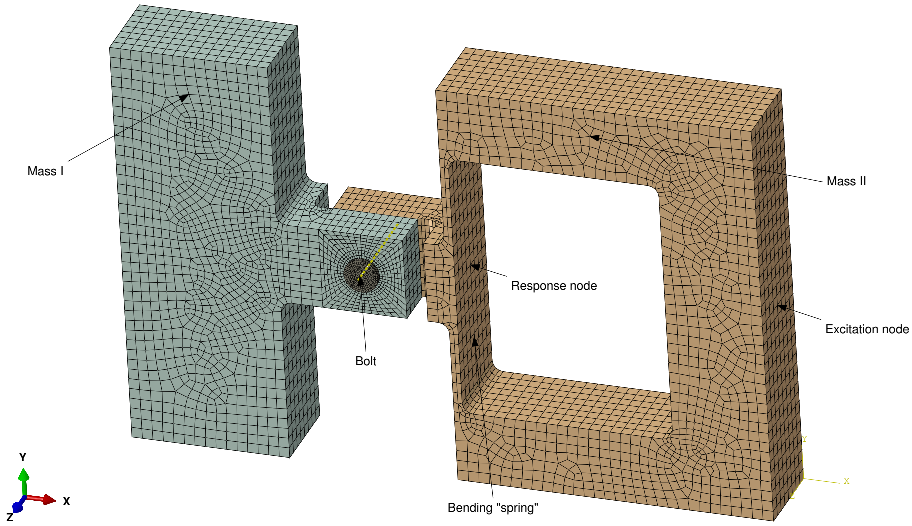

Fig. 5.6 Finite Element model of the resonator

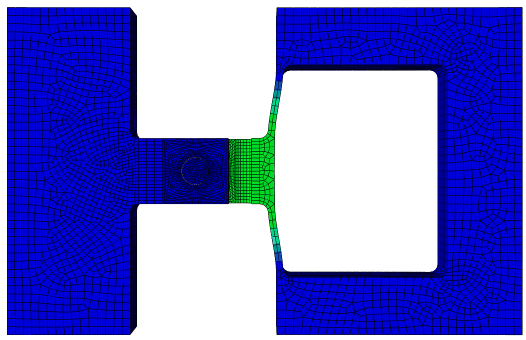

Fig. 5.7 Deformed shape of the first breathing mode of the leaf spring

all subsequent analyses presented here. Similarly, the use of the first three harmonics, plus the harmonic ‘zero’ in the Fourier truncated representation of the response was shown to be sufficient.

For this initial analysis, the contact surface of the joint is supposed to be perfectly flat and smooth. A nonlinear static analysis performed in Abaqus with a 30 kN pretension load of the bolt is providing the normal load required for the definition of each friction element used in the nonlinear dynamic analysis. The pre-tensioning of the bolt is applied by using the ‘bolt load’ feature available in Abaqus. The shaft of the bolt is cut at mid-length through a pre-tension section, and the prescribed force is applied to this section along the axis of the bolt. A surface-to-surface approach with a direct enforcement method (based on Lagrange multipliers) is then used to solve the contact problem. A penalty method formulation with a friction coefficient $\mu = 0.6$ is used to describe the frictional behaviour [180, 181]. The resulting pressure distribution is shown in Fig. 5.8. As expected, the pressure is maximum around the bolt hole and reduces concentrically leading to an area of lower compression on the corners of the contact interface.

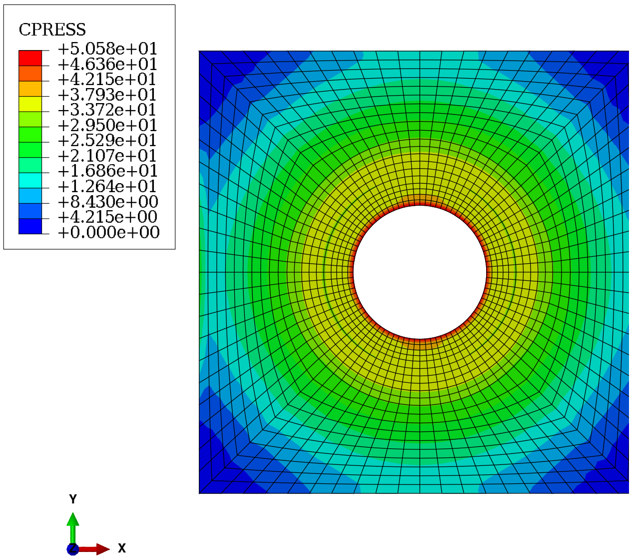

Fig. 5.8 Contact pressure in [MPa] under a 30 kN bolt tightening load

For the baseline modelling approach, the normal and tangential contact stiffnesses of each contact element are set to $6 \times 10^4\,\mathrm{N\,mm^{-3}}$ based on previous measurements reported in [167] to represent the current best practice. For the multiscale approach model, these values are replaced by the ones computed using the BEM-based contact solver, as described in section 5.4. For the initial comparison, only the normal contact stiffnesses were extracted from the contact solver and the tangential contact stiffnesses were assumed to be equal to the normal ones. Figure 5.9 shows the values of normal

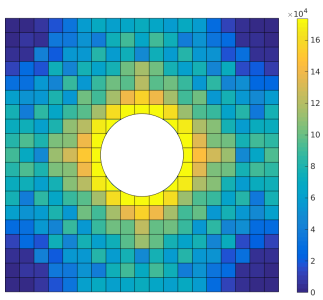

Fig. 5.9 Distribution of normal contact stiffness k_n in $[\mathrm{N\,mm^{-3}}]$

contact stiffness k_n computed using the contact solver (each polygonal area represents one friction element of the nonlinear dynamic model). It can be seen that these values are consistent with the pressures shown in Fig. 5.8: the higher the pressure, the higher the normal contact stiffness. Compared to the uniform value of $6 \times 10^4\,\mathrm{N\,mm^{-3}}$ used in the current modelling approach, the computed values of k_n vary greatly across the contact area between 0 (where there is no contact) and $1.74 \times 10^5\,\mathrm{N\,mm^{-3}}$ around the hole where the pressure is maximum. Interestingly, the average value of k_n is $6.6 \times 10^4\,\mathrm{N\,mm^{-3}}$, which is very close to the measured reference value of $6 \times 10^4\,\mathrm{N\,mm^{-3}}$.

5.5.3 Nonlinear dynamic response: comparison between the current modelling approach and the newly proposed multiscale approach

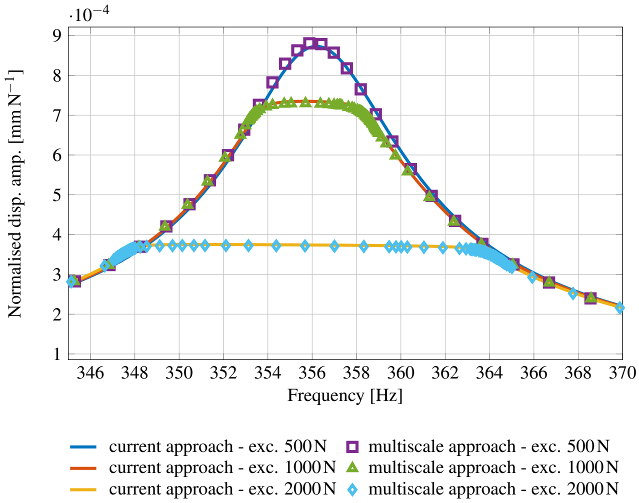

Fig. 5.10 Frequency response functions of the resonator

Figure 5.10 shows the obtained dynamic response under different levels of excitation in the x direction (see Fig. 5.6 which shows the excitation and response nodes location) for the baseline and the updated stiffness model, which illustrates the typical behaviour of a frictional joint: at low excitation level, the joint is fully stuck so its response is linear whereas at higher excitations, some parts of the joint interface start slipping, which leads to a softening effect and an increased damping. The presented results are consistent with the numerical and experimental results of Süß [180, 181]. Figure 5.10 also shows that the newly proposed multiscale approach leads to very similar results to the baseline model with constant contact stiffness across the contact area. This can be probably attributed to the closeness between the baseline and the average multiscale contact stiffness, which leads to a similar stiffness of the entire contact, and therefore to a similar frequency behaviour of the global dynamic response shown in Fig. 5.10.

Figure 5.11 shows the applied pressure on each nonlinear contact element as well as the resulting contact conditions and dissipated energy at resonance under an excitation of 500 N. Similar results are obtained with both methods: in the region underneath

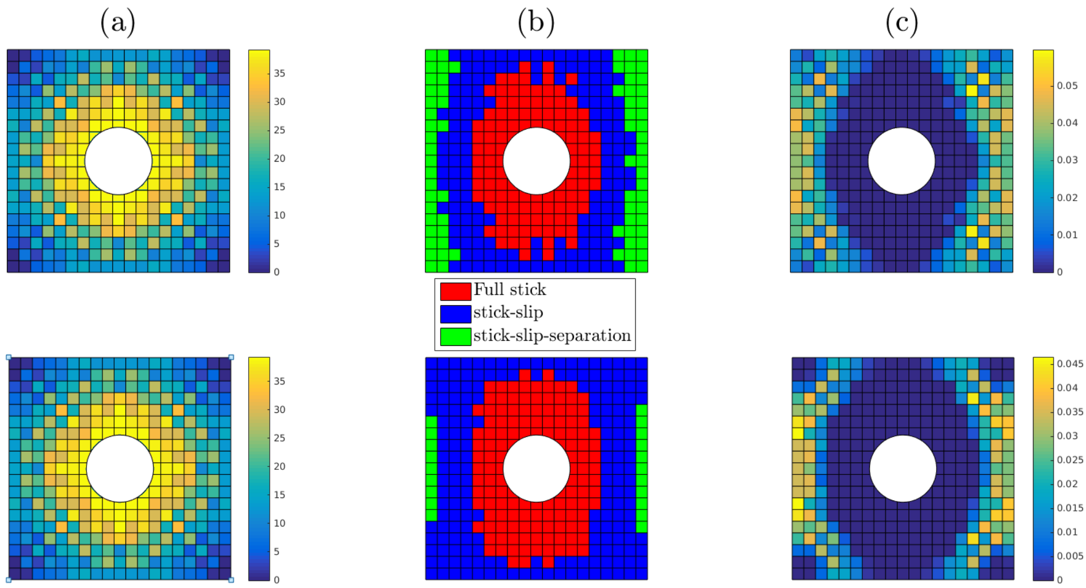

Fig. 5.11 Contact pressure in [MPa] (a), contact conditions (b) and dissipated energy in [mJ] (c) at resonance for the reference (top) and the new model (bottom)

the bolt, the high pressure resulting from the tightening of the bolt prevents relative slip at the contact interface; this part of the joint remains fully stuck and therefore does not dissipate any energy. Outside this area, further away from the bolt, the pressure decreases and relative motion is observed; the nonlinear contact elements experience stick-slip transitions and dissipate frictional energy. Even further away from the bolt, at the edges of the contact area, the much lower pressure allows separation between the two contacting surfaces during a vibration cycle, leading to a mixture of energy dissipation and total loss of contact stiffness.

It is worth noting that despite using the same normal load for each contact element within the two approaches, localised differences can be observed in the contact conditions and dissipated energy. These differences are due to the change of contact stiffness alone, i.e. using an uniform value of contact stiffness across the contact area for the baseline model and values computed for each friction element using the BEM-based contact solver for the newly proposed model. This demonstrates the potential of the proposed multiscale approach to capture the localised contact conditions accurately which is particularly important for future wear predictions or joint contact optimisation.

5.6 Study of the effects of roughness on the nonlinear dynamic response

5.6.1 Comparison between smooth and rough contact

To investigate the effect of surface roughness, different surface finishes have been generated, where the RMS roughness was kept between 0.025 μm and 50 μm, as given in ISO 1302. All these rough surfaces have been generated using 256×256 points. As a result, the analyses performed in the contact solver on the entire contact surface were done using a regular grid of 256×256 elements. A finer meshing of the surface in the contact solver would not increase the accuracy but instead would amplify the boundary effects at the edges of the contact area. Figure 5.12 shows one of the simulated rough profiles and the resulting contact morphology under a 30 kN normal load.

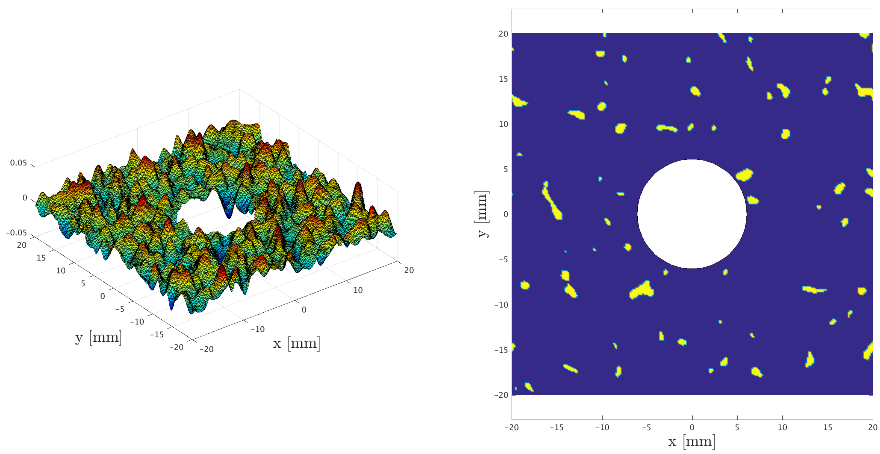

Fig. 5.12 Profile heights [mm] (left) and morphology of the contact under a 30 kN normal load (right)

The heights of the profile follow a Gaussian distribution with a root-mean-square (RMS) roughness $R_q = 10\,\mu\text{m}$ and a correlation lengths of 0.5 mm in both x and y directions. The heights of the profile have been magnified in Fig. 5.12 to allow the visualisation of the roughness. As can be seen on the right part of that figure, the real contact area is significantly reduced compared to the smooth surface and represents only 2.7% of the total potential contact area. This results in a completely different pressure distribution now consisting in local peaks of much high pressure. The computed local pressure ranges from 0 to 568 MPa. Depending on the material properties, these values may lead to plastic deformation. The compressive yield strength of a stainless steel typically varies between 170 and 310 MPa while that of a maraging steel can be as high as 1200 MPa. As a result, for an even more accurate analysis and to extend the range of application of the proposed approach, plasticity should be considered. The effects of plasticity, which are ignored here, will be investigated in the next chapter.

In order to evaluate the effect of the localised pressure distribution on the dynamic response, initially a nonlinear dynamic analysis was performed using the new pressure distribution only, but keeping the reference values of contact stiffness, i.e. $k_\mathrm{n} = k_\mathrm{t} = 6 \times 10^4\,\mathrm{N\,mm^{-3}}$ for all nonlinear contact elements constant. In a next step, the normal contact stiffnesses were computed with the contact solver, and proportional values of tangential contact stiffnesses obtained from Eq. 5.9 were used. Finally, the values of k_n and k_t, computed from the contact solver were used to consider all relevant effects for the dynamic response of the system. These three configurations will be referred to respectively as 'multiscale v1', 'multiscale v2' and 'multiscale v3' (see Tab. 5.2).

	Normal load	k_n	k_t
baseline approach	from Abaqus	$6 \times 10^4\,\mathrm{N\,mm^{-3}}$	$6 \times 10^4\,\mathrm{N\,mm^{-3}}$
multiscale v1	from contact solver	$6 \times 10^4\,\mathrm{N\,mm^{-3}}$	$6 \times 10^4\,\mathrm{N\,mm^{-3}}$
multiscale v2	from contact solver	from contact solver	$\frac{2(1-\nu)}{(2-\nu)} k_\mathrm{n}$
multiscale v3	from contact solver	from contact solver	from contact solver

Table 5.2 Contact parameters for all tested configurations

The resulting distributions of stiffness computed by the contact solver are shown in Fig. 5.13. Fig. 5.13a) shows the normal contact stiffness used in the configurations 'multiscale v2' and 'multiscale v3'. Fig. 5.13b) is the tangential contact stiffness, proportional to the computed values of k_n, according to Eq. 5.9 and used in 'multiscale v2'. Finally, Fig. 5.13c) shows the computed tangential stiffness from the contact solver, used in 'multiscale v3'. As expected, the computed values of stiffness vary greatly across the contact area, in line with the non-uniform pressure distribution shown in Fig. 5.12.

In order to quantify the effects of the computed contact stiffnesses on the global dynamic response, an equivalent value was calculated for each configuration, representing an average value of stiffness between all nonlinear contact elements. It can be seen in Fig. 5.14 that despite using the reference value of $6 \times 10^4\,\mathrm{N\,mm^{-3}}$ in 'multiscale v1', a significant drop in global joint stiffness occurs, since the roughness reduces the real contact area so that fewer nonlinear contact elements actually come into contact during the dynamic analysis. A further drop of the global joint stiffness is observed for the configurations 'multiscale v2' and 'multiscale v3'. This is due to the fact that all local contact stiffnesses computed by the contact solver are below $4.5 \times 10^4\,\mathrm{N\,mm^{-3}}$ which is lower than the baseline value of $6 \times 10^4\,\mathrm{N\,mm^{-3}}$. Interestingly, using the Mindlin analytical solution for the tangential contact stiffness (see Eq. 5.9) yields

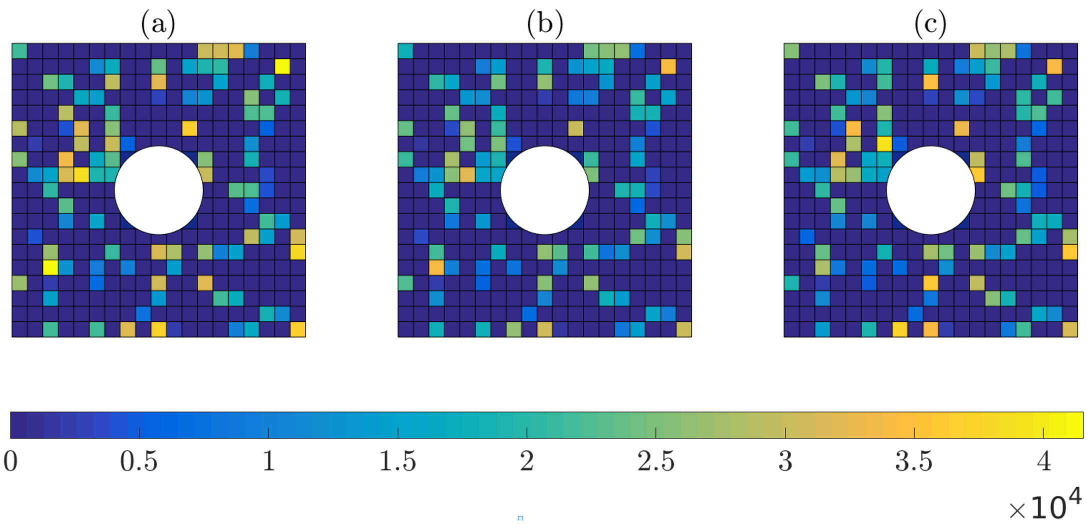

Fig. 5.13 (a) Computed normal contact stiffness k_n in [N mm^{-3}], (b) Mindlin tangential contact stiffness k_t in [N mm^{-3}] and (c) computed k_t in [N mm^{-3}]

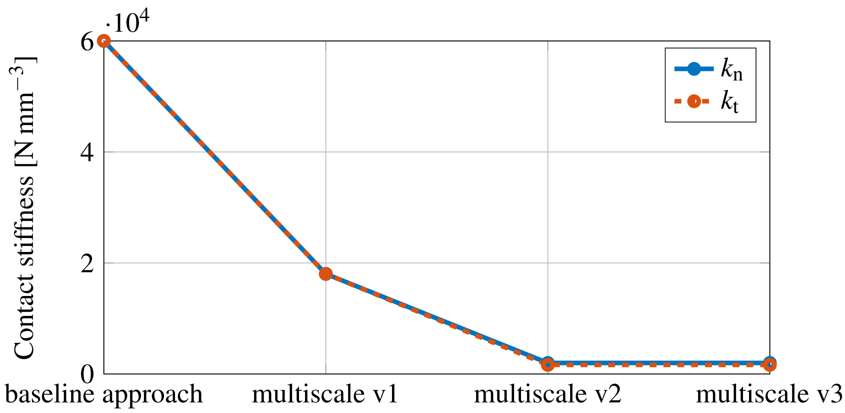

Fig. 5.14 Equivalent normal and tangential contact stiffness for all tested configurations

almost the same equivalent global tangential stiffness than that obtained using the contact solver values. This means that in this particular case, Mindlin theory is providing a good average value of the tangential contact stiffness. However, some discrepancies can be observed locally in Fig. 5.13 which justifies the need to use the contact solver for an accurate evaluation of the local contact conditions.

The nonlinear dynamic response for the 1st breathing mode of the oscillator for each of the above mentioned joint models was computed at three different excitation levels (500 N, 1,000 N, 2,000 N), and the results are shown in Fig. 5.15. The changes of contact stiffness between the multiscale approaches v1 , v2 and v3 do not result in significant changes of the global dynamic response which is in line with their relatively similar averaged values from Fig. 5.14. It is interesting to notice, that the baseline approach with a much higher contact stiffness still leads to only marginally stiffer resonance frequencies, indicating that this particular joint geometry is relatively robust with regards to contact stiffness variations. All multiscale approaches tend to

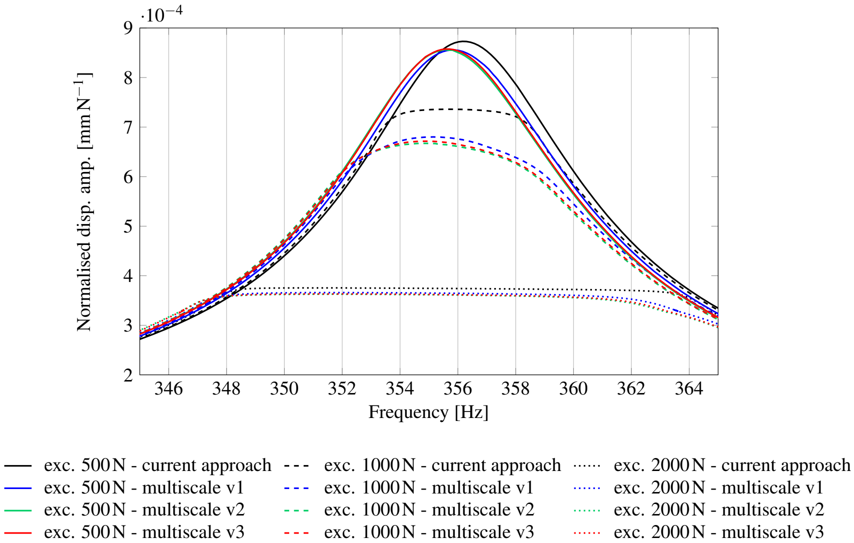

Fig. 5.15 Frequency response functions of the resonator for different contact parameter setups

increase the energy dissipation in the contact, leading to a reduction in amplitude, but only the 1,000 N case shows a significant change. This is reflected in the local contact conditions and frictional dissipated energy at resonance in Fig. 5.16, where a very different picture emerges for the multiscale approach when compared to the baseline model. The originally clearly identifiable zones of stick, slip and separation

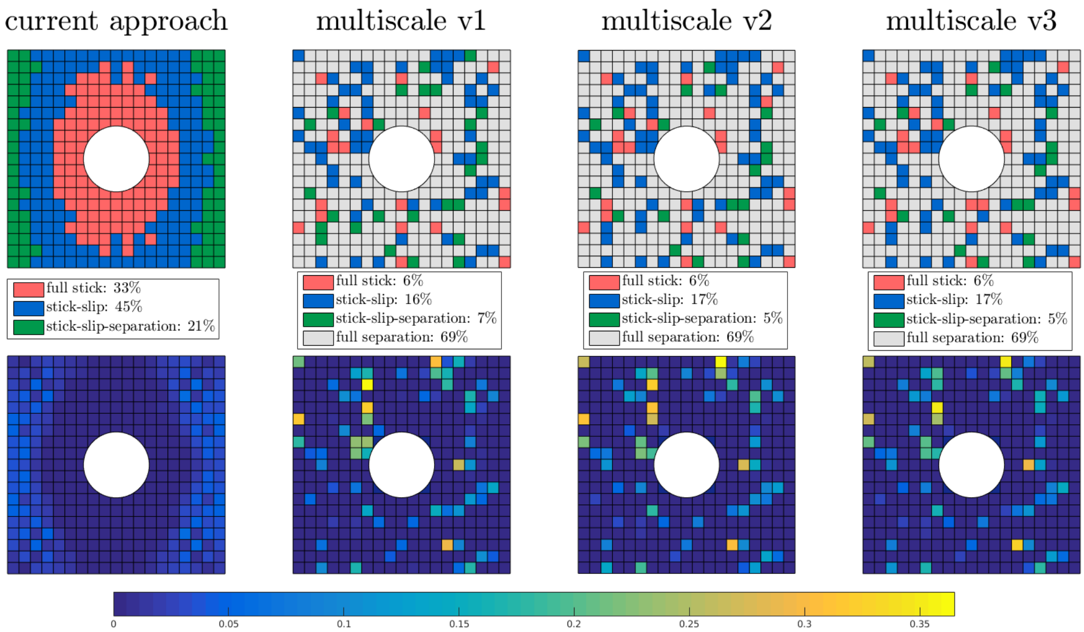

Fig. 5.16 Contact conditions (top) and frictional dissipated energy distribution mJ (bottom) at resonance under a 500 N excitation

have entirely disappeared, with all contact conditions now distributed over the entire contact zone. Although a reduced number of nonlinear elements is undergoing stick-slip transitions for the multiscale models the tangential relative motion between the contacting surfaces is much larger, which in turn leads to a larger frictional energy dissipation in certain hotspots (see bottom row of Fig. 5.16). To further demonstrate this increase in energy dissipation, the global hysteresis loop of a single vibration cycle for all four configurations has been plotted in Fig. 5.17, showing the significantly larger displacements and enclosed area of the multiscale approach.

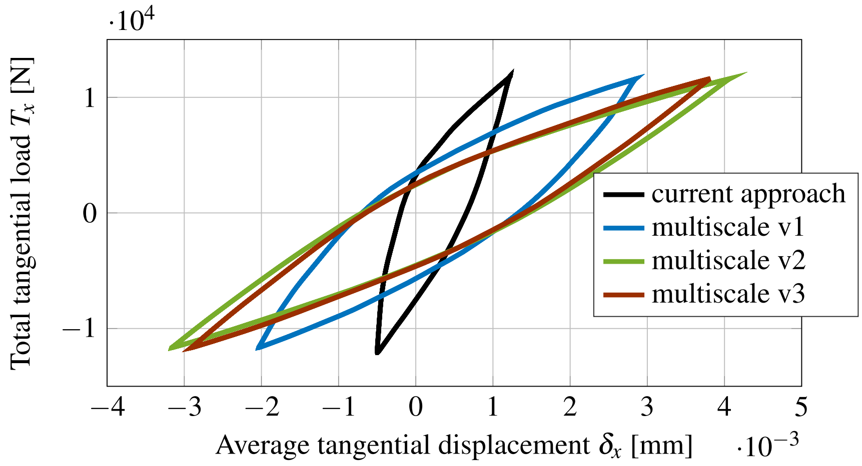

Fig. 5.17 Frictional hysteresis loops at resonance under a 500 [N] excitation

5.6.2 Effects of R_q on the nonlinear dynamic response

To understand the effects of different roughness values on the contact stiffness and in turn on the nonlinear dynamic response, four different surfaces with a root-mean-square roughness R_q of 1 µm, 5 µm, 10 µm and 15 µm and correlation lengths $cl_x = cl_y = 0.5$ mm were generated. Figure 5.18 shows the resulting morphology of the contact where it can be seen that as R_q increases, the fractional real area of contact decreases from 22.1% to 2.0%.

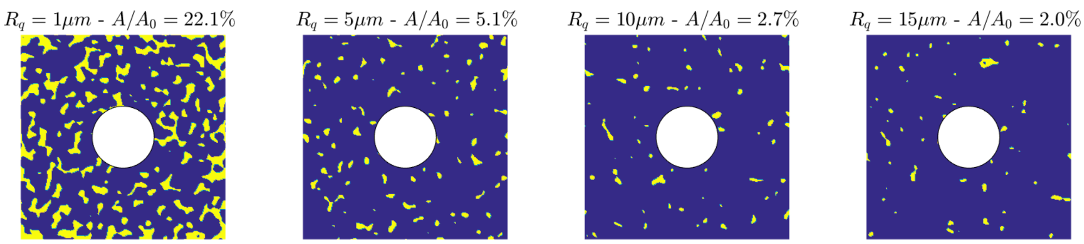

Fig. 5.18 Morphology of the contact under a 30 kN normal load for different values of RMS roughness

With regards to the resulting stiffness (computed following multiscale v3), as R_q increases the real contact area decreases, leading to an increase of the local pressures and therefore to an increase of the corresponding local contact stiffnesses from the contact solver. Interestingly, Fig. 5.19 shows that the equivalent stiffness of the joint decreases for higher values of R_q, which can be attributed to the fact that the loss of contact stiffness due to the decrease of the real contact area has a much stronger impact on the global stiffness than the increase of some local contact stiffness due to higher pressure.

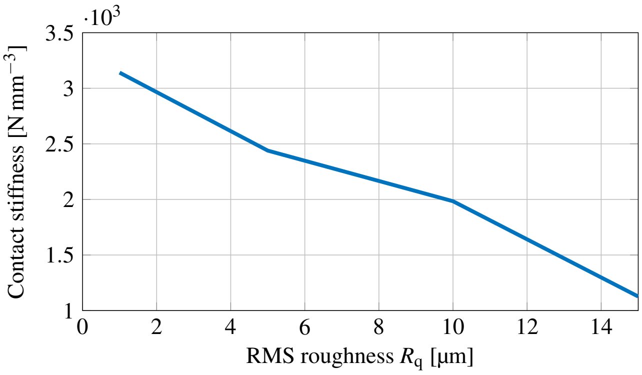

Fig. 5.19 Global contact stiffness for different values of R_q

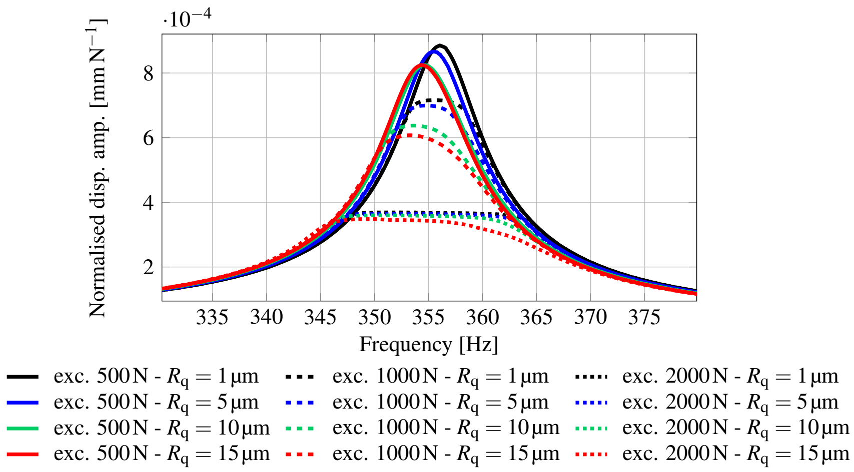

Fig. 5.20 Frequency response functions of the resonator for different values of R_q

The effect of the roughness values on the nonlinear frequency response can be seen in Figure 5.20 for the four different profiles and for three different excitation levels, 500 N, 1,000 N and 2,000 N. The same dependency on the R_q values can be observed for all three excitation levels: the higher R_q, the lower the resonance frequency and the higher the energy dissipation. The drop in frequency is in line with the reduction in global stiffness at higher R_q values observed in Fig. 5.19, while the change in energy dissipation can be explained with Fig. 5.21. It shows that for higher values of R_q, the same tangential load T_x leads to higher relative tangential motions. As a result, although there are less and less contact elements dissipating energy, the total frictional dissipated energy, which is equal to the area of the presented hysteresis loops, increases with R_q, leading to a more damped frequency response function.

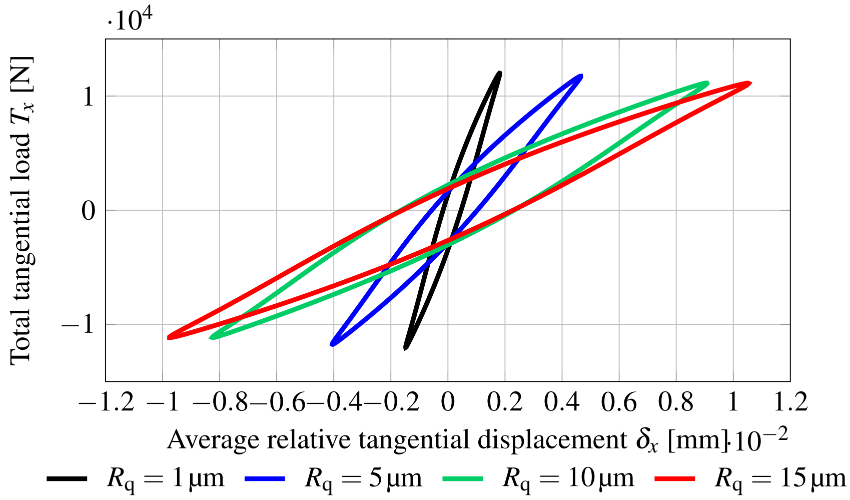

Fig. 5.21 Frictional hysteresis loops at resonance for different values of R_q under 500 N excitation

5.7 Discussions

The proposed approach permitted to evaluate the influence of roughness on the non-linear dynamic response of a friction joint. It was shown that the surface roughness has a very strong impact on the contact conditions that are the pressure distribution and the normal and tangential contact stiffness. Roughness reduces drastically the real contact area, which leads to a fundamentally different contact pressure than that of a smooth surface; very localised peaks of pressure appear and lead to higher values of local normal contact stiffness. At the same time, the decrease of the real contact area leads to fewer active friction elements and therefore to a decrease of the global stiffness of the joint. This last mechanism was shown to have a stronger impact than the increase of local contact stiffness since the global stiffness of the joint was observed to decrease with roughness. The same observations were made on the tangential contact stiffness. It was also observed that the Mindlin analytical solution was providing a good average value of the tangential contact stiffness, so it could potentially be used to save computational time if only the global dynamic behaviour of the joint is of interest. By plotting the frequency response functions of the first breathing mode of the joint, it was shown that the newly proposed approach only led to small variations of resonance frequency and energy dissipation. However, this does not mean that the baseline approach should not evolve since the small differences can be explained by the fact that the computed global joint stiffness, which drives the frequency response function that represents the global behaviour of the joint, happened to be close to the reference value of $6 \times 10^4\,\mathrm{N\,mm^{-3}}$, which could be different for another application. Furthermore, larger differences between the baseline approach and the newly proposed approach were observed on the local contact conditions and in particular completely different energy dissipation mechanisms were observed with the new approach. These local phenomena resulting from surface roughness, which are critical if it is intended to optimise the joint design or to predict wear, can only be captured with the proposed approach. It is worth reminding that for even more accurate evaluation of the contact conditions with regards to roughness, plasticity should be considered.

5.8 Conclusions

In this chapter, a refinement of the multiscale approach was introduced to evaluate the effects of surface roughness on the nonlinear dynamic response of a bolted joint. In this approach, four out of the five parameters of the nonlinear friction elements are computed using the BEM-based contact solver, which allows to include the strong effects of surface roughness on contact stiffness.

The presented results highlight the sensitivity of the nonlinear dynamic response to changes at the contact interface; the surface roughness reduces drastically the real contact area, which leads to a complete redistribution of the contact pressure and to a strongly non-uniform distribution of contact stiffness. It could be shown that for low values of RMS roughness (below $5\,\mu\mathrm{m}$), the effects of the roughness on the global nonlinear dynamic response is small enough to be neglected in the analysis and even for larger values the global effect is relatively small and smeared values can provide a reasonably good prediction.

However, if it is intended to obtain accurate local contact predictions in order to optimise the joint design to maximize energy dissipation or to predict wear, then the effects of roughness must be considered in the analysis. For higher values of RMS roughness, both the global and local behaviour of the joint are significantly affected.

Chapter 6

Fretting wear analysis of a bolted lap joint with rough contact interface

6.1 Introduction

In the previous chapter, a single bolted joint system was used to study the effects of roughness on the nonlinear dynamics of the system. In this chapter, the same system is being used to investigate the effects of surface roughness on fretting wear and in turn on the nonlinear dynamics of the system over time. Three of the four surfaces used previously have been kept. The surface with an initial root mean square (rms) roughness of 15 μm has been replaced by one with an initial rms roughness of 0.5 μm in order to have one surface representing of a fine finishing process. Therefore, the four considered surfaces now have an initial rms roughness of 0.5, 1.0, 5.0 and 10 μm.

6.2 Fretting wear analyses

Fretting wear simulations have been run for each surface profile, up to 10 millions vibration cycles, which was shown to be enough to reach a steady state. Fretting wear is having cascading effects on (a) the contact surface geometry, (b) the contact conditions and (c) the nonlinear dynamic response, as will be shown hereafter. Owing to the fact that a similar behaviour was observed for all profiles, and to improve clarity, most of the results presented here are the ones associated with the profile having an initial rms roughness of 5 μm.

6.2.1 Input parameters

Wear parameters

As described in Chapter 4, the wear simulations are controlled by two parameters. The first one is the wear coefficient α that links the volume of wear to the frictional dissipated energy (see Eq. 4.4). The same coefficient as the one used in Chapter 4, equal to $2 \times 10^3\,\mu m^3\,J^{-1}$, will be used again here.

The second parameter is the maximum allowed local wear depth per iteration. Its value must be small enough to ensure the stability of the wear scheme and at the same time as large as possible to speed up the computations. A value of 0.01 µm was found to be optimal for the profiles with an initial rms roughness of 0.5 and 1 µm. A value of 0.1 µm has been used for the two other profiles. This second parameter leads to the use of an acceleration factor, which is the number of fretting cycles that can be accumulated before the maximum allowed local wear depth is attained, at which point the surface profile is updated and the refined contact analysis is performed again.

Loading conditions

The other input data which are necessary for the contact analysis and the wear simulations are the normal and tangential loads applied to the contact interface. These loads are extracted from the frequency response functions (FRFs) at resonance. The initial FRFs corresponding to each unworn rough surface under a 1,000 N excitation are shown in Fig. 6.1.

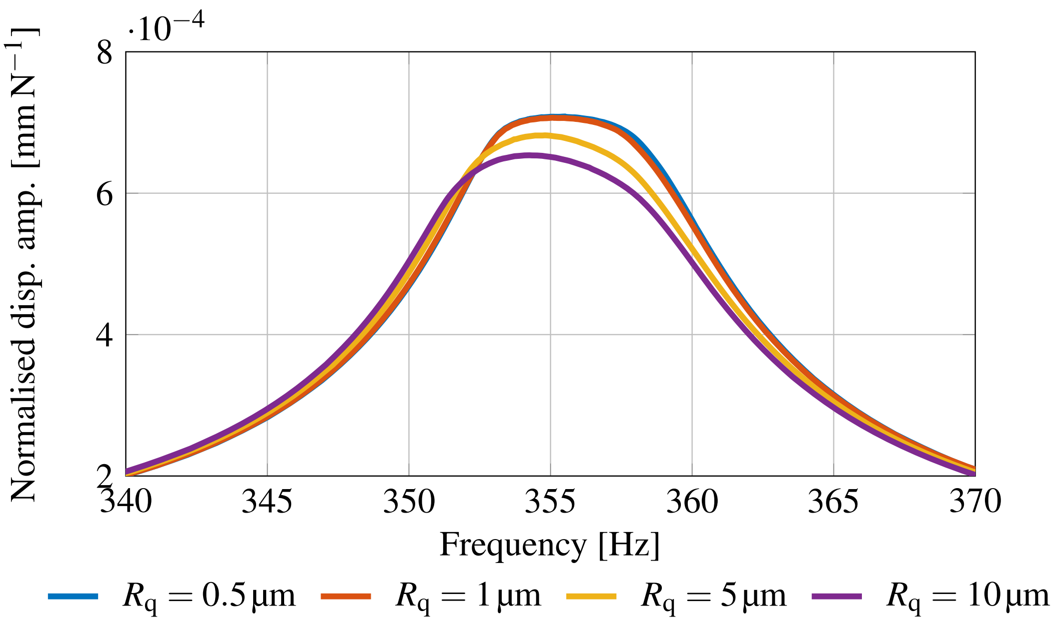

Fig. 6.1 Initial FRFs for different initial rms roughness

The necessary inputs for the contact analysis are the contact loads and displacements at resonance. More precisely, the input of the normal problem is the summation of the normal forces at each nonlinear friction element. The bending moments were shown to be negligible. The tangential problem simulations are displacement-controlled to allow macro-slip. The necessary input is therefore the average of the tangential relative motions over the contact interface. Before proceeding to the required summation and averaging, the data are converted from the frequency domain into the time domain using an inverse Discrete Fourier Transform. The resulting loadings, corresponding to each surface profile, are given in Fig. 6.2. As discussed in the

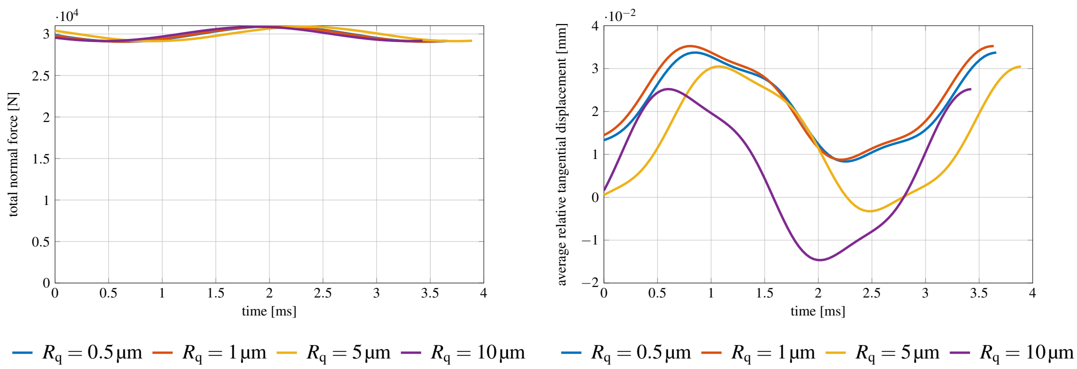

Fig. 6.2 (a) Total normal force [N] and (b) average tangential relative displacement [mm]

previous chapter, the higher the roughness, the larger the relative tangential displacement and therefore the higher energy dissipation. As for the normal contact, it was shown in the previous chapter that significant changes are observed in the local normal force depending on roughness. Despite these local differences, not much difference is observed on the total normal force transmitted through the contact interface of the joint.

Using the input parameters described in this section, fretting wear simulations were run on each surface up to 10 million cycles at resonance frequency, without any update of the nonlinear dynamic model along the way. The effects of wear on the contact surface geometry and on the contact conditions are discussed in the next two sections.

6.2.2 Effects of wear on the contact surface geometry

The first effect of wear is the change of the contacting surface geometry. Figure 6.3 shows the total wear depth obtained after $10,041,928$ cycles for the profile having an initial rms roughness of $5\,\mu\text{m}$. The wear simulations were run using one CPU of an Intel Core i7-4700HQ 2.40GHz. Each fretting cycle took approximately 70s to run, but thanks to the acceleration factor, only 231 iterations were needed to reach 10 million cycles, which took approximately 4h29min. Figure 6.4 shows the evolution of the surface profile with wear along the blue line drawn in Fig. 6.3. It can be observed

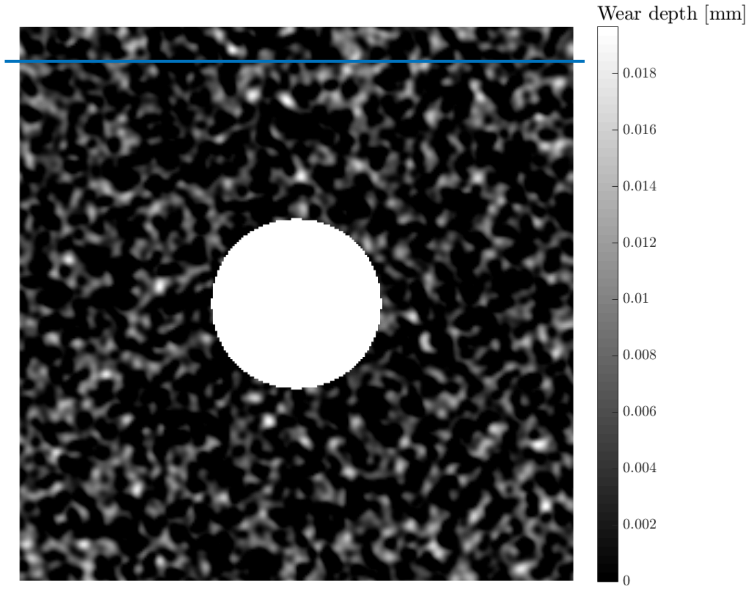

Fig. 6.3 Cumulated wear depth in [mm] after 10,041,928 cycles

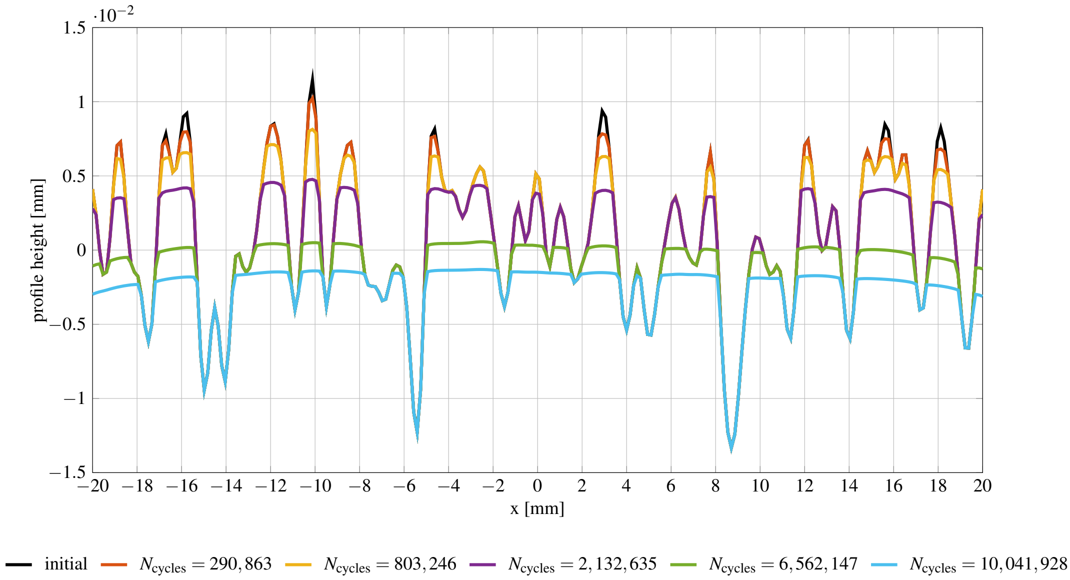

Fig. 6.4 Evolution of surface profile with wear

that the roughness is progressively being removed by fretting wear.

Due to that change of geometry, the roughness parameters of the surface are also affected, including its skewness and kurtosis, so that after only a few wear cycles, the four Gaussian rough surfaces used here are no longer Gaussian. In order to better describe the evolution of each surface, two additional roughness parameters, which are the skewness and kurtosis, will be used here as well. Skewness tells whether the shape of the surface height distribution is symmetric or skewed to one side. Its value can be computed using the following formula:

$$Sk = \frac{m_3}{m_2^{3/2}}, \tag{6.1}$$

where $m_3 = \frac{1}{n}\sum(h-\bar{h})^3$ and $m_2 = \frac{1}{n}\sum(h-\bar{h})^2$.
$\bar{h}$ is the mean of the heights and n is the number of points. m_3 is called the third moment of the data and m_2 is the variance, i.e. the square of the standard deviation. The distribution of height of a Gaussian surface being perfectly symmetric, its skewness is equal to 0.

The second parameter used to describe a non-Gaussian surface is the kurtosis which characterises the sharpness of the central peak of the height distribution. Higher values of kurtosis indicate a higher and sharper central peak. Lower values indicate a lower and less distinct peak, as shown in Fig. 6.5. Kurtosis is linked to the fourth moment of the data m_4 via the following expression:

$$Ku = \frac{m_4}{m_2^2}, \tag{6.2}$$

where $m_4 = \frac{1}{n}\sum(h-\bar{h})^4$.
A Gaussian rough surface has a kurtosis equal to 3.
The evolution of the mean height, the rms roughness, the skewness and the kurtosis of

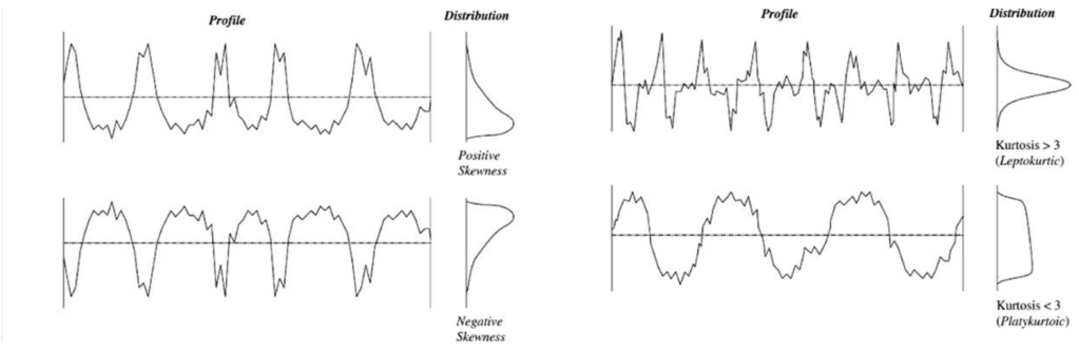

Fig. 6.5 Rough profiles with different skewness and kurtosis values [75]

the surface with wear is shown in Fig. 6.6. It can be seen that all roughness parameters of the surface are strongly affected by wear. As the surface wears out, its rms roughness decreases. The couple skewness-kurtosis starts from (0,3) which is characteristic of a Gaussian rough surface, to different values, which shows that the surface is no longer Gaussian. The evolution of the skewness indicates that the distribution of heights

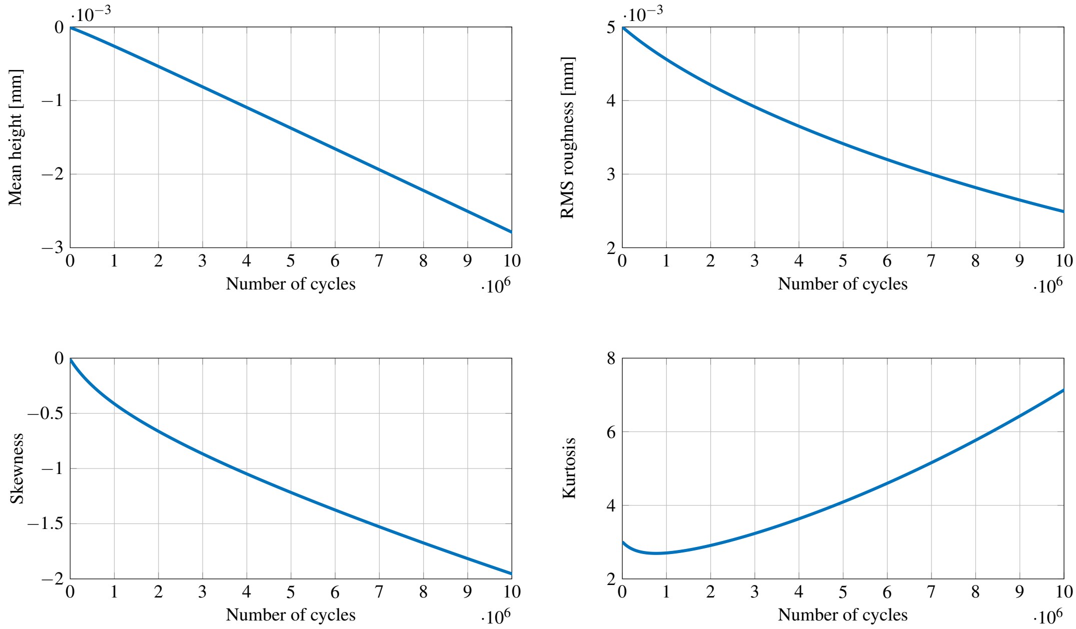

Fig. 6.6 Evolution of (a) mean height, (b) RMS roughness, (c) Skewness and (d) Kurtosis with wear

becomes negatively skewed as the surface wears out. Conversely, the kurtosis is increasing with wear.

6.2.3 Effects of wear on the contact conditions

The changes of contact geometry affect the contact conditions. The evolution of the contact pressure with wear is shown in Fig. 6.7. As the surface wears out, the asperities are progressively removed, the contact area increases (as shown in Fig. 6.8) and consequently, the peaks of pressure are decreasing until nearly flat patches of much lower pressure are obtained.

Wear is also affecting another key parameter for the nonlinear dynamic analysis which is the contact stiffness. Figure 6.9 shows the evolution of the global normal contact stiffness for each rough profile. Two distinct phases can be observed: a running-in phase during which the contact stiffness rapidly increases and a steady phase during which it keeps increasing, but at a much lower rate. During the running-in phase, there is an increasing number of asperities that come into contact which leads to more and more peaks of pressure which are associated with high values of contact stiffness. Then, as the peaks are progressively turning into larger patches of much lower pressure, the local values of contact stiffness are decreasing, but the overall contact stiffness keeps increasing because the global contact area does so. The results also seem to indicate that the global contact stiffness tends to the same value no matter

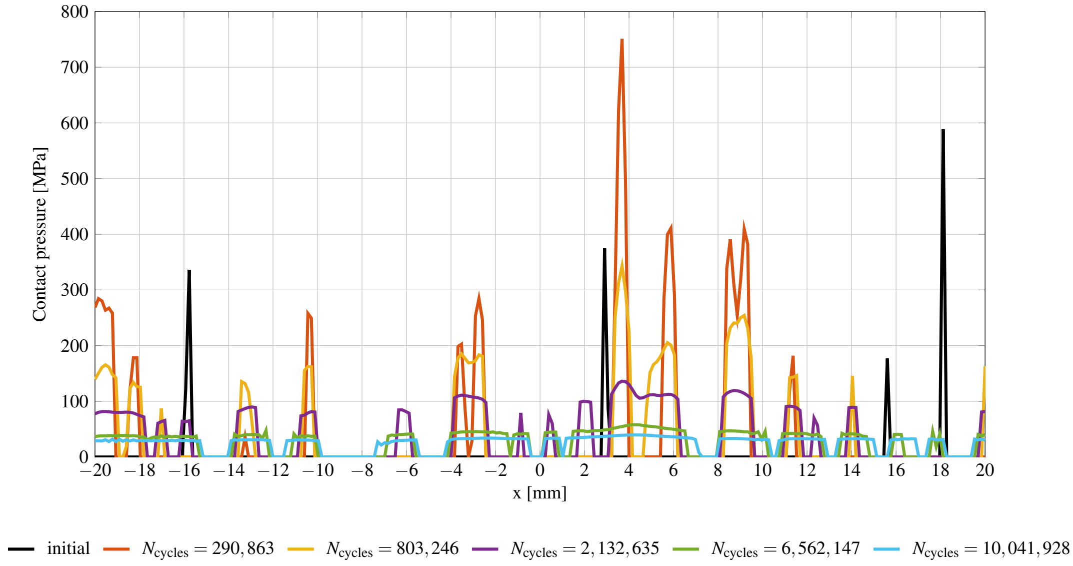

Fig. 6.7 Evolution of contact pressure with wear

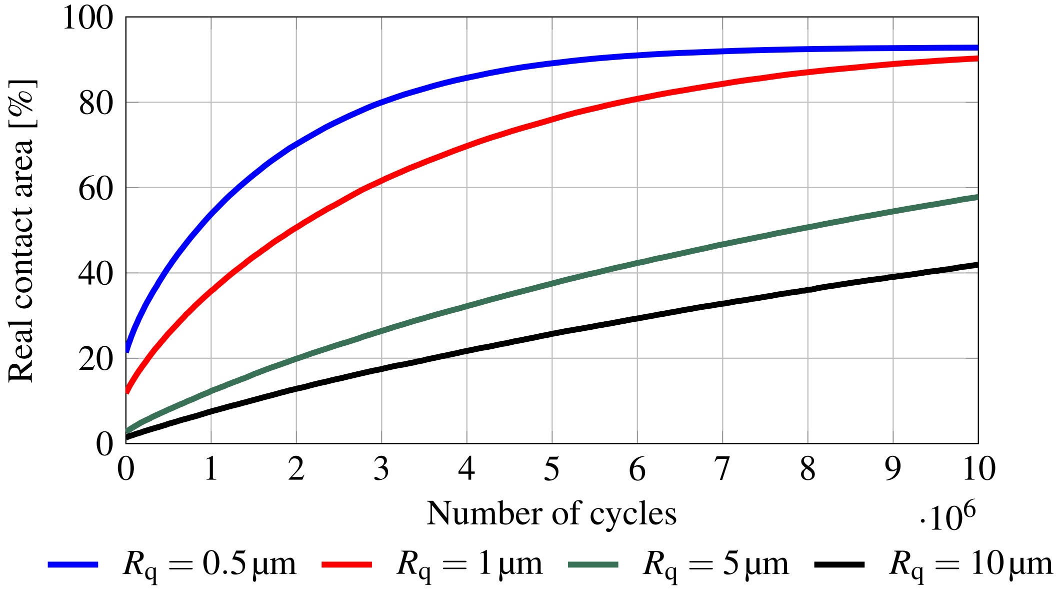

Fig. 6.8 Evolution of contact area with wear

what the initial rms roughness is. The same observations can be made on the global tangential contact stiffness, which is plotted in Fig. 6.10.

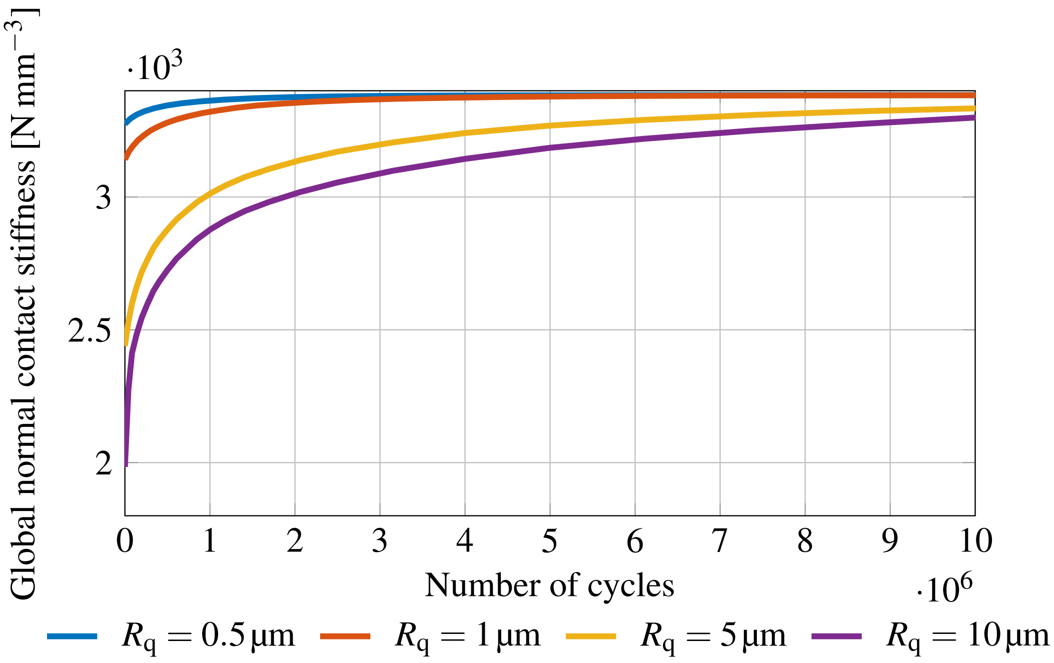

Fig. 6.9 Evolution of global normal contact stiffness with wear

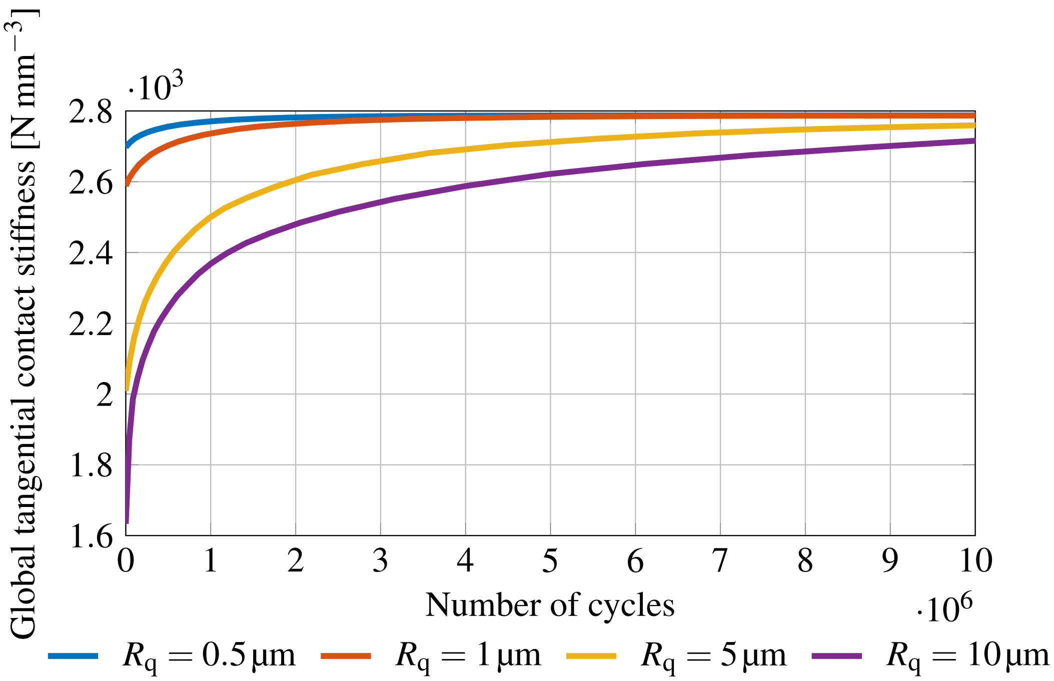

Fig. 6.10 Evolution of global tangential contact stiffness with wear

6.2.4 Effects of wear on the nonlinear dynamics

Criterion for the update of the nonlinear dynamic model

To generate the results presented in the previous section, the inputs parameters that are the loading conditions of the contact interface have been kept the same over time.

In other words, the coupling between fretting wear and nonlinear dynamics has been neglected. Considering the strong variations of contact pressure and contact stiffness with wear, the nonlinear dynamic behaviour is likely to be affected too.
The nonlinear dynamic response depends on the local values of normal load, normal and tangential contact stiffness which drive the stick-slip phenomena taking place at the contact interface. However, in order to have one parameter usable as a criterion for the update of the nonlinear dynamic model, the global contact stiffness was chosen, leading to the following criterion: the nonlinear dynamic model, and more precisely the parameters of the friction elements which are the normal load, the gap and contact stiffness, should be updated after a certain variation of the global contact stiffness is obtained in the wear simulations. The value of that variation depends on the system and the sensitivity of its dynamic behaviour to changes of contact conditions. For the present system, three values of 5%, 10% and 20%, chosen arbitrarily, have been tested.

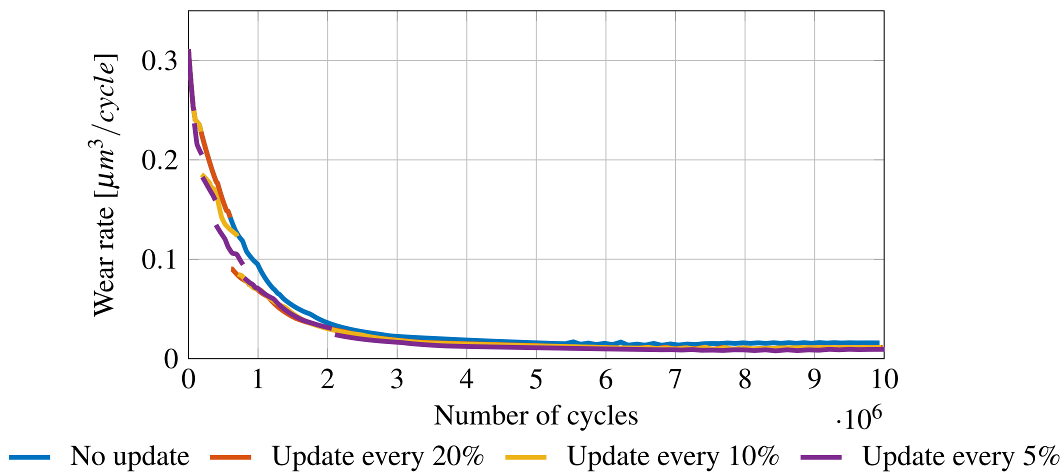

Fig. 6.11 Evolution of the wear rate for different update criteria

Figure 6.11 shows the evolution of the wear rate for different update criteria of the nonlinear dynamic model. First of all, similar to the observations made on the contact stiffness, a running-phase and a steady phase can be observed. Secondly, a jump in the wear rate is obtained after every update of the nonlinear dynamic model. This can be explained by the fact that the increase of contact stiffness with wear leads to smaller tangential relative displacements at the contact interface and therefore to a lower energy dissipation and a lower wear rate. The influence of the update is noticeable in the running-in phase during which the largest differences can be observed between the blue curve and the others. But these differences nearly vanish during the steady state wear: after only one million cycles, the three update criteria are yielding to nearly the same wear rate.

Figure 6.12 depicts the evolution of the contact stiffness for the different update criteria. As can be seen, the global contact stiffness is barely affected by the updates, and all of them are yielding to nearly the same stiffness during all simulated cycles. Based on these observations, the nonlinear dynamic response after these 10 million cycles is expected to be the same for all update criteria, which is confirmed by Fig. 6.13.

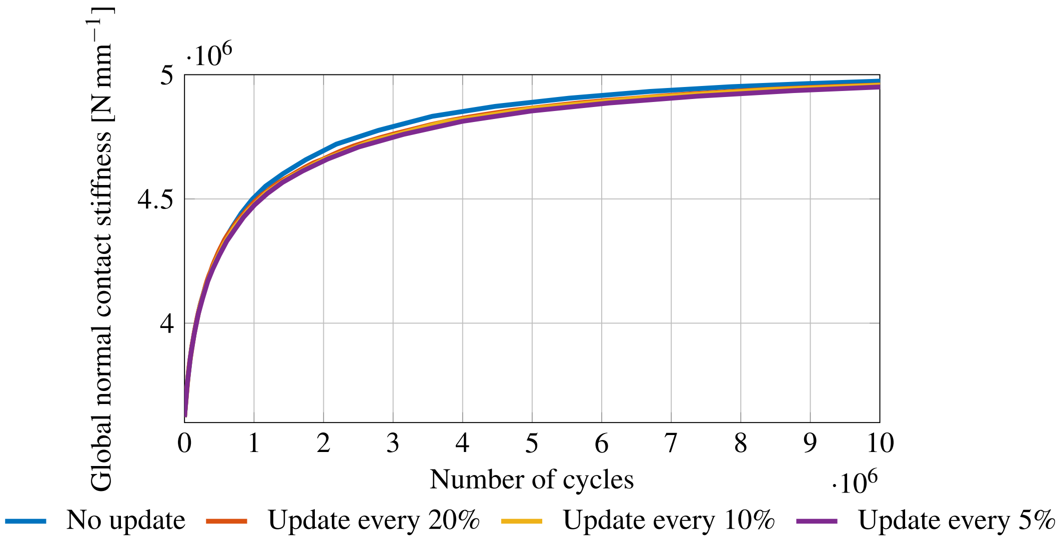

Fig. 6.12 Evolution of global normal contact stiffness with wear for different update criteria

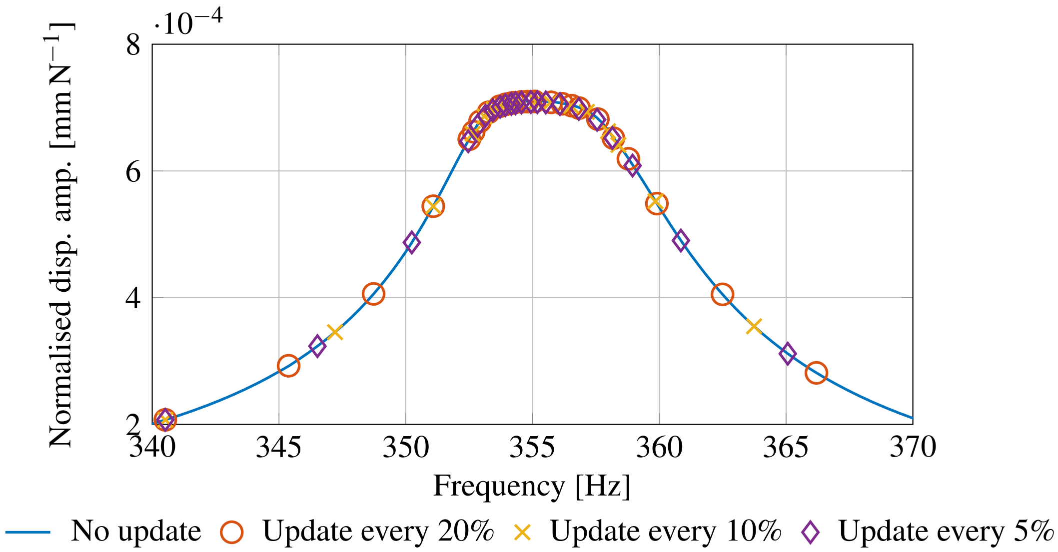

Fig. 6.13 FRFs after 10 million cycles for different update criteria

As a result, for this particular application, no update of the nonlinear dynamic model is needed to discuss the effects of roughness and wear on the dynamic response up to 10 million cycles. For that reason, all subsequent presented results have been obtained without updating the nonlinear dynamic model.

Effects of wear on the nonlinear dynamics

The changes of the dynamic response with wear are given in Fig. 6.14. The analysis which was done in the previous chapter can be transposed here: due to wear, the surface roughness is decreasing. This loss of roughness results in a global stiffening of the contact interface and thus to a shift of the resonance frequency to the higher frequencies, and in a lower energy dissipation which means higher amplitude of the frequency response function. These effects are further illustrated by Fig. 6.15 which shows the corresponding hysteresis loops for the full contact.

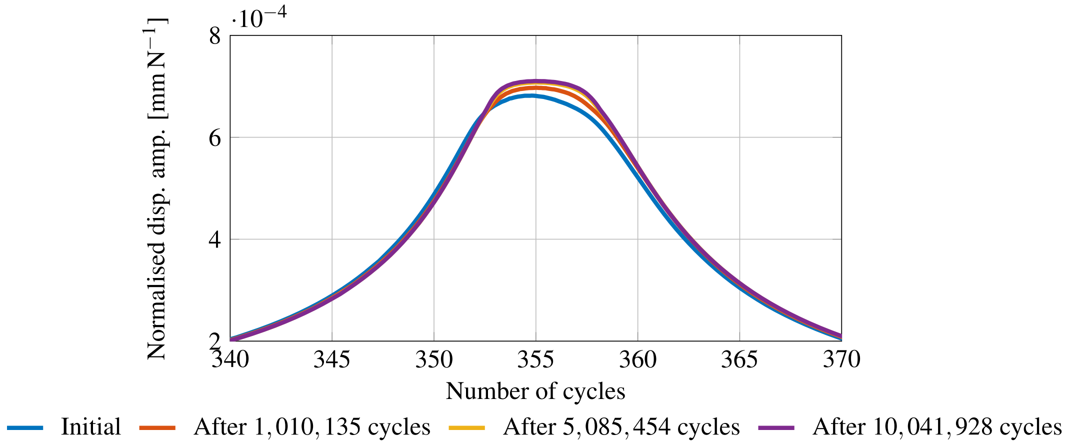

Fig. 6.14 Evolution of FRFs with wear for $R_q = 5\,\mu m$

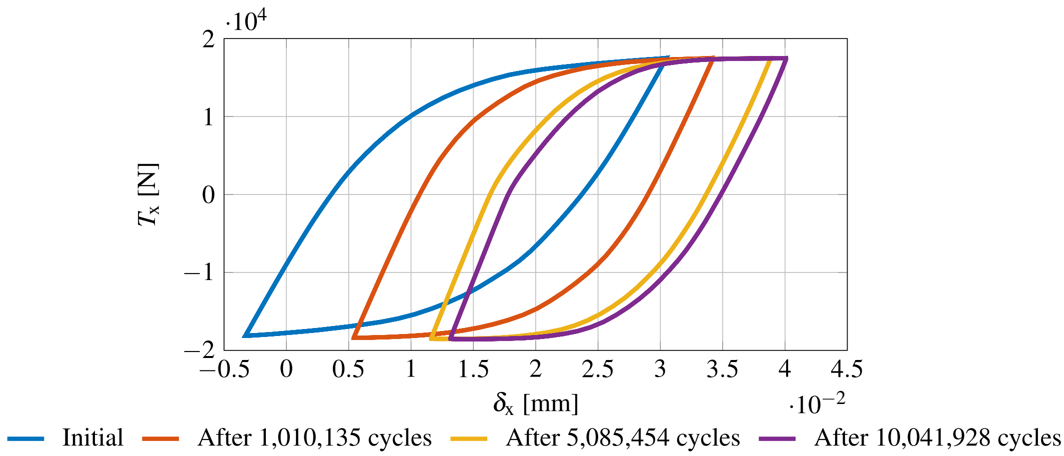

Fig. 6.15 Evolution of dissipated energy per cycle with wear for $R_q = 5\,\mu m$

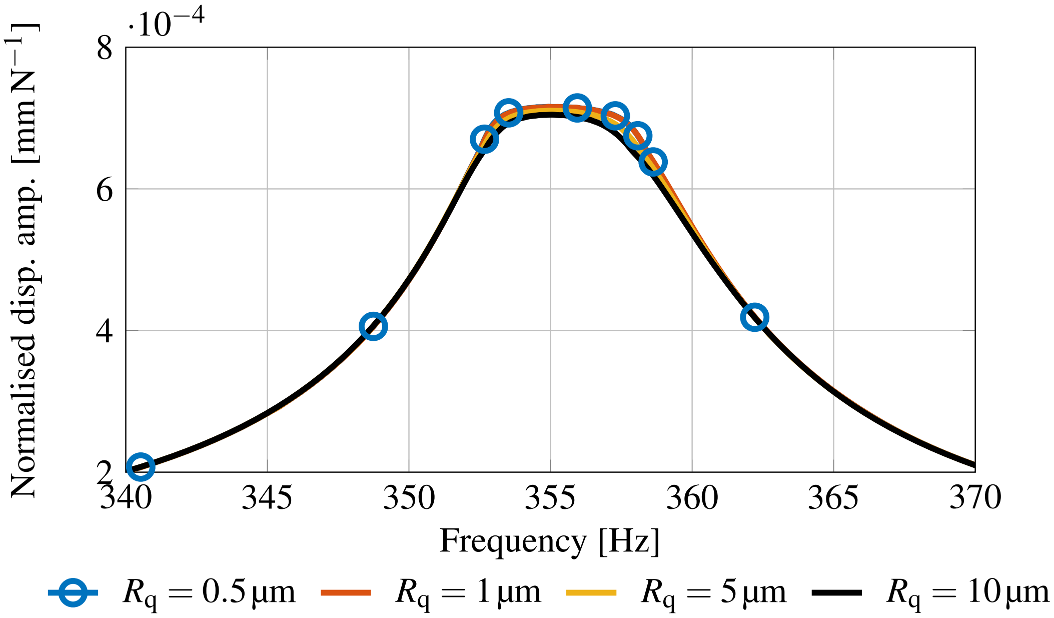

Fig. 6.16 Final FRFs for different initial rms roughness

Figure 6.16 shows the frequency response functions of the worn surfaces obtained after 10 million cycles. By comparing it with Fig. 6.1, it can be observed that due to wear, the responses are getting closer to each other and are nearly identical after 10 million cycles. This result is supported by Fig. 6.9 and Fig. 6.17 which show that after 10 millions cycles, all initial rough surface tend to nearly identical global contact stiffness and wear rate. It can also be observed from Fig. 6.17 that the higher the initial rms roughness, the higher the wear rates, and that the wear rate decreases to a steady state value, which has been previously observed by Ghosh and Sadeghi [55]. These findings have also been observed experimentally by Kubiak et al. [88].

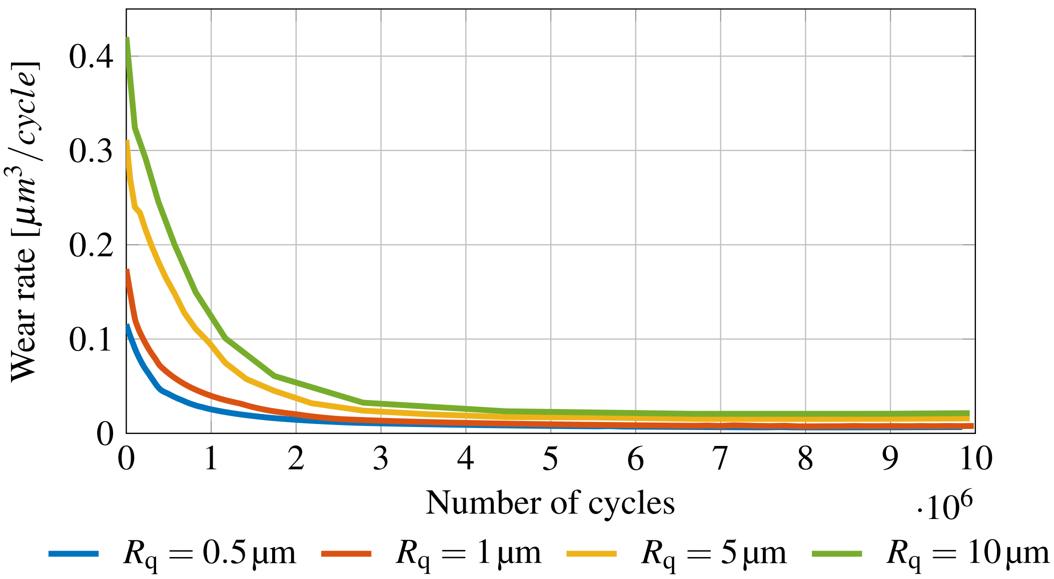

Fig. 6.17 Wear rates for different initial rms roughness

Effects of plasticity

In order to evaluate the potential influence of plasticity on the wear analysis of a rough contact, a hardness limit of the contact pressure, has been introduced here and the analysis has been done on the surface with an initial rms roughness of 5 µm. The hardness limit was set to 600 MPa which is an average value of compressive yield strength for steel material. Figure 6.18 shows the initial pressure distribution for the elastic and the elastic-perfectly-plastic contacts. It can be seen that the pressure distribution is strongly affected by the hardness limit: the numerous peaks that were higher to 600 MPa in the elastic contact, are now all equal to 600 MPa. This change of pressure distribution also comes with a slight increase of the contact area, as shown in Fig. 6.19. Figure 6.20 shows the evolution of the normal contact stiffness

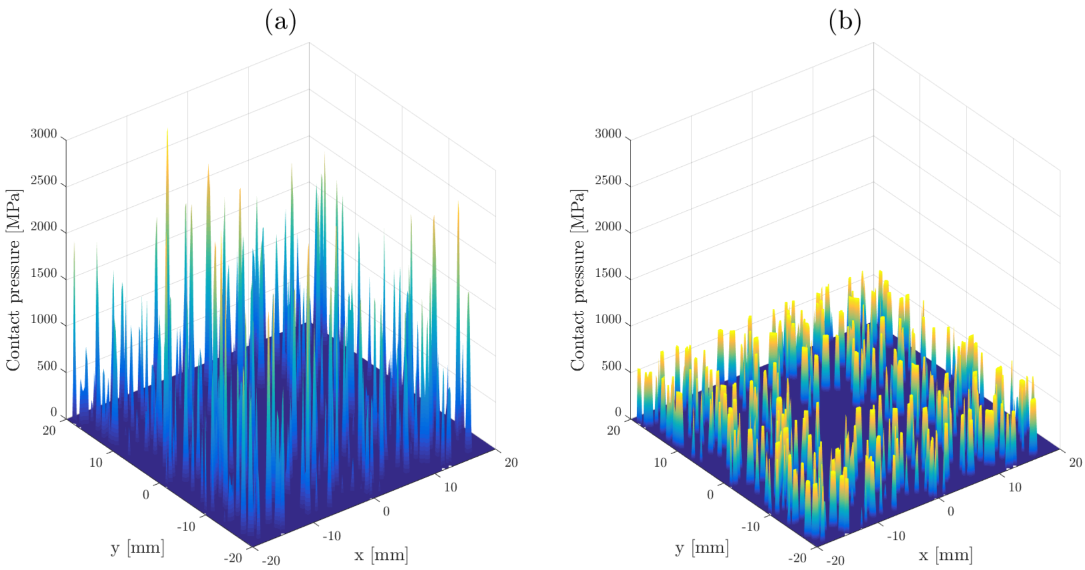

Fig. 6.18 Initial contact pressure [MPa] for the elastic (a) and elastic-perfectly-plastic with $p_{\max} = 600\,\text{MPa}$ (b) contact

with wear. Since the contact area is only slightly varying between the elastic and the elastic-perfectly-plastic contact, the differences that are observed for the contact stiffness are due to the change of the pressure distribution alone. As discussed in the previous chapter, a lower normal load leads to a lower normal contact stiffness, which is observed here. These differences can be observed up to approximately 2 millions cycles. At this stage, all the pressures are below 600 MPa which means that the plasticity is no longer activated, and that the behaviour becomes identical to that of the elastic contact.

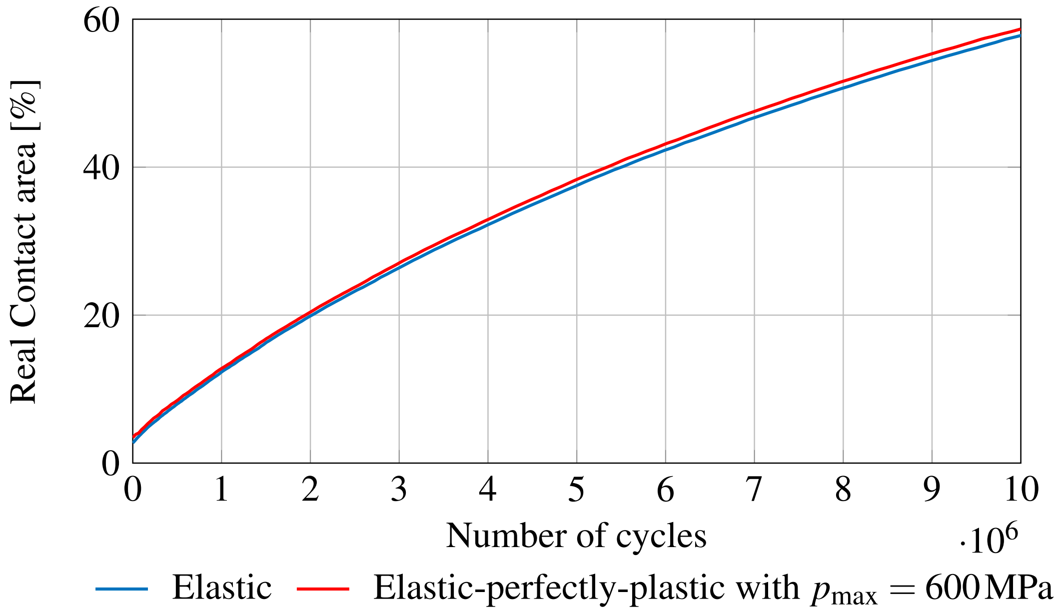

Fig. 6.19 Evolution of real contact area with wear for elastic and elastic-perfectly-plastic behaviour

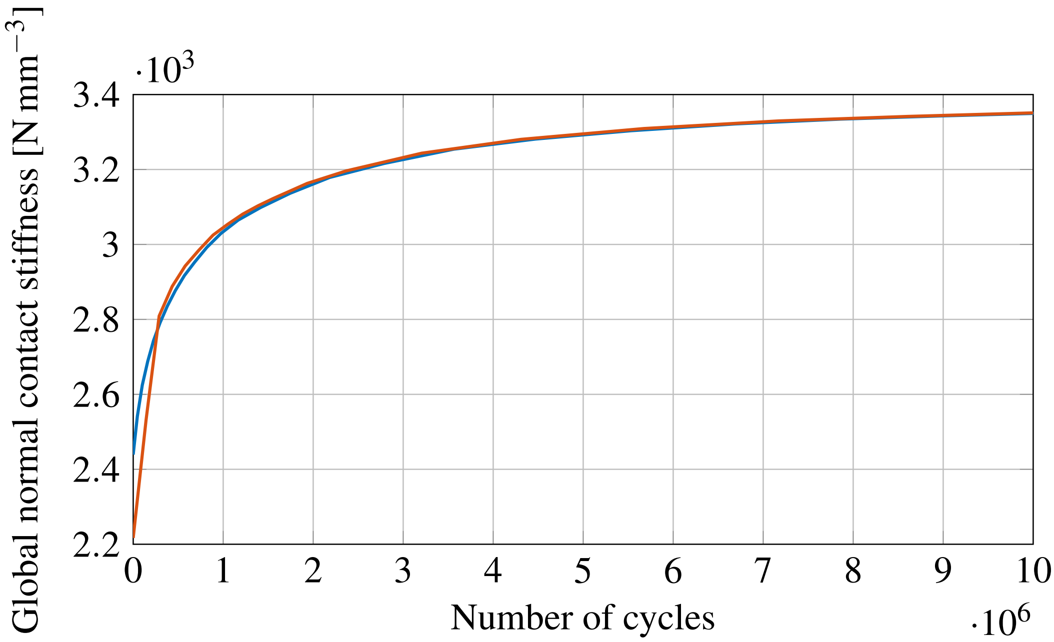

Fig. 6.20 Evolution of global normal contact stiffness with wear for elastic and elastic-perfectly-plastic behaviour

The same observations can be made on the evolution of the cumulated dissipated energy, depicted in Fig. 6.21: the wear rates, which are equal to the slope of these curves multiplied by the wear coefficient, differ during the running-in phase until they reach a similar value after 2 million cycles.

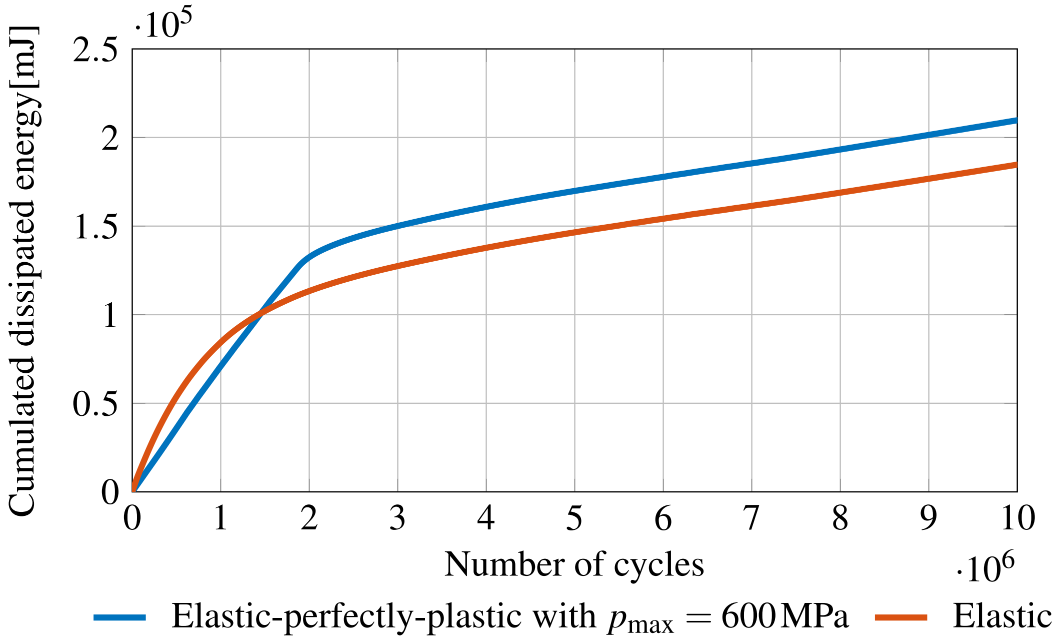

Fig. 6.21 Cumulated dissipated energy for elastic and elastic-perfectly-plastic behaviour

6.3 Conclusions

In this chapter, the proposed multiscale approach has been used to conduct fretting wear analysis of a single bolted joint with a rough contact interface, bringing all the previously proposed techniques together. Fretting wear was first shown to have a strong impact on the contacting surface geometry. As the surface wears out, its initial roughness is progressively removed and all its roughness parameters are changed. The changes of contact geometry are in turn affecting the contact conditions: as the initial roughness of the surface is being removed, the contact area is significantly increased and as a result the pressure distribution in strongly affected: the initial high peaks of pressure are turning into nearly flat patches of much lower pressure. Also due to the variation of the contact area, the global normal contact stiffness of the joint was shown to increase with wear.

In order to evaluate the mutual effects of these changes of contact conditions and the nonlinear dynamics of the system, a question which was raised in the third chapter was addressed here: an update criterion of the nonlinear dynamic model has been proposed. The nonlinear dynamic model should be updated after a certain variation of the global contact stiffness is observed during the wear simulations performed with the contact solver. The appropriate value of this variation must be determined for each system since it depends on the sensitivity of its dynamic behaviour to changes of contact conditions. For the presented particular application, updating the nonlinear dynamic model every 20%, 10% and 5% did not result in any noticeable change of the nonlinear dynamic response of the joint. As a result, no update was required to study the effects of roughness on wear rate and on the nonlinear dynamic response up to the simulated 10 million cycles.

From a wear perspective, higher wear rates were observed for higher values of roughness which resulted in initial significant differences between the four different rough surfaces. However, after the loss of the initial roughness, a steady-state phase was observed during which the wear rates reached nearly the same value for all surfaces.

As for the nonlinear dynamics, it was shown that the loss of roughness due to wear resulted in a global stiffening of the contact interface and thus to a shift of the resonance frequency to the higher frequencies, and in a lower energy dissipation which means higher amplitude of the frequency response function.

The effects of plasticity were also discussed but it is worth reminding that plasticity has been implemented here in a very simplified manner, via a hardness limit applied to the pressure, which does not allow to capture the real physics of a plastic behaviour. Nevertheless, this study emphasizes the strong effects of a change of pressure distribution alone and suggests that plasticity should be considered for a more realistic analysis.

Chapter 7

Conclusions and perspectives

The main objective of this work was to evaluate and understand the effects of a change of the contact geometry due fretting wear on the nonlinear dynamic response of a jointed structure with dry friction interfaces. This objective has been achieved by developing a multiscale approach combining a BEM-based contact solver, an energy wear approach and a multiharmonic balance solver. The main achievements and findings of this work will be summarised here and then a few recommendations on potential future developments will be made.

Fretting wear modelling

In order to evaluate fretting wear and its impact on the nonlinear dynamic response, an accurate representation of the contact conditions is required. To this end, a contact solver based on boundary integral equations has been implemented. Owing to its computational efficiency, it makes it possible to use a very fine mesh of the contact area and extract accurate contact conditions at a low computational cost compared to the classical Finite Element Method.

Based on the obtained accurate contact conditions, local wear depths were computed using an energy wear approach which assumes that the wear volume is proportional to the frictional dissipated energy. This approach was chosen for its ability to accurately capture wear, which was demonstrated in previous experiments, and for its ease of implementation.

A thorough verification of the contact solver against analytical solutions and FE simulations demonstrated its accuracy and computational benefits over the Finite Element Method. Furthermore, the comparisons with FEM results showed to how much extent the accuracy of the solver results could be altered due to its underlying half-space assumption. As a result, the implemented contact solver provides accurate and reliable results for problems where the contact area is small compared to the dimensions of the contacting bodies. For other cases such as a conforming contact between perfectly flat and smooth surfaces, the Finite Element Method should be used instead.

Applications of the multiscale approach

The proposed multiscale approach was first applied to an underplatform-damper system with a smooth contact interface. The obtained results highlighted the sensitivity of the nonlinear dynamic response to changes at the contact interface; the changes of contact geometry due to wear led to a redistribution of the contact pressure, which in turn changed the underlying nonlinear mechanisms at the interface from sliding at the edges only to sliding over a larger part of the contact interface, thereby increasing the frictional dissipated energy. This first application showed the relevance and the interest of the proposed approach for this type of turbomachinery application.

The multiscale approach was then applied to a 'resonator' system consisting of two masses linked together via a single bolted joint with a rough contact interface. In order to include the effects of surface roughness, the multiscale approach has been upgraded. In addition to the contact normal loads and the normal gaps, it was proposed to also update the normal and tangential contact stiffness of the nonlinear friction elements used in the MHBM solver based on the contact solver results. By doing so, the approach was able to capture the following mechanisms which are characteristic of a rough contact; the surface roughness reduces drastically the real contact area, which leads to a complete redistribution of the contact pressure and to a strongly non-uniform distribution of contact stiffness. Higher values of roughness were shown to lead to a lower global stiffness of the joint and to higher energy dissipation. It was also found that for low values of root mean square (rms) roughness (below 5 µm), the effect of the roughness on the global nonlinear dynamic response was small enough to be neglected in the analysis but for accurate local contact predictions, even small roughness values must be considered in order to predict wear accurately and capture its impact on the nonlinear response over time correctly. For higher values of rms roughness, both the local and global dynamic behaviour was significantly affected, making rough contact analysis a crucial component for the accurate prediction of the nonlinear dynamic response over the life time of the structure.

Finally, the fully developed multiscale approach was used to conduct fretting wear analysis on that resonator system and to evaluate the effects of wear on the nonlinear dynamic behaviour of the system. Fretting wear was first shown to have a strong impact on the contacting surface geometry, which in turn strongly affected the the normal load distribution and contact stiffness input parameters for the nonlinear dynamic response. As the surface wears out, its initial roughness is progressively removed and all its roughness parameters are changed, which in turn affects the contact conditions. It could be shown that, as the initial roughness of the surface is being removed, the contact area is significantly increased and as a result the pressure distribution is strongly affected with the initial high and very localised peaks of pressure turning into nearly flat patches of much lower pressure. A further important effect for the nonlinear dynamic analysis was an observed rise of the global contact stiffness due to wear resulting from an increase of the contact area. Higher wear rates were observed for higher values of roughness, but after the loss of the initial roughness, a steady-state phase was observed during which the wear rates reached nearly the same value for all surfaces. The loss of roughness due to wear resulted in a global stiffening of the contact interface and thus led to a small increase of the resonance frequency of the system, and to a lower energy dissipation resulting in an higher amplitude of the frequency response function.

In summary, the work in this thesis introduced a fully integrated approach that allowed the prediction of the evolution of the vibration behaviour of an assembled system over time due to fretting wear. The developed tool has enabled an in-depth study of the effects of contact conditions, including pressure distribution and contact stiffness, and changes of these contact conditions due to fretting wear on the nonlinear dynamic response of the jointed structure. Several future developments can be recommended to further improve the computational efficiency of the approach, as discussed hereafter.

Recommendations for future work

Although the presented contact solver, in its current state, allows highly efficient computation of the contact conditions, the use of recent developments could further improve that efficiency and therefore make the fretting wear simulations even faster. These recent developments include the work of Vollebregt [188] who showed that the number of conjugate gradient iterations could be significantly reduced by using a FFT-based preconditioner. Another one is due to Paggi [9] who presented a comprehensive comparison of the available optimisation algorithms for the solution of the frictionless normal contact between rough surfaces and showed that the Non-Negative Least Squares (NNLS) algorithm was one order of magnitude faster that a constrained conjugate gradient algorithm.

In addition, the current implementation of elasto-plastic contact via a hardness limit is very simplified and does not allow to capture the real physics of a plastic behaviour. The presence of a plastic flow inside the bulk of the material requires the consideration of the residual displacement induced by plastic strain. As a result, the surface displacements are no longer just a function of the pressure and the shear stresses, but they also depend on the plastic strain. A 3D-FFT, instead of a 2D-FFT, must therefore be used with additional influence coefficients to compute these displacements. The developments of Jacq et al. [73] and Wang et al. [193] could be used as a basis to introduce plasticity more appropriately in the presented contact solver.

Furthermore, in the present work, the contact solver was used to determine the parameters of the macro-slip nonlinear friction elements, including the normal and tangential contact stiffness. As a result, the micro-slip behaviour, which can be captured by the implemented contact solver, is lost in the nonlinear dynamic model. One way to improve that would be to tune the normal and tangential contact stiffness of the macroslip element so that it dissipates the same frictional energy than that obtained from the contact solver. Thus, the energy dissipation in the nonlinear dynamic analysis would be closer to that of a real rough contact exhibiting micro-slip and macro-slip behaviours, but the joint stiffness might be altered, and a significant increase in computational time would be required. Alternatively, a micro-slip friction element could be included in the multiharmonic balance solver, where its parameters would be supplied by the contact solver. This solution is currently being investigated and is showing promising results [127].

Lastly, the relevance, ease of implementation and computational benefits of the proposed multiscale approach have been demonstrated in the present work. However, in order to gain more trust in its results, a series of experimental validations should be conducted. A test rig such as the one developed by Pesaresi [128] could be a good candidate to conduct these experiments. It is indeed a relevant industrial test case since it is representative of engine high pressure turbine underplatform dampers which are known to significantly wear in service. Due to the intended strong energy dissipation at the contact interface, and with an appropriate choice of material and loading conditions, it should be possible to quickly observe the effects of wear.

References

[1] Abdelaziz, Y. and Hamouine, A. (2008). A survey of the extended finite element. *Computers & Structures*, 86(11-12):1141–1151.

[2] Aghababaei, R., Warner, D. H., and Molinari, J.-F. (2016). Critical length scale controls adhesive wear mechanisms. *Nature Communications*, 7:11816.

[3] Aghdam, A. B. and Khonsari, M. M. (2011). On the correlation between wear and entropy in dry sliding contact. *Wear*, 270(11-12):781–790.

[4] Albertson, F. and Gilbert, J. (2001). Harmonic balance method used for calculating the steady state oscillations of a simple one-cylinder cold engine. *Journal of Sound and Vibration*, 241(4):541–565.

[5] Aliabadi, M. (2002). *The Boundary Element Method, Applications in Solids and Structures*. The Boundary Element Method. John Wiley & Sons.

[6] Archard, J. F. (1953). Contact and rubbing of flat surfaces. *J. Appl. Phys.*, 24(8):981.

[7] Archard, J. F. and Hirst, W. (1956). The wear of metals under unlubricated conditions. 236(1206):397–410.

[8] Bampton, M. C. C. and Craig, R. R. (1968). Coupling of substructures for dynamic analyses. *AIAA Journal*, 6(7):1313–1319.

[9] Bemporad, A. and Paggi, M. (2015). Optimization algorithms for the solution of the frictionless normal contact between rough surfaces. *International Journal of Solids and Structures*, 69-70:94–105.

[10] Bergstrom, D. (2010). Rough surface generation.

[11] Besselink, B., Tabak, U., Lutowska, A., van de Wouw, N., Nijmeijer, H., Rixen, D., Hochstenbach, M., and Schilders, W. (2013). A comparison of model reduction techniques from structural dynamics, numerical mathematics and systems and control. *Journal of Sound and Vibration*, 332(19):4403–4422.

[12] Bhaskaran, H., Gotsmann, B., Sebastian, A., Drechsler, U., Lantz, M. A., Despont, M., Jaroenapibal, P., Carpick, R. W., Chen, Y., and Sridharan, K. (2010). Ultralow nanoscale wear through atom-by-atom attrition in silicon-containing diamond-like carbon. *Nature Nanotechnology*, 5(3):181–185.

[13] Bhushan, B. (2000). Surface roughness analysis and measurement techniques. In *Modern Tribology Handbook, Two Volume Set*. CRC Press.

[14] Boucly, V., Nélias, D., Liu, S., Wang, Q. J., and Keer, L. M. (2005). Contact analyses for bodies with frictional heating and plastic behavior. *Journal of Tribology*, 127(2):355.

[15] Boussinesq, J. (1885). *Application des potentiels à l'étude de l'équilibre et du mouvement des solides élastiques...* Gauthier-Villars.

[16] Brake, M. R., editor (2018). *The Mechanics of Jointed Structures*. Springer International Publishing.

[17] Brandt, A. and Lubrecht, A. (1990). Multilevel matrix multiplication and fast solution of integral equations. *Journal of Computational Physics*, 90(2):348–370.

[18] Bryant, M. D., Khonsari, M. M., and Ling, F. F. (2008). On the thermodynamics of degradation. 464(2096):2001–2014.

[19] Bucher, F., Dmitriev, A., Ertz, M., Knothe, K., Popov, V., Psakhie, S., and Shilko, E. (2006). Multiscale simulation of dry friction in wheel/rail contact. *Wear*, 261(7-8):874–884.

[20] Cai, M. B., Li, X. P., and Rahman, M. (2007). Study of the mechanism of groove wear of the diamond tool in nanoscale ductile mode cutting of monocrystalline silicon. *Journal of Manufacturing Science and Engineering*, 129(2):281–286.

[21] Calamaz, M., Limido, J., Nouari, M., Espinosa, C., Coupard, D., Salaün, M., Girot, F., and Chieragatti, R. (2009). Toward a better understanding of tool wear effect through a comparison between experiments and SPH numerical modelling of machining hard materials. *International Journal of Refractory Metals and Hard Materials*, 27(3):595–604.

[22] Cameron, T. M. and Griffin, J. H. (1989). An alternating frequency/time domain method for calculating the steady-state response of nonlinear dynamic systems. *Journal of Applied Mechanics*, 56(1):149.

[23] Cattaneo, C. (1938). Sul contatto di due corpi elastici: distribuzione locale degli sforzi. *Rendiconti dell'Aecademia Nazionale dei Lincei*, 27:342–348,434–436,474–478.

[24] Cerruti, V. (1882). *Ricerche intorno all'equilibrio de'corpi elastici isotropi: memoria*. coi tipi del Salviucci.

[25] Charleux, D., Gibert, C., Thouverez, F., and Dupeux, J. (2006). Numerical and experimental study of friction damping blade attachments of rotating bladed disks. *International Journal of Rotating Machinery*, 2006:1–13.

[26] Chen, J., Yang, B., and Menq, C. (2000). Periodic forced response of structures having three-dimensional frictional constraints. *Journal of Sound and Vibration*, 229(4):775–792.

[27] Cheng, K., Luo, X., Ward, R., and Holt, R. (2003). Modeling and simulation of the tool wear in nanometric cutting. *Wear*, 255(7-12):1427–1432.

[28] Cigeroglu, E., An, N., and Menq, C.-H. (2009). Forced response prediction of constrained and unconstrained structures coupled through frictional contacts. *Journal of Engineering for Gas Turbines and Power*, 131(2):022505.

[29] Cigeroglu, E., Lu, W., and Menq, C.-H. (2006). One-dimensional dynamic microslip friction model. *Journal of Sound and Vibration*, 292(3-5):881–898.

[30] Csaba, G. (1995). *Microslip Friction Damping: With Special Reference to Turbine Blade Vibrations*. LiU-Tek-Lic. Univ.

[31] Csaba, G. (1998). *Modelling microslip friction damping and its influence on turbine blade vibrations*. Division of Machine Design, Department of Mechanical Engineering, Linköping University.

[32] Cundall, P. A. and Strack, O. D. L. (1979). A discrete numerical model for granular assemblies. *Géotechnique*, 29(1):47–65.

[33] Dahl, P. R. (1976). Solid friction damping of mechanical vibrations. *AIAA Journal*, 14(12):1675–1682.

[34] de Wit, C. C., Olsson, H., Astrom, K., and Lischinsky, P. (1995). A new model for control of systems with friction. *IEEE Transactions on Automatic Control*, 40(3):419–425.

[35] Desai, C. S., Zaman, M. M., Lightner, J. G., and Siriwardane, H. J. (1984). Thin-layer element for interfaces and joints. *International Journal for Numerical and Analytical Methods in Geomechanics*, 8(1):19–43.

[36] Dick, T. (2006). *Modélisation multiéchelle du phénomène de fretting dans le contact aube-disque*. Theses, École Nationale Supérieure des Mines de Paris.

[37] Doelling, K. L., Ling, F. F., Bryant, M. D., and Heilman, B. P. (2000). An experimental study of the correlation between wear and entropy flow in machinery components. *J. Appl. Phys.*, 88(5):2999.

[38] Dowell, E. (1983). The behavior of a linear, damped modal system with a non-linear spring-mass-dry friction damper system attached. *Journal of Sound and Vibration*, 89(1):65–84.

[39] Dragon-Louiset, M. (2001). On a predictive macroscopic contact-sliding wear model based on micromechanical considerations. *International Journal of Solids and Structures*, 38(9):1625–1639.

[40] Ferri, A. and Dowell, E. (1988). Frequency domain solutions to multi-degree-of-freedom, dry friction damped systems. *Journal of Sound and Vibration*, 124(2):207–224.

[41] Ferri, A. A. (1986). On the equivalence of the incremental harmonic balance method and the harmonic balance-newton raphson method. *Journal of Applied Mechanics*, 53(2):455.

[42] Ferri, A. A. (1995). Friction damping and isolation systems. *Journal of Vibration and Acoustics*, 117(B):196.

[43] Firrone, C. M. and Zucca, S. (2011). Modelling friction contacts in structural dynamics and its application to turbine bladed disks. In *Numerical Analysis - Theory and Application*. InTech.

[44] Fouvry, S., Duó, P., and Perruchaut, P. (2004). A quantitative approach of Ti–6Al–4V fretting damage: friction, wear and crack nucleation. *Wear*, 257(9-10):916–929.

[45] Fouvry, S., Liskiewicz, T., Kapsa, P., Hannel, S., and Sauger, E. (2003a). An energy description of wear mechanisms and its applications to oscillating sliding contacts. *Wear*, 255(1-6):287–298.

[46] Fouvry, S., Liskiewicz, T., Kapsa, P., Hannel, S., and Sauger, E. (2003b). An energy description of wear mechanisms and its applications to oscillating sliding contacts. *Wear*, 255(1-6):287–298.

[47] Fransson, T. (1999). *Aeroelasticity in axial flow turbomachines*. Von Karman Inst. for Fluid Dynamics.

[48] Frigo, M. and Johnson, S. G. (2005). The design and implementation of FFTW3. *Proceedings of the IEEE*, 93(2):216–231. Special issue on "Program Generation, Optimization, and Platform Adaptation".

[49] Galin, L. A. (1953). *Contact Problems in the Theory of Elasticity*. English translation by H.Moss, edited by I. N. Sneddon, North Carolina State College, Departments of Mathematics and Engineering Research, NSF Grant No. G16447, 1961.

[50] Gallego, L. (2007). *Fretting et Usure des Contacts Mecaniques : Modelisation Numerique*. PhD thesis, INSA Lyon.

[51] Gallego, L., Fulleringer, B., Deyber, S., and Nélias, D. (2010). Multiscale computation of fretting wear at the blade/disk interface. *Tribology International*, 43(4):708–718.

[52] Garcia, N. and Stoll, E. (1984). Monte carlo calculation for electromagnetic-wave scattering from random rough surfaces. *Physical Review Letters*, 52(20):1798–1801.

[53] Gaul, L. and Lenz, J. (1997). Nonlinear dynamics of structures assembled by bolted joints. *Acta Mechanica*, 125(1-4):169–181.

[54] Gaul, L. and Nitsche, R. (2001). The role of friction in mechanical joints. *Applied Mechanics Reviews*, 54(2):93.

[55] Ghosh, A. and Sadeghi, F. (2015). A novel approach to model effects of surface roughness parameters on wear. *Wear*, 338-339:73–94.

[56] Gingold, R. A. and Monaghan, J. J. (1977). Smoothed particle hydrodynamics: theory and application to non-spherical stars. *Monthly Notices of the Royal Astronomical Society*, 181(3):375–389.

[57] Goel, S., Luo, X., and Reuben, R. L. (2012). Molecular dynamics simulation model for the quantitative assessment of tool wear during single point diamond turning of cubic silicon carbide. *Computational Materials Science*, 51(1):402–408.

[58] Goel, S., Luo, X., and Reuben, R. L. (2013). Wear mechanism of diamond tools against single crystal silicon in single point diamond turning process. *Tribology International*, 57:272–281.

[59] Goodman, R. E., Taylor, R. L., and Brekke, T. L. (1968). A model for the mechanics of jointed rocks. *Journal of Soil Mechanics & Foundations Div*.

[60] Goryacheva, I. (2002). Contact problem with partial slip for the inclined punch with rounded edges. *International Journal of Fatigue*, 24(11):1191–1201.

[61] Gotsmann, B. and Lantz, M. A. (2008). Atomistic wear in a single asperity sliding contact. *Physical Review Letters*, 101(12).

[62] Gray, P. and McCarthy, C. (2010). A global bolted joint model for finite element analysis of load distributions in multi-bolt composite joints. *Composites Part B: Engineering*, 41(4):317–325.

[63] Griffin, J. H. (1980). Friction damping of resonant stresses in gas turbine engine airfoils. *Journal of Engineering for Power*, 102(2):329.

[64] Griffin, J. H. and Sinha, A. (1985). The interaction between mistuning and friction in the forced response of bladed disk assemblies. *Journal of Engineering for Gas Turbines and Power*, 107(1):205.

[65] Hertz, H. (1881). On the contact of elastic solids. *J. reine angew. Math*, 92(156–171):110.

[66] Hestenes, M. R. (1980). Conjugate direction methods. In *Conjugate Direction Methods in Optimization*, pages 81–149. Springer Nature.

[67] Hills, D., Nowell, D., and Sackfield, A. (1993). Rough contacts and numerical methods. In *Mechanics of Elastic Contacts*, pages 392–438. Elsevier.

[68] Hohl, A., Siewert, C., Panning, L., and Kayser, A. (2008). Nonlinear vibration analysis of gas turbine bladings with shroud coupling. In *Volume 5: Structures and Dynamics, Parts A and B*. ASME.

[69] Huq, M. Z. and Celis, J.-P. (2002). Expressing wear rate in sliding contacts based on dissipated energy. *Wear*, 252(5-6):375–383.

[70] Ismail, M., Ikhouane, F., and Rodellar, J. (2009). The hysteresis bouc-wen model, a survey. *Archives of Computational Methods in Engineering*, 16(2):161–188.

[71] Iwan, W. D. (1966). A distributed-element model for hysteresis and its steady-state dynamic response. *Journal of Applied Mechanics*, 33(4):893.

[72] Jacobs, T. D. B. and Carpick, R. W. (2013). Nanoscale wear as a stress-assisted chemical reaction. *Nature Nanotechnology*, 8(2):108–112.

[73] Jacq, C., Nélias, D., Lormand, G., and Girodin, D. (2002). Development of a three-dimensional semi-analytical elastic-plastic contact code. *Journal of Tribology*, 124(4):653.

[74] Jareland, M. H. and Csaba, G. (2000). Friction damper mistuning of a bladed disk and optimization with respect to wear. In *Volume 4: Manufacturing Materials and Metallurgy Ceramics Structures and Dynamics Controls, Diagnostics and Instrumentation Education*. ASME.

[75] Jesus, M. and Yebra-Pimentel, E. (2012). Hydrogel contact lenses surface roughness and bacterial adhesion. In *Ocular Diseases*. InTech.

[76] Johansson, L. (1994). Numerical simulation of contact pressure evolution in fretting. *J. Tribol.*, 116(2):247.

[77] Johnson, K. L. (1985). *Contact Mechanics*. Cambridge University Press (CUP).

[78] Ju, Y. and Farris, T. N. (1996). Spectral analysis of two-dimensional contact problems. *J. Tribol.*, 118(2):320–328.

[79] Kaliakin, V. and Li, J. (1995). Insight into deficiencies associated with commonly used zero-thickness interface elements. *Computers and Geotechnics*, 17(2):225–252.

[80] Kalker, J. J. (1990). *Three-Dimensional Elastic Bodies in Rolling Contact*. Springer Netherlands.

[81] Karekal, S., Das, R., Mosse, L., and Cleary, P. W. (2011). Application of a mesh-free continuum method for simulation of rock caving processes. *International Journal of Rock Mechanics and Mining Sciences*, 48(5):703–711.

[82] Khoei, A. and Nikbakht, M. (2006). Contact friction modeling with the extended finite element method (x-FEM). *Journal of Materials Processing Technology*, 177(1-3):58–62.

[83] Kim, J., Yoon, J.-C., and Kang, B.-S. (2007). Finite element analysis and modeling of structure with bolted joints. *Applied Mathematical Modelling*, 31(5):895–911.

[84] Kim, N. H., Won, D., Burris, D., Holtkamp, B., Gessel, G. R., Swanson, P., and Sawyer, W. G. (2005). Finite element analysis and experiments of metal/metal wear in oscillatory contacts. *Wear*, 258(11-12):1787–1793.

[85] Kim, T. W., Moon, S. M., and Cho, Y. J. (2011). Prediction of fretting wear using boundary element method. *Tribology International*, 44(11):1571–1576.

[86] Klamecki, B. E. (1980). Wear — an entropy production model. *Wear*, 58(2):325–330.

[87] Krack, M., Salles, L., and Thouverez, F. (2016). Vibration prediction of bladed disks coupled by friction joints. *Archives of Computational Methods in Engineering*, 24(3):589–636.

[88] Kubiak, K., Liskiewicz, T., and Mathia, T. (2011). Surface morphology in engineering applications: Influence of roughness on sliding and wear in dry fretting. *Tribology International*, 44(11):1427–1432.

[89] Legrand, M., Roques, S., Pierre, C., Peseux, B., and Cartraud, P. (2006). n-dimensional harmonic balance method extended to non-explicit nonlinearities. *Revue européenne de mécanique numérique*, 15(1-2-3):269–280.

[90] Leonard, B. D. (2008). *An experimental and numerical investigation of the effect of coatings and third body on fretting wear*. PhD thesis, Purdue University.

[91] Leonard, B. D., Ghosh, A., Sadeghi, F., Shinde, S., and Mittelbach, M. (2014). Third body modeling in fretting using the combined finite-discrete element method. *International Journal of Solids and Structures*, 51(6):1375–1389.

[92] Leonard, B. D., Patil, P., Slack, T. S., Sadeghi, F., Shinde, S., and Mittelbach, M. (2011). Fretting wear modeling of coated and uncoated surfaces using the combined finite-discrete element method. *J. Tribol.*, 133(2):021601.

[93] Levy, G. (1980). Modelling of coulomb damping and wear of vibrating systems. *Wear*, 64(1):57–82.

[94] Ling, F. F., Bryant, M. D., and Doelling, K. L. (2002). On irreversible thermodynamics for wear prediction. *Wear*, 253(11-12):1165–1172.

[95] Liu, G., Wang, Q., and Liu, S. (2001). A three-dimensional thermal-mechanical asperity contact model for two nominally flat surfaces in contact. *Journal of Tribology*, 123(3):595.

[96] Liu, S. and Wang, Q. (2002). Studying contact stress fields caused by surface tractions with a discrete convolution and fast fourier transform algorithm. *Journal of Tribology*, 124(1):36.

[97] Liu, S., Wang, Q., and Liu, G. (2000). A versatile method of discrete convolution and FFT (DC-FFT) for contact analyses. *Wear*, 243(1-2):101–111.

[98] Love, A. (1906). *A Treatise on the Mathematical Theory of Elasticity*. A Treatise on the Mathematical Theory of Elasticity. at the University Press.

[99] Love, A. E. H. (1929). The stress produced in a semi-infinite solid by pressure on part of the boundary. *Philosophical Transactions of the Royal Society A: Mathematical, Physical and Engineering Sciences*, 228(659-669):377–420.

[100] Lubkin, J. L. (1951). The torsion of elastic spheres in contact. *J. Appl. Mech.-Transactions of the ASME*, 18(2):183–187.

[101] Lubrecht, A. A. and Ioannides, E. (1991). A fast solution of the dry contact problem and the associated sub-surface stress field, using multilevel techniques. *J. Tribol.*, 113(1):128–133.

[102] Lucy, L. B. (1977). A numerical approach to the testing of the fission hypothesis. *The Astronomical Journal*, 82:1013.

[103] Luding, S. (2008). Introduction to discrete element methods. basic of contact force models and how to perform the micro-macro transition to continuum theory. *Revue européenne de génie civil*, 12(7-8):785–826.

[104] Lur'e, A. I. (1964). *Three-Dimensional Problems of the Theory of Elasticity*. New York, Interscience Publishers.

[105] Maekawa, K. and Itoh, A. (1995). Friction and tool wear in nano-scale machining—a molecular dynamics approach. *Wear*, 188(1-2):115–122.

[106] Mayer, M. and Gaul, L. (2007). Segment-to-segment contact elements for modelling joint interfaces in finite element analysis. *Mechanical Systems and Signal Processing*, 21(2):724–734.

[107] Mayeur, C., Sainsot, P., and Flamand, L. (1995). A numerical elastoplastic model for rough contact. *Journal of Tribology*, 117(3):422.

[108] McColl, I. R., Ding, J., and Leen, S. B. (2004). Finite element simulation and experimental validation of fretting wear. *Wear*, 256(11-12):1114–1127.

[109] Meng, H. and Ludema, K. (1995). Wear models and predictive equations: their form and content. *Wear*, 181-183:443–457.

[110] Menq, C.-H., Chidamparam, P., and Griffin, J. (1991). Friction damping of two-dimensional motion and its application in vibration control. *Journal of Sound and Vibration*, 144(3):427–447.

[111] Merkle, A. P. and Marks, L. D. (2008). Liquid-like tribology of gold studied by in situ TEM. *Wear*, 265(11-12):1864–1869.

[112] Mindlin, R. D. (1989). Compliance of elastic bodies in contact. In *The Collected Papers of Raymond D. Mindlin Volume I*, pages 197–206. Springer Science + Business Media.

[113] Molinari, J. F., Ortiz, M., Radovitzky, R., and Repetto, E. A. (2001). Finite-element modeling of dry sliding wear in metals. *Engineering Computations*, 18(3/4):592–610.

[114] Muskhelishvili, N. I. (1977). *Some Basic Problems of the Mathematical Theory of Elasticity*. Springer Nature.

[115] Müller, M. and Ostermeyer, G. (2007). A cellular automaton model to describe the three-dimensional friction and wear mechanism of brake systems. *Wear*, 263(7-12):1175–1188.

[116] Narayanan, S. and Sekar, P. (1998). A frequency domain based numeric-analytical method for non-linear dynamical systems. *Journal of Sound and Vibration*, 211(3):409–424.

[117] Nélias, D., Antaluca, E., and Boucly, V. (2007a). Rolling of an elastic ellipsoid upon an elastic-plastic flat. In *ASME/STLE 2007 International Joint Tribology Conference, Parts A and B*. ASME.

[118] Nélias, D., Antaluca, E., Boucly, V., and Cretu, S. (2007b). A three-dimensional semianalytical model for elastic-plastic sliding contacts. *Journal of Tribology*, 129(4):761.

[119] Nélias, D., Boucly, V., and Brunet, M. (2005). Elastic-plastic contact between rough surfaces: Proposal for a wear model. In *World Tribology Congress III, Volume 1*. ASME.

[120] Nogi, T. and Kato, T. (1997). Influence of a hard surface layer on the limit of elastic contact—part i: Analysis using a real surface model. *Journal of Tribology*, 119(3):493.

[121] Panning, L., Sextro, W., and Popp, K. (2003). Spatial dynamics of tuned and mistuned bladed disks with cylindrical and wedge-shaped friction dampers. *International Journal of Rotating Machinery*, 9(3):219–228.

[122] Paulin, C., Fouvry, S., and Deyber, S. (2005). Wear kinetics of Ti–6Al–4V under constant and variable fretting sliding conditions. *Wear*, 259(1–6):292–299.

[123] Paulin, C., Fouvry, S., and Meunier, C. (2008). Finite element modelling of fretting wear surface evolution: Application to a ti–6a1–4v contact. *Wear*, 264(1-2):26–36.

[124] Peng, W. and Bhushan, B. (2001). Three-dimensional contact analysis of layered elastic/plastic solids with rough surfaces. *Wear*, 249(9):741–760.

[125] Persson, B. (2006). Contact mechanics for randomly rough surfaces. *Surface Science Reports*, 61(4):201–227.

[126] Persson, B. N. J. (2001). Elastoplastic contact between randomly rough surfaces. *Physical Review Letters*, 87(11).

[127] Pesaresi, L., Armand, J., Salles, L., Schwingshackl, C., and Wong, C. (2017a). An advanced underplatform damper modelling approach based on a microslip contact model. In *Proceedings of the International Symposium on Transport Phenomena and Dynamics of Rotating Machinery*.

[128] Pesaresi, L., Salles, L., Jones, A., Green, J., and Schwingshackl, C. (2017b). Modelling the nonlinear behaviour of an underplatform damper test rig for turbine applications. *Mechanical Systems and Signal Processing*, 85:662–679.

[129] Petrov, E. P. (2005). Sensitivity analysis of nonlinear forced response for bladed discs with friction contact interfaces. In *Volume 4: Turbo Expo 2005*. ASME.

[130] Petrov, E. P. (2007). Direct parametric analysis of resonance regimes for nonlinear vibrations of bladed disks. *Journal of Turbomachinery*, 129(3):495.

[131] Petrov, E. P. (2010). A high-accuracy model reduction for analysis of nonlinear vibrations in structures with contact interfaces. In *Volume 6: Structures and Dynamics, Parts A and B*. ASME International.

[132] Petrov, E. P. (2011). A high-accuracy model reduction for analysis of nonlinear vibrations in structures with contact interfaces. *J. Eng. Gas Turb. Power*, 133(10):102503.

[133] Petrov, E. P. (2013). Analysis of nonlinear vibrations upon wear-induced loss of friction dampers in tuned and mistuned bladed discs. In *Volume 7A: Structures and Dynamics*. ASME.

[134] Petrov, E. P. and Ewins, D. J. (2003a). Analytical formulation of friction interface elements for analysis of nonlinear multi-harmonic vibrations of bladed disks. *J. Turbomach.*, 125(2):364–371.

[135] Petrov, E. P. and Ewins, D. J. (2003b). Analytical formulation of friction interface elements for analysis of nonlinear multi-harmonic vibrations of bladed disks. *J. Turbomach.*, 125(2):364.

[136] Petrov, E. P. and Ewins, D. J. (2004a). Generic friction models for time-domain vibration analysis of bladed disks. *J. Turbomach.*, 126(1):184.

[137] Petrov, E. P. and Ewins, D. J. (2004b). State-of-the-art dynamic analysis for non-linear gas turbine structures. *Proceedings of the Institution of Mechanical Engineers, Part G: Journal of Aerospace Engineering*, 218(3):199–211.

[138] Petrov, E. P. and Ewins, D. J. (2004c). State-of-the-art dynamic analysis for non-linear gas turbine structures. *Proceedings of the Institution of Mechanical Engineers, Part G: Journal of Aerospace Engineering*, 218(3):199–211.

[139] Petrov, E. P. and Ewins, D. J. (2006). Effects of damping and varying contact area at blade-disk joints in forced response analysis of bladed disk assemblies. *Journal of Turbomachinery*, 128(2):403.

[140] Petrov, E. P. and Ewins, D. J. (2007). Advanced modeling of underplatform friction dampers for analysis of bladed disk vibration. *J. Turbomach.*, 129(1):143.

[141] Pettigrew, M. and Taylor, C. (2003). Vibration analysis of shell-and-tube heat exchangers: an overview—part 2: vibration response, fretting-wear, guidelines. *Journal of Fluids and Structures*, 18(5):485–500.

[142] Põdra, P. and Andersson, S. (1999). Simulating sliding wear with finite element method. *Tribology International*, 32(2):71–81.

[143] Polonsky, I. and Keer, L. (1999). A numerical method for solving rough contact problems based on the multi-level multi-summation and conjugate gradient techniques. *Wear*, 231(2):206–219.

[144] Polonsky, I. A. and Keer, L. M. (2000). Fast methods for solving rough contact problems: A comparative study. *J. Tribol.*, 122(1):36–41.

[145] Popov, V. and Psakhie, S. (2007). Numerical simulation methods in tribology. *Tribology International*, 40(6):916–923.

[146] Popov, V., Psakhie, S., Gerve, A., Kehrwald, B., Shilko, E., and Dmitriev, A. (2001). Wear in combustion engines: experiment and simulation on a basis of movable cellular automaton method. *Phys. Mesomech*, 4.

[147] Popov, V. L. (2010). Contact between rough surfaces. In *Contact Mechanics and Friction*, pages 81–103. Springer Berlin Heidelberg.

[148] Popp, K., Panning, L., and Sextro, W. (2003). Vibration damping by friction forces: Theory and applications. *Modal Analysis*, 9(3-4):419–448.

[149] Press, W. H., Teukolsky, S. A., Vetterling, W. T., and Flannery, B. P. (1992). Numerical recipes in fortran 77: the art of scientific computing.

[150] Putignano, C., Ciavarella, M., and Barber, J. (2011). Frictional energy dissipation in contact of nominally flat rough surfaces under harmonically varying loads. *Journal of the Mechanics and Physics of Solids*, 59(12):2442–2454.

[151] Rabinowicz, E. (1965). *Friction and wear of materials*. Wiley series on the science and technology of materials. Wiley.

[152] Ramalho, A. and Miranda, J. (2006). The relationship between wear and dissipated energy in sliding systems. *Wear*, 260(4-5):361–367.

[153] Reid, J. D. and Hiser, N. R. (2005). Detailed modeling of bolted joints with slippage. *Finite Elements in Analysis and Design*, 41(6):547–562.

[154] Rizvi, A., Smith, C. W., Rajasekaran, R., and Evans, K. E. (2014). Dynamics of dry friction damping in gas turbines: literature survey. *Journal of Vibration and Control*, 22(1):296–305.

[155] Rodríguez-Tembleque, L., Abascal, R., and Aliabadi, M. (2012). Anisotropic fretting wear simulation using the boundary element method. *Computer Modeling in Engineering & Sciences(CMES)*, 87(2):127–156.

[156] Roy Craig, J. (2000). Coupling of substructures for dynamic analyses - an overview. In *41st Structures, Structural Dynamics, and Materials Conference and Exhibit*. American Institute of Aeronautics and Astronautics.

[157] Salles, L., Blanc, L., Thouverez, F., and Gouskov, A. (2011). Dynamic analysis of fretting-wear in friction contact interfaces. *International Journal of Solids and Structures*, 48(10):1513–1524.

[158] Salles, L., Blanc, L., Thouverez, F., Gouskov, A. M., and Jean, P. (2010). Multiscale analysis of fretting-wear under dynamical loading. *Méc. Ind*, 11(3-4):277–282.

[159] Salles, L., Blanc, L., Thouverez, F., Gouskov, A. M., and Jean, P. (2012). Dual time stepping algorithms with the high order harmonic balance method for contact interfaces with fretting-wear. *J. Eng. Gas Turb. Power*, 134(3):032503.

[160] Salles, L., Staples, B., Hoffmann, N., and Schwingshackl, C. (2016). Continuation techniques for analysis of whole aeroengine dynamics with imperfect bifurcations and isolated solutions. *Nonlinear Dynamics*, 86(3):1897–1911.

[161] Sanliturk, K. and Ewins, D. (1996). Modelling two-dimensional friction contact and its application using harmonic balance method. *Journal of Sound and Vibration*, 193(2):511–523.

[162] Sanliturk, K. Y., Imregun, M., and Ewins, D. J. (1997). Harmonic balance vibration analysis of turbine blades with friction dampers. *Journal of Vibration and Acoustics*, 119(1):96.

[163] Sato, T., Ishida, T., Jalabert, L., and Fujita, H. (2012). Real-time transmission electron microscope observation of nanofriction at a single ag asperity. *Nanotechnology*, 23(50):505701.

[164] Schwingshackl, C. W. (2012). Measurement of friction contact parameters for nonlinear dynamic analysis. In *Topics in Modal Analysis I, Volume 5*, pages 167–177. Springer Science Business Media.

[165] Schwingshackl, C. W., Maio, D. D., Sever, I., and Green, J. S. (2013). Modeling and validation of the nonlinear dynamic behavior of bolted flange joints. *Journal of Engineering for Gas Turbines and Power*, 135(12):122504.

[166] Schwingshackl, C. W. and Natoli, A. (2016). *Explicit Modelling of Microslip Behaviour in Dry Friction Contact*, pages 265–272. Springer International Publishing, Cham.

[167] Schwingshackl, C. W., Petrov, E. P., and Ewins, D. J. (2012). Measured and estimated friction interface parameters in a nonlinear dynamic analysis. *Mechanical Systems and Signal Processing*, 28:574–584.

[168] Segalman, D. J. (2005). A four-parameter iwan model for lap-type joints. *Journal of Applied Mechanics*, 72(5):752.

[169] Segalman, D. J. (2006). Modelling joint friction in structural dynamics. *Structural Control and Health Monitoring*, 13(1):430–453.

[170] Segalman, D. J., Starr, M. J., and Heinstein, M. W. (2005). New approximations for elastic spheres under an oscillating torsional couple. *Journal of applied mechanics*, 72(5):705–710.

[171] Sextro, W. (2007). *Dynamical Contact Problems with Friction*. Springer Science + Business Media.

[172] Sextro, W., Popp, K., and Wolter, I. (1997). Improved reliability of bladed disks due to friction dampers. *ASME paper*, (97-GT):189.

[173] Sfantos, G. and Aliabadi, M. (2006). Wear simulation using an incremental sliding boundary element method. *Wear*, 260(9-10):1119–1128.

[174] Sfantos, G. and Aliabadi, M. (2007). A boundary element formulation for three-dimensional sliding wear simulation. *Wear*, 262(5-6):672–683.

[175] Sharma, K. G. and Desai, C. S. (1992). Analysis and implementation of thin-layer element for interfaces and joints. *Journal of Engineering Mechanics*, 118(12):2442–2462.

[176] Sinha, A. and Griffin, J. H. (1984). Effects of static friction on the forced response of frictionally damped turbine blades. *Journal of Engineering for Gas Turbines and Power*, 106(1):65.

[177] Spinu, S. and Amarandei, D. (2012). Numerical simulation of slip-stick elastic contact. In *Numerical Simulation - From Theory to Industry*. InTech.

[178] Spreng, F., Eberhard, P., and Fleissner, F. (2013). An approach for the coupled simulation of machining processes using multibody system and smoothed particle hydrodynamics algorithms. *Theoretical and Applied Mechanics Letters*, 3(1):013005.

[179] Stenberg, N., Delić, A., and Björk, T. (2017). Using the SPH method to easier predict wear in machining. *Procedia CIRP*, 58:317–322.

[180] Süß, D. (2016). *Multi-Harmonische-Balance-Methoden zur Untersuchung des Übertragungsverhaltens von Strukturen mit Fügestellen*. PhD thesis, Dissertation, Erlangen, Friedrich-Alexander-Universität Erlangen-Nürnberg (FAU), 2016.

[181] Süß, D. and Willner, K. (2015). Investigation of a jointed friction oscillator using the multiharmonic balance method. *Mechanical Systems and Signal Processing*, 52-53:73–87.

[182] Tersoff, J. (1989). Modeling solid-state chemistry: Interatomic potentials for multicomponent systems. *Phys. Rev. B*, 39(8):5566–5568.

[183] Thomas, T. R. (1998). *Rough Surfaces*. Imperial College Press.

[184] Vahdat, V., Grierson, D. S., Turner, K. T., and Carpick, R. W. (2013). Mechanics of interaction and atomic-scale wear of amplitude modulation atomic force microscopy probes. *ACS Nano*, 7(4):3221–3235.

[185] Valanis, K. C. (1978). Fundamental consequences of a new intrinsic time measure. plasticity as a limit of the endochronic theory. Technical report, IOWA UNIV IOWA CITY.

[186] Vergne, F. (1985). ‘calcul des déplacements et des contraintes dans un demiespace élastique chargé en surface par des actions distribuées normales et tangentielles quelconques. *Master's Thesis, INSA, Lyon*.

[187] Visintin, A. (1994). *Differential Models of Hysteresis*. Springer Berlin Heidelberg.

[188] Vollebregt, E. (2014). A new solver for the elastic normal contact problem using conjugate gradients, deflation, and an FFT-based preconditioner. *Journal of Computational Physics*, 257:333–351.

[189] Wagner, L. F. and Griffin, J. H. (1990). Blade vibration with nonlinear tip constraint: Model development. *Journal of Turbomachinery*, 112(4):778.

[190] Wahlström, J. (2014). Towards a cellular automaton to simulate friction, wear, and particle emission of disc brakes. *Wear*, 313(1-2):75–82.

[191] Wang, F. and Keer, L. M. (2005). Numerical simulation for three dimensional elastic-plastic contact with hardening behavior. *Journal of Tribology*, 127(3):494.

[192] Wang, W., Liu, Y., Zhu, G., and Liu, K. (2014). Using FEM–DEM coupling method to study three-body friction behavior. *Wear*, 318(1-2):114–123.

[193] Wang, Z., Jin, X., Liu, S., Keer, L. M., Cao, J., and Wang, Q. (2013). A new fast method for solving contact plasticity and its application in analyzing elasto-plastic partial slip. *Mechanics of Materials*, 60:18–35.

[194] Wen, Y.-K. (1976). Method for random vibration of hysteretic systems. *Journal of the engineering mechanics division*, 102(2):249–263.

[195] Wentzel, H. (2006). *Modelling of frictional joints in dynamically loaded structures: a review*. KTH Solid mechanics, Royal Institute of technology.

[196] Whiteman, W. and Ferri, A. (1996). Displacement-dependent dry friction damping of a beam-like structure. *Journal of Sound and Vibration*, 198(3):313–329.

[197] Yang, B. and Menq, C. (1998). Characterization of 3d contact kinematics and prediction of resonant response of structures having 3d frictional constraint. *Journal of Sound and Vibration*, 217(5):909–925.

[198] Zmitrowicz, A. (1987). A thermodynamical model of contact, friction and wear: I governing equations. *Wear*, 114(2):135–168.

[199] Zmitrowicz, A. (2006). Wear patterns and laws of wear - a review. *Journal of theoretical and applied mechanics*, 44(2):219–253.

[200] Öqvist, M. (2001). Numerical simulations of mild wear using updated geometry with different step size approaches. *Wear*, 249(1-2):6–11.

Appendix A

Elliptical integral definitions

Elliptical integral of the first kind:

$$F(\varphi, m) = \int_0^{\varphi} \frac{1}{\sqrt{1 - m^2 \sin^2(\theta)}} d\theta \tag{A.1}$$

Elliptical integral of the second kind:

$$E(\varphi, m) = \int_0^{\varphi} \sqrt{1 - m^2 \sin^2(\theta)} d\theta \tag{A.2}$$

Complete elliptical integral of the first kind:

$$K(m) = \int_0^{\pi/2} \frac{1}{\sqrt{1 - m^2 \sin^2(\theta)}} d\theta \tag{A.3}$$

Complete elliptical integral of the second kind:

$$E(m) = \int_0^{\pi/2} \sqrt{1 - m^2 \sin^2(\theta)} d\theta \tag{A.4}$$

Appendix B

Permission to reproduce previously published work

17.11.2017

Dear Sir,

I am completing my PhD thesis at Imperial College London, which is entitled 'Nonlinear dynamics of jointed structures: a multiscale approach to predict fretting wear and its effects on the dynamic response'.

I seek your permission to reprint, in my thesis, the published version of the following papers:

Armand, J., Salles, L., & Schwingshackl, C. W. (2015). Numerical Simulation of Partial Slip Contact Using a Semi-Analytical Method. ASME. International Design Engineering Technical Conferences and Computers and Information in Engineering Conference, Volume 8: 27th Conference on Mechanical Vibration and Noise. doi:10.1115/DETC2015-46464.

Armand, J., Pesaresi, L., Salles, L., & Schwingshackl, C. W. (2016). A Multi-Scale Approach for Nonlinear Dynamic Response Predictions With Fretting Wear. ASME. Turbo Expo: Power for Land, Sea, and Air, *Volume 7A: Structures and Dynamics*. doi:10.1115/GT2016-56201.

Armand, J., Pesaresi, L., Salles, L., & Schwingshackl, C. W. (2016). A Multiscale Approach for Nonlinear Dynamic Response Predictions With Fretting Wear. ASME. Journal of Engineering for Gas Turbines and Power, 139(2), 022505. doi:10.1115/1.4034344.

I would like to include these papers in my thesis which will be added to Spiral, Imperial's institutional repository http://spiral.imperial.ac.uk/ and made available to the public under the following Creative Commons use licence: Attribution-NonCommercial-NoDerivs 3.0 Unported (CC BY-NC-ND 3.0).

If you are happy to grant all the requested permissions, please return a signed copy of this letter. If you wish to grant only some of them, please list these and then sign.

Yours sincerely,

Jason Armand

Jason Armand

Permission granted for the use requested above:

I confirm that the papers mentioned above under the Rolls-Royce copyright can be included in the PhD thesis which will be made available via the Internet, for non-commercial purposes under the terms of the user licence.

Name: Akin Keskin

Signature:

Organisation: Rolls-Royce plc.

Job title: Chief of VEDS